

Concentrated colloids in a centrifugal field

Citation for published version (APA):

Xu, X. (2020). *Concentrated colloids in a centrifugal field*. [Phd Thesis 1 (Research TU/e / Graduation TU/e), Chemical Engineering and Chemistry]. Technische Universiteit Eindhoven.

Document status and date:

Published: 04/11/2020

Document Version:

Publisher's PDF, also known as Version of Record (includes final page, issue and volume numbers)

Please check the document version of this publication:

- A submitted manuscript is the version of the article upon submission and before peer-review. There can be important differences between the submitted version and the official published version of record. People interested in the research are advised to contact the author for the final version of the publication, or visit the DOI to the publisher's website.
- The final author version and the galley proof are versions of the publication after peer review.
- The final published version features the final layout of the paper including the volume, issue and page numbers.

[Link to publication](#)

General rights

Copyright and moral rights for the publications made accessible in the public portal are retained by the authors and/or other copyright owners and it is a condition of accessing publications that users recognise and abide by the legal requirements associated with these rights.

- Users may download and print one copy of any publication from the public portal for the purpose of private study or research.
- You may not further distribute the material or use it for any profit-making activity or commercial gain
- You may freely distribute the URL identifying the publication in the public portal.

If the publication is distributed under the terms of Article 25fa of the Dutch Copyright Act, indicated by the "Taverne" license above, please follow below link for the End User Agreement:

www.tue.nl/taverne

Take down policy

If you believe that this document breaches copyright please contact us at:

openaccess@tue.nl

providing details and we will investigate your claim.

Concentrated colloids in a centrifugal field

PROEFSCHRIFT

ter verkrijging van de graad van doctor aan de Technische Universiteit Eindhoven, op
gezag van de rector magnificus prof.dr.ir.F.P.T. Baaijens, voor een commissie aangewezen
door het College voor Promoties, in het openbaar te verdedigen op woensdag 4 november
2020 om 16:00 uur

door

Xufeng Xu

geboren te Jiangsu, China

Dit proefschrift is goedgekeurd door de promotoren en de samenstelling van de promotiecommissie is als volgt:

voorzitter: prof.dr.ir. E.J.M. Hensen

1^e promotor: prof.dr. G. de With

2^e promotor: prof.dr. H. Cölfen (University of Konstanz)

leden: prof.dr. A.P. Philipse (Universiteit Utrecht)

prof.dr. T.N. Zemb (ICSM Site de Marcoule)

prof.dr.ir. R. Tuinier

prof.dr. J. Meuldijk

Het onderzoek dat in dit proefschrift wordt beschreven is uitgevoerd in overeenstemming met de TU/e Gedragscode Wetenschapsbeoefening.

To my dearest grandmother 张忠英

子曰：「學而不思則罔，思而不學則殆。」

《論語·為政》

Xufeng Xu

Concentrated colloids in a centrifugal field

Eindhoven University of Technology, 2020

The research described in this thesis has been carried out in three different places: 1) at the former Laboratory of Materials and Interface Chemistry (SMG) and current Laboratory of Physical Chemistry (SPC), within the Department of Chemical Engineering and Chemistry of the Eindhoven University of Technology, The Netherlands, 2) in AG Cölfen within the Department of Chemistry in University of Konstanz, Germany and 3) in Nanolytics GmbH with an associated guest stay in MPIKG, Potsdam, Germany.

This project has received funding from the European Union's Horizon 2020 research and innovation programme under grant agreement No. 676045.

A catalogue record is available from the Eindhoven University of Technology Library

ISBN: 978-90-386-5102-6

Printed by Gildeprint, Enschede, The Netherlands (www.gildeprint.nl)

Cover designed by Xufeng Xu

Cover photography by NASA (<https://earthobservatory.nasa.gov>)

As you may recognize, the cover photo is 黄河 (Yellow River) in my beloved home China. The sedimentation of concentrated sands is vividly demonstrated in the image of my mother river.

Copyright © 2020 by Xufeng Xu

Table of Contents

CHAPTER 1	1
<i>General introduction</i>	
1.1. Colloidal particles.....	2
1.2. Centrifugation.....	3
1.3. Aim and Outline	9
1.4. References	10
CHAPTER 2	15
<i>Hard-sphere-like colloids in a centrifugal field at high concentration</i>	
2.1. Introduction	16
2.2. Results and discussion.....	17
2.3. Conclusion.....	22
2.4. References	23
2.5. Appendix	26
CHAPTER 3	37
<i>Binary hard spheres with a large size ratio in a centrifugal field</i>	
3.1. Introduction	38
3.2. Results and discussion.....	40
3.3. Conclusion.....	43
3.4. Experimental section	45
3.5. References	45
3.6. Appendix	48
CHAPTER 4	51
<i>Self-association and gelation of like-charged colloids at very high concentration</i>	
4.1. Introduction	52
4.2. Results and discussion.....	53

4.3. Conclusion.....	59
4.4. References	59
4.5. Appendix	62
CHAPTER 5	77
<i>Layering of bidisperse charged nanoparticles in sedimentation</i>	
5.1. Introduction	78
5.2. Results and discussion.....	79
5.3. Conclusion.....	83
5.4. References	84
5.5. Appendix	87
CHAPTER 6	95
<i>Superstructure control for monodisperse nanoparticles with a low Peclet number in ultracentrifugation</i>	
6.1. Introduction	96
6.2. Results and discussion.....	97
6.3. Conclusion.....	102
6.4. References	102
6.5. Appendix	105
CHAPTER 7	111
<i>Conclusion and outlook</i>	
7.1. Conclusion.....	112
7.2. Outlook.....	113
7.3. References	113
List of important symbols and abbreviations	115
Acknowledgement	121
Curriculum vitae	121
Publication list	123

Summary

The sedimentation of colloidal particles is of great interest to both condensed matter physics and colloidal chemistry. Colloidal particles sediment until a sedimentation-diffusion equilibrium state is reached. From the equilibrium concentration profile, important thermodynamic information of these particles can be retrieved. The classic case is provided by Jean Baptiste Perrin who determined the Boltzmann constant by measuring the sedimentation of a suspension containing microscopic gamboge particles of a uniform size under natural gravity. Systematic studies on the sedimentation of colloids were followed from 1980s, beginning with the easiest case, namely nearly hard spheres, where only volume exclusion repulsion plays a role. Confocal laser scanning microscopy was for the first time applied to in-situ study the sedimentation process thoroughly. After that, the more practical but also more complicated case of charged colloids was studied theoretically by the inclusion of the Donnan equilibrium, followed by analytical ultracentrifugation (AUC) experiments on charged colloidal particles at low concentration. Following these classic researches, the sedimentation of concentrated colloidal particles in a centrifugal field with a much broader practical importance is described in my Ph.D. work

Specifically speaking, the sedimentation of fluorescent labeled silica particles at a very high concentration (up to 60 vol%) in a suspension of a refractive index matching solvent was studied in a centrifugal field, by using multi-wavelength analytical ultracentrifugation (MWL-AUC) along with detailed theoretical research. The two main directions in this Ph.D. work are: (I) the sedimentation of hard-sphere colloidal particles and (II) the sedimentation of charged colloidal particles.

(I) In the hard spheres part, it is shown that: 1) the concentration gradients of both monodisperse and binary hard-sphere colloidal particles can be measured and simulated at very high particle concentration up to 30 vol%, permitting tailor-made concentration gradients of colloidal particles in a centrifugal field. Therefore, a continuous and extended binary colloidal particle packing superstructure library can be obtained due to particle concentration ratio variation along the centrifugal field. This study helps to explore a large variety of binary colloidal particle packing superstructures, including different crystalline and amorphous structures. These structures can be formed simultaneously using a preparative ultracentrifuge, in one single experiment. 2) the buoyancy of the smaller colloidal particles during the sedimentation of a binary hard-sphere colloidal particle mixture with a considerable size ratio can be quantitatively well explained by the theory of effective buoyancy. In this theory, effective solvent density, which is calculated based on the particle concentration in suspension, will be employed instead of the normally used constant solvent density. This study proves the validity of effective buoyancy in colloidal particle mixtures and provides a good experimental model to study the sedimentation of polydisperse colloids.

(II) In the charged spheres part, it is shown that: 1) self-association and gel formation of charged colloids at extremely high concentration occurs, which is very different from the well-accepted good stability of like-charge colloids by electrostatic repulsion in a diluted suspension. In the study, we quantitatively analyze molecular, microscopic and macroscopic experimental results on like-charged colloids in a concentration gradient up to 60 vol% by

conducting sedimentation-diffusion equilibrium experiments in an AUC. The concentration gradient is shown to reveal important information, including particle size, particle surface charge and interparticle interaction. We even, surprisingly, observe a steep pH gradient resulting from the Donnan effect and the self-association of like-charge colloids at high concentration, leading to gel formation. These results will help us understand the effects of crowding on matter-matter interaction, which will have very important biological implications. 2) the layering of bidisperse charged colloids in a centrifugal field can be experimentally measured by MWL-AUC. Different factors, including particle size, charge and centrifugal field strength, are investigated experimentally for their effects on the layering. These experiments are supported by theoretical calculations, using an accurate equation of state for multicomponent mixtures (of particles of unequal size). Surprisingly, smaller colloidal particles can even sink below larger ones when the particle surface charge is carefully tuned. This study provides deeper insights in the control of layering in polydisperse particle mixtures during sedimentation, which can give some vital hints to use the thermodynamic driving force for colloidal particle purification.

(III) In the last part, a tiny piece of work is added to discuss the superstructure control of monodisperse colloidal particles with a low Peclet number under a centrifugal field. The intrinsic high diffusion rate of colloidal nanoparticles (with a low Peclet number) results in an extremely fast crystallization process and instant formation of colloidal crystals, even at a centrifugal field of an extremely high angular velocity. In this study, by introducing a very small amount (as low as 3%) of colloidal oligomers in the sedimentation process, we can obtain both crystalline and glassy superstructures by changing the centrifugal field strength. Therefore, a novel handle is provided to fabricate superstructures of tunable packing order for colloids with a low Peclet number, which may have a wide application in areas, such as quantum electronics, battery and photonic materials.

Overall, these results provide a deeper insight into the behavior of colloids in a crowded dispersion and this will help us to understand crowding effects on matter behavior, which is relevant for many fields in science and technology. In addition, the study of fluorescent labeled silica nanoparticles in a refractive index matching solvent by using one of the most powerful available quantitative techniques, namely analytical ultracentrifugation can serve as an excellent model system to study colloids at high concentration.

The research on concentrated colloids in a centrifugal field is still not well understood. The field will develop significantly if the two main issues are tackled: 1) software development to make tailor-made concentration gradients more convenient to design, with the combinational use of analytical and preparative (ultra)centrifugation; 2) methodology development to allow the measurement of concentration gradients in centrifugation without the pre-requirement of a refractive index matching solvent and fluorescent labelling, especially at high concentration. Solving these problems will certainly improve the range of applications to all kinds of colloidal particles and even to polymers. Therefore, it is expected to see more research output in this interdisciplinary field between colloidal science and the centrifugation techniques in future, especially for the applications in photonic materials, porous materials and functional gradient materials.

CHAPTER 1

General Introduction



This chapter is based on:

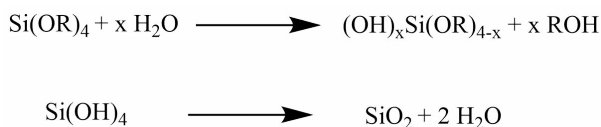
Xufeng Xu, Helmut Cölfen*. Ordering of nanoparticles in a centrifugal field.
Nanomaterials 2020, to be submitted (invited review).

1. General introduction

1.1. Colloidal particles

According to the IUPAC¹, colloids are defined as a state of subdivision, implying that the molecules or polymolecular particles dispersed in a medium have at least in one direction a dimension roughly between 1 nm and 1 μm , or that in a system discontinuities are found at distances of that order. Colloids² are vastly studied in the last decades, especially in physics and material science. In 1905, in his doctoral thesis Albert Einstein³ advanced a theory that any small object, especially colloidal particles, moves in constant randomness, known as the Brownian motion. After that, Jean Baptiste Perrin used optical microscopy to observe the motion of colloidal particles in the dispersion of water during the sedimentation under the gravity⁴ to demonstrate the barometric distribution and verify Albert Einstein's prediction. These studies prove that colloids behave in a similar way as atoms and molecules of a much smaller dimension. Therefore colloids can be treated as 'big atoms'⁵ for the study on the fundamental problems, ranging from phase transitions⁶⁻⁷ to crystal nucleation⁸⁻⁹ and equations of state of a system¹⁰. Moreover, colloidal particles are promising building blocks for the fabrication of micro-, meso- and macro-scale materials with controlled properties and functions¹¹⁻¹². These colloidal particle based materials are widely used for different aims, including carbon dioxide capture¹³, catalyst support¹⁴, fuel cell construction¹⁵ and so on.

Among a large variety of colloidal particles, silica particles¹⁶ are one of the mostly studied type mainly due to the availability of a 1) simple and well-established synthesis approach and 2) particles of a wide accessible size range and a low polydispersity. The synthesis of monodisperse silica particles was developed¹⁷ by Stöber in 1968 where a versatile sol-gel process was introduced. The synthesized particle size typically ranges from 50 to 2000 nm¹⁸. Recently an amino acid assisted approach¹⁹⁻²⁰ was reported for the synthesis of monodisperse silica particles below 50 nm. These two methods share the same synthesis mechanism, which consists of hydrolysis and condensation reaction steps, as shown in **Scheme 1.1**.



Scheme 1.1: The hydrolysis and condensation step in the silica particle synthesis.

The realization of fluorescent labeling²¹⁻²³ is regarded as another important milestone in the field of silica particles. By labeling with fluorescent dyes, the silica particles can be *in-situ* visualized and studied by confocal laser scanning microscopy (CLSM) and fluorescence microscopy. Thus, the behavior of colloids, such as crystallization and phase transitions can be *in-situ* studied in real time²⁴⁻²⁵. Moreover, fluorescent labeled silica particles can be used as an *in-vivo* probe in biological applications²⁶⁻²⁷. Another type of widely-studied particles is polystyrene particles²⁸ due to their simple synthesis procedures, and the low polydispersity and the superior stability that can be obtained. In this thesis, fluorescent labeled silica

particles are mainly used while polystyrene particles are used in the work as described in Chapter 6.

Colloids at low concentration have been extensively studied in the last decades. One of the most important achievements is the establishment of the DLVO (Derjaguin-Landau-Verwey-Overbeek) theory²⁹⁻³⁰ which is vastly employed to determine interparticle interactions. The theory works for a diluted dispersion where only pairs of colloidal particles are considered. However, there is limited research on colloids at high concentration because the challenging analytics of such systems as well as the complex interparticle interactions in concentrated conditions. Specifically speaking, the intrinsic hurdle at high concentration is that the turbidity of dispersions increases dramatically with the concentration hindering *in-situ* observation and analysis. Another important question is whether the interparticle interaction changes due to the participation of short ranged forces when the colloids move so close that even their electrical double layers overlap. In this thesis, concentrated silica nanoparticles in a refractive index matching solvent will be vastly employed as a model system to study the colloidal behavior at high concentration, which sheds light on the behavior of colloids in a crowded environment and helps to understand and predict the physicochemical behavior of colloidal dispersions in various applications of great practical and academic relevance.

1.2. Centrifugation

1.2.1. Preparative (ultra)centrifugation

Preparative (ultra)centrifugation (PUC) is a most widely used technique in a variety of disciplines, especially like chemistry and biology. It is employed to apply an enhanced gravity effect up to 800,000 *g* (correspondingly roughly to 100,000 rpm), suitable for a wide size window ranging from micrometer-sized species down to nanoparticles with an intrinsically low sedimentation rate³¹⁻³². Its main application can be found in the isolation/purification of a mixture of different species or of a polydisperse sample³³. It has also been used recently for the fabrication of macroscopic materials³⁴. The main mechanism behind the isolation is that different species have different sedimentation velocities due to their intrinsic properties such as size, density and shape. Therefore, the different species in a mixture tend to move to different positions after centrifugation for a specific time, which can be then collected separately. The most commonly used centrifugation assisted separation methods include 1) differential centrifugation; 2) isopycnic separation and 3) density gradient centrifugation. Differential centrifugation is the simplest method and it requires repeated centrifugation procedures by a series of progressively higher speeds, as shown in **Figure 1.1**. Isopycnic separation is also a traditional method where different species sediment by the centrifugal force to the position of the solvent having the same density, as shown in **Figure 1.2**. Density gradient centrifugation combines the advantages of these two methods and has proven to be powerful in different research cases, as shown **Figure 1.3**. For example, promising research results were illustrated in the recent years: the oligomer mixtures of 2 to more than 15 particles of polystyrene microspheres were separated using centrifugation of a linear gradient of Ficoll 400 in a 1% w/w Pluronic F108/water solution³⁵. Another example is the separation of gold nanoparticle mixtures of different shapes³⁶ and sizes³⁷ by

CHAPTER 1

centrifugation in a gradient of aqueous CsCl solutions and cyclohexane + tetrachloromethane separately.

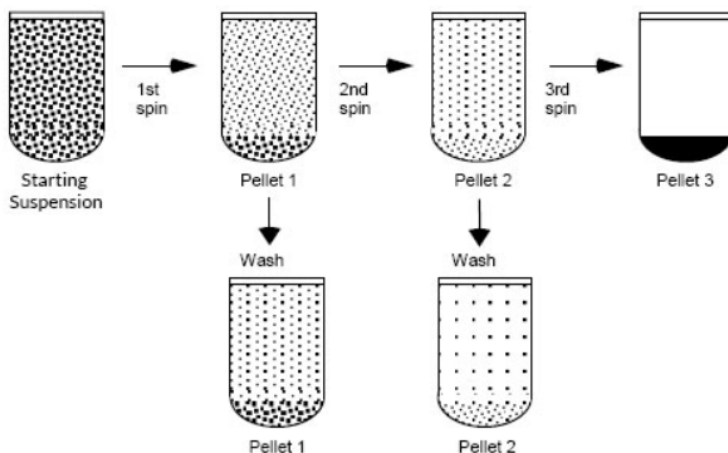


Figure 1.1: Schematic of the procedures for a typical differential centrifugation experiment.

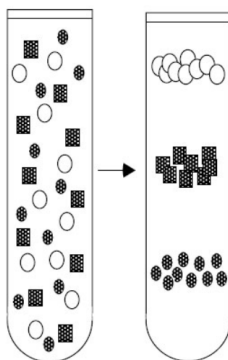


Figure 1.2: Schematic of the mechanism in a typical isopycnic separation experiment.

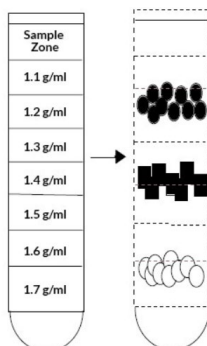


Figure 1.3: Schematic of the mechanism in a typical density gradient centrifugation experiment.

Moreover, centrifugation can be used to fabricate macroscopic materials. For instance, a crack-free and transferable film can be prepared by the sedimentation of colloidal particles in a centrifugal field³⁸. Three-dimensional materials of a crystalline^{34, 39} and amorphous⁴⁰ structure can also be prepared for photonic applications⁴¹⁻⁴². It is noteworthy that different types of rotors are designed for these different applications. As shown in **Figure 1.4**, the rotors can be divided into three categories: 1) Swinging bucket; 2) Fixed angle and 3) Vertical rotors. Accordingly, their pros and cons are listed in **Table 1.1**. In this thesis, the swinging bucket rotor (**SW 55 Ti** from Beckman coulter) is used for all the preparative centrifugation experiments.

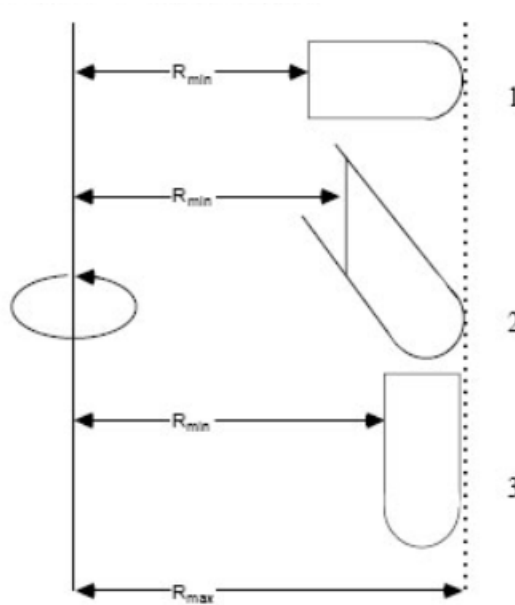


Figure 1.4: Three mostly used rotor types in a preparative centrifugation experiment: 1. swinging-bucket rotor; 2. fixed-angle rotor and 3. vertical rotor.

Type of rotor	Pelleting	Isopycnic	Density gradient
Fixed angle	Excellent	Limited	Good
Swinging-Bucket	Inefficient	Good	Good
Vertical	Not suitable	Good	Excellent

Table 1.1: The three mostly used types of rotors and their applications.

1.2.2. Analytical (ultra)centrifugation

Analytical (ultra)centrifugation (AUC)⁴³ is an important technique to precisely *in-situ* characterize colloidal particles in the dispersion⁴⁴ in real-time. The first ever AUC experiment can be traced back to the work⁴⁵⁻⁴⁶ done by Theodor Svedberg and his co-workers in the 1920s. They demonstrated the ability of AUC for the determination of the size and size distribution of nanoparticles, such as gold nanoparticles with the diameter of only 2 nm in dispersion, even before the invention of advanced electron microscopy⁴⁷. Later on, the AUC technique became widely used in the field of biochemistry and molecular biology, especially for the analysis of biological macromolecules such as proteins, nucleic acids and so on⁴⁸⁻⁴⁹. Nevertheless, this technique remains powerful in colloidal science⁵⁰ with the vast development in nanoscience and nanotechnology⁵¹⁻⁵² in the recent decades. In a typical AUC experiment, dissolved or dispersed samples inside an AUC measuring cell are exposed to a centrifugal field induced by the spinning of a centrifuge rotor. The reaction of the sample to this centrifugal field is *in-situ* detected by optical detection systems⁵³, as demonstrated in **Figure 1.5**. The two most fundamental theories for the analysis of the experimental data are due to Svedberg and Lamm. In the simplified Svedberg theory, three forces are assumed to come into balance immediately in a centrifugal field, namely the sedimentation (F_s), the buoyancy (F_b) and the frictional (F_f) force, and thus induce the sample species to move in a constant sedimentation velocity, as shown in **Equation 1.1**. With the introduction of these three forces and several rearrangements, the famous Svedberg Equation and an expression for the particle size can be deduced, as shown in **Equation 1.2**. and **Equation 1.3**⁵³.

$$F_s + F_b + F_f = 0 \quad (1.1)$$

$$M = \frac{sRT}{D(1 - \bar{v}\rho_s)} \quad (1.2)$$

$$d_p = \sqrt{\frac{18\eta_s s}{(\rho_p - \rho_s)}} \quad (1.3)$$

where M is the molecular mass of the species, s is the sedimentation coefficient, RT is the product of the molar gas constant R and temperature T , D is the diffusion coefficient, ρ_p and ρ_s are the density of the species and solvent, respectively, \bar{v} is the partial specific volume, d_p is the Stokes-equivalent diameter and η_s is the solvent viscosity.

In comparison, the general Lamm equation is deduced by a more accurate thermodynamic approach⁵³. It describes the sample concentration (c) change with time (t) and radius (r) during an AUC experiment, as shown in **Equation 1.4** and it basically holds for all kinds of AUC experiments.

$$\frac{\partial c}{\partial t} = D \left(\frac{\partial^2 c}{\partial r^2} + \frac{1}{r} \frac{\partial c}{\partial r} \right) - \omega^2 s \left(r \frac{\partial c}{\partial r} + 2c \right) \quad (1.4)$$

where D and s are the diffusion and sedimentation coefficient of the species, respectively.

Typically, four types of optical detection systems are implemented in an AUC instrument: Schlieren optics, Interference optics, UV-vis absorbance optics and Turbidity optics⁵⁴. Among these, the currently most-widely-used optics are interference and UV-vis absorbance optics and their typical optical patterns are shown in **Figure 1.6**. In the recent years, another advanced detector development has been launched: a multi-wavelength (MWL) optics⁵⁵⁻⁵⁷, which allows for the simultaneous measurement of multiple species by producing a three-dimensional information set (absorbance \times wavelength \times radial position), as shown in **Figure 1.7**.

The two most basic AUC experiments are sedimentation velocity (AUC-SV) and sedimentation equilibrium (AUC-SE) experiments, which are both used in this thesis. A typical AUC-SV experiment is carried out in a strong centrifugal field which allows for complete sedimentation of the to be measured species. By applying **Equation 1.2** and **1.3**, the molecular mass and particle diameter distribution can be obtained for the samples. In comparison, a typical AUC-SE experiment is carried out in a moderate or low centrifugal field. By doing so, the slowly developing sedimentation process can be gradually balanced by the back-diffusion process from the sample until an equilibrium state is achieved. This means that $\partial c / \partial t = 0$ in **Equation 1.4** and a concentration gradient $c(r)$ along the radius r is established accordingly in this equilibrium state. It is also worthwhile to mention that the final equilibrium concentration gradient is determined by the thermodynamics of the measuring system, including the absolute molar mass and the second virial coefficient/interspecies interaction of the sample⁵⁸.

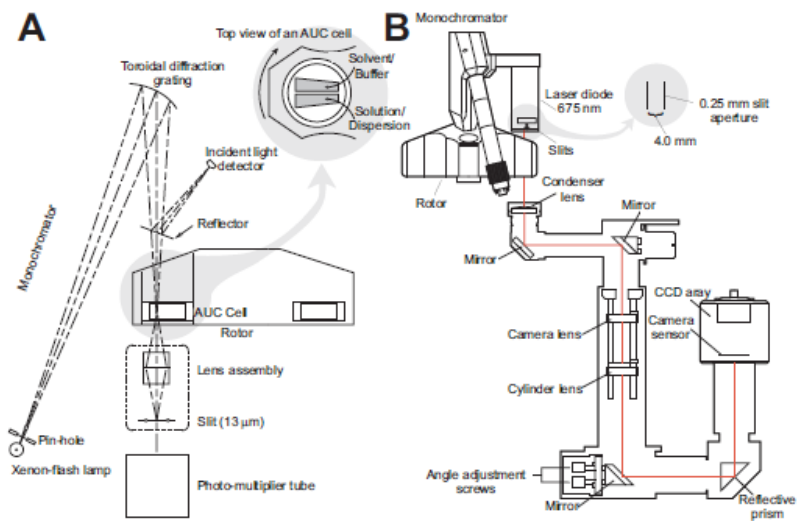


Figure 1.5: A schematic image of a Beckman Coulter™ Optima™ XL-A/XL-I AUC instrument equipped with an A. absorbance and B. interference optical system (reproduced from reference 53).

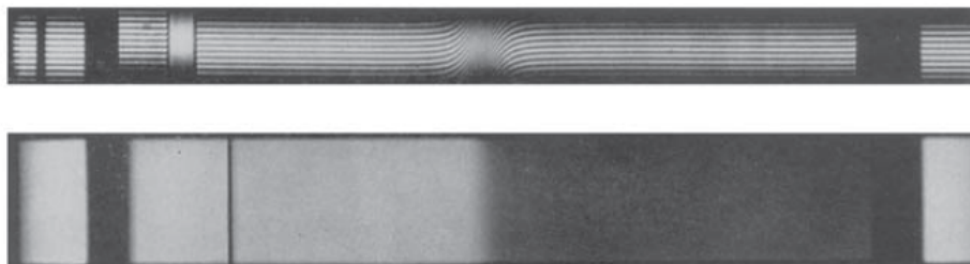


Figure 1.6: Typical optical patterns from the interference (figure above) and UV-vis absorbance (figure below) optics (reproduced from reference⁵³).

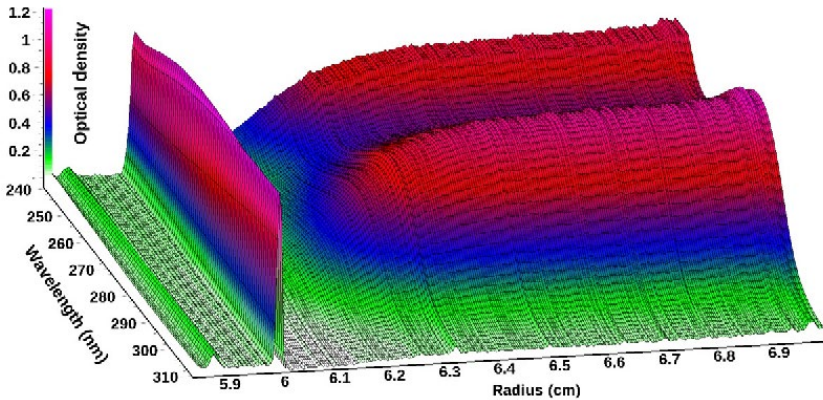


Figure 1.7: A typical multi-wavelength analytical ultracentrifugation result dataset (reproduced from reference³⁹).

1.3. Aim and Outline

Concentrated colloidal particles in a centrifugal field are of great interest in the understanding of the physicochemical behavior of any concentrated dispersion. This topic is not only relevant for industry, as processes using such dispersions are abundant, but also in academia, since interparticle interaction at such high concentration is largely unexplored. Moreover, colloidal particles interact strongly and order into a superstructure when the concentration becomes higher, especially above the phase transition point⁶⁰. After a proper fabrication, functional materials can be further prepared which find many applications in a large variety of fields. For example, photonic materials^{41, 61} including photonic crystals and glasses, can be fabricated to control and manipulate light. Porous materials⁶² can be also obtained after the infiltration and removal of templating nanoparticles, which is very promising in catalysis, chemical sensing, molecular separation and so on. Last but not least, functional gradient materials⁶³ can be made for the optimization of material properties for specific requirements, such as mechanical⁶⁴, thermal⁶⁵ and chemical properties⁶⁶.

In *Chapter 2*, we start from the simplest case, the colloidal particles with hard-sphere-like interaction. In this case, particles are deemed not to ‘feel’ any interparticle interaction when they are separated while they feel excluded volume repulsion of infinite strength after they touch each other. In this chapter, we discuss how monodisperse and binary hard spheres at high concentration behave in a centrifugal field, especially in sedimentation-diffusion equilibrium. With this knowledge, we may predict and control the concentration gradients of binary hard spheres, which finally help us tailor make different superstructures in the preparative centrifugation.

In *Chapter 3*, we describe an intriguing phenomenon in the sedimentation of binary hard spheres mixtures in a centrifugal field when the particle size ratio is sufficiently large. We found that the smaller particles feel an unexpected strong buoyancy force which can even levitate them in the presence of sufficiently larger particles. This buoyancy effect can be quantitatively explained by the concept of ‘effective’ solvent density. The theory and

CHAPTER 1

experiments are found to be in very good agreement in our case, which thus provides a good model to study sedimenting polydisperse colloidal particles in natural and industrial cases.

In *Chapter 4*, we move forward to a more complicated but also more realistic case of charged colloids. With a strong Donnan potential due to the presence of counterions, the concentration gradients of charged colloidal particles are unexpectedly much more extended. We also found that at extremely high concentration, interparticle interaction appears attractive even though these particles are like-charged. This attraction can even induce the gel formation. In this chapter, we will uncover the mystery in a highly concentrated and extremely nonideal suspension of charged colloids in a centrifugal field.

In *Chapter 5*, we will continue with charged colloids in a bimodal mixture. We found that the interparticle interaction between charged particles of two different sizes makes the particles layered, which means the spontaneous emergence of segregation during the sedimentation of binary charged colloids. This is due to the minimum Gibbs free energy in this system. With the help of the theoretical calculations using the Boublik–Mansoori–Carnahan–Starling–Leland (BMCSL) approximation, we can simulate the layering and even predict the counterintuitive ‘reverse’ layering where larger nanoparticles may float above the smaller ones. This knowledge is applicable to the control of particle segregation in the dispersions of polydisperse particles, which is very common in practice.

In *Chapter 6*, we will narrate a delicate story of superstructure control for monodisperse colloidal particles with a low Peclet number in a centrifugal field. Due to intrinsically fast diffusion of nanoparticles, it is extremely hard to construct a colloidal glass, even in a very strong centrifugal field. However, in this chapter, we show for latex colloids that by introducing as low as 3% of oligomers in the sedimentation process, a colloidal glass may be formed in a strong centrifugal field while a colloidal crystal may be formed in a weaker centrifugal field. Therefore, the assembly ordering of colloidal particles with a low Peclet number becomes fully tunable in a centrifugal field.

Finally, in *Chapter 7*, we will conclude and summarize the lessons and current hurdles on concentrated colloids in a centrifugal field. With a deeper understanding of interparticle interactions and ordering of colloidal particles at high concentration, we may have handles to tailor make superstructures, which is promising in the future for the fabrication of functional materials with different applications.

1.4. References

1. McNaught, A. D.; McNaught, A. D., *Compendium of chemical terminology*. Blackwell Science Oxford: 1997; Vol. 1669.
2. Russel, W. B.; Saville, D. A.; Schowalter, W. R., *Colloidal dispersions*. Cambridge University Press: Cambridge, 1989.
3. Einstein, A., Über die von der molekularkinetischen theorie der wärme geforderte bewegung von in ruhenden flüssigkeiten suspendierten teilchen. *Annalen der physik* **1905**, 322 (8), 549-560.
4. Oster, G., Brownian ratchets: Darwin's motors. *Nature* **2002**, 417 (6884), 25.
5. Poon, W., Colloids as big atoms. *Science* **2004**, 304 (5672), 830-831.
6. Pusey, P. N.; van Megen, W., Observation of a glass transition in suspensions of spherical colloidal particles. *Physical Review Letters* **1987**, 59 (18), 2083-2086.

7. Pusey, P. N.; van Megen, W., Phase behaviour of concentrated suspensions of nearly hard colloidal spheres. *Nature* **1986**, *320* (6060), 340-342.
8. Auer, S.; Frenkel, D., Prediction of absolute crystal-nucleation rate in hard-sphere colloids. *Nature* **2001**, *409* (6823), 1020.
9. Auer, S.; Frenkel, D., Suppression of crystal nucleation in polydisperse colloids due to increase of the surface free energy. *Nature* **2001**, *413* (6857), 711.
10. Piazza, R., Settled and unsettled issues in particle settling. *Reports on Progress in Physics* **2014**, *77* (5), 056602.
11. Lu, Z.; Yin, Y., Colloidal nanoparticle clusters: Functional materials by design. *Chemical Society Reviews* **2012**, *41* (21), 6874-6887.
12. Ciesla, U.; Schüth, F., Ordered mesoporous materials. *Microporous and Mesoporous Materials* **1999**, *27* (2), 131-149.
13. Yang, H.; Xu, Z.; Fan, M.; Gupta, R.; Slimane, R. B.; Bland, A. E.; Wright, I., Progress in carbon dioxide separation and capture: A review. *Journal of Environmental Sciences* **2008**, *20* (1), 14-27.
14. Huh, S.; Chen, H.-T.; Wiench, J. W.; Pruski, M.; Lin, V. S. Y., Cooperative catalysis by general acid and base bifunctionalized mesoporous silica nanospheres. *Angewandte Chemie International Edition* **2005**, *44* (12), 1826-1830.
15. Lu, S.; Wang, D.; Jiang, S. P.; Xiang, Y.; Lu, J.; Zeng, J., Hpw/mcm-41 phosphotungstic acid/mesoporous silica composites as novel proton-exchange membranes for elevated-temperature fuel cells. *Advanced Materials* **2010**, *22* (9), 971-976.
16. Bergna, H. E.; Roberts, W. O., *Colloidal silica: Fundamentals and applications*. CRC Press: 2005.
17. Stöber, W.; Fink, A.; Bohn, E., Controlled growth of monodisperse silica spheres in the micron size range. *Journal of Colloid and Interface Science* **1968**, *26* (1), 62-69.
18. Carcouet, C. Chemistry and morphology of silica nanoparticles. PhD thesis, Eindhoven university of Technology, 2014.
19. Watanabe, R.; Yokoi, T.; Kobayashi, E.; Otsuka, Y.; Shimojima, A.; Okubo, T.; Tatsumi, T., Extension of size of monodisperse silica nanospheres and their well-ordered assembly. *Journal of Colloid and Interface Science* **2011**, *360* (1), 1-7.
20. Yokoi, T.; Sakamoto, Y.; Terasaki, O.; Kubota, Y.; Okubo, T.; Tatsumi, T., Periodic arrangement of silica nanospheres assisted by amino acids. *Journal of the American Chemical Society* **2006**, *128* (42), 13664-13665.
21. Verhaegh, N. A. M.; Vanblaaderen, A., Dispersions of rhodamine-labeled silica spheres - synthesis, characterization, and fluorescence confocal scanning laser microscopy. *Langmuir* **1994**, *10* (5), 1427-1438.
22. Van Blaaderen, A.; Vrij, A., Synthesis and characterization of colloidal dispersions of fluorescent, monodisperse silica spheres. *Langmuir* **1992**, *8* (12), 2921-2931.
23. Ow, H.; Larson, D. R.; Srivastava, M.; Baird, B. A.; Webb, W. W.; Wiesner, U., Bright and stable core-shell fluorescent silica nanoparticles. *Nano Letters* **2005**, *5* (1), 113-117.
24. Van Blaaderen, A.; Ruel, R.; Wiltzius, P., Template-directed colloidal crystallization. *Nature* **1997**, *385*, 321.
25. Van Blaaderen, A.; Wiltzius, P., Real-space structure of colloidal hard-sphere glasses. *Science* **1995**, *270* (5239), 1177-1179.

CHAPTER 1

26. Rocco, M. A.; Kim, J.-Y.; Burns, A.; Kostecki, J.; Doody, A.; Wiesner, U.; DeLisa, M. P., Site-specific labeling of surface proteins on living cells using genetically encoded peptides that bind fluorescent nanoparticle probes. *Bioconjugate Chemistry* **2009**, *20* (8), 1482-1489.
27. Bae, S. W.; Tan, W.; Hong, J.-I., Fluorescent dye-doped silica nanoparticles: New tools for bioapplications. *Chemical Communications* **2012**, *48* (17), 2270-2282.
28. Reese, C. E.; Guerrero, C. D.; Weissman, J. M.; Lee, K.; Asher, S. A., Synthesis of highly charged, monodisperse polystyrene colloidal particles for the fabrication of photonic crystals. *Journal of Colloid and Interface Science* **2000**, *232* (1), 76-80.
29. Derjaguin, B. V.; Churaev, N. V.; Muller, V. M., The derjaguin—landau—verwey—overbeek (dlvo) theory of stability of lyophobic colloids. In *Surface forces*, Springer US: Boston, MA, 1987; pp 293-310.
30. Verwey, E. J. W.; Overbeek, J. T. G.; van Nes, K., *Theory of the stability of lyophobic colloids: The interaction of sol particles having an electric double layer*. Elsevier Publishing Company: 1948.
31. Graham, J. M., *Biological centrifugation*. Bios: 2001.
32. Rickwood, D., *Preparative centrifugation: A practical approach*. IRL Press Oxford, UK: 1992.
33. Ford, T.; Graham, J. M., *An introduction to centrifugation*. Bios: 1991.
34. Holland, B. T.; Blanford, C. F.; Stein, A., Synthesis of macroporous minerals with highly ordered three-dimensional arrays of spheroidal voids. *Science* **1998**, *281* (5376), 538-540.
35. Manoharan, V. N.; Elsesser, M. T.; Pine, D. J., Dense packing and symmetry in small clusters of microspheres. *Science* **2003**, *301* (5632), 483-487.
36. Chen, G.; Wang, Y.; Tan, L. H.; Yang, M.; Tan, L. S.; Chen, Y.; Chen, H., High-purity separation of gold nanoparticle dimers and trimers. *Journal of the American Chemical Society* **2009**, *131* (12), 4218-4219.
37. Qiu, P.; Mao, C., Viscosity gradient as a novel mechanism for the centrifugation-based separation of nanoparticles. *Advanced Materials* **2011**, *23* (42), 4880-4885.
38. Fan, W.; Chen, M.; Yang, S.; Wu, L., Centrifugation-assisted assembly of colloidal silica into crack-free and transferrable films with tunable crystalline structures. *Scientific Reports* **2015**, *5*, 12100.
39. Holland, B. T.; Blanford, C. F.; Do, T.; Stein, A., Synthesis of highly ordered, three-dimensional, macroporous structures of amorphous or crystalline inorganic oxides, phosphates, and hybrid composites. *Chemistry of Materials* **1999**, *11* (3), 795-805.
40. Chen, M.; Fischli, D.; Schertel, L.; Aubry, G. J.; Häusele, B.; Polarz, S.; Maret, G.; Cölfen, H., Free-standing photonic glasses fabricated in a centrifugal field. *Small* **2017**, *13* (34), 1701392.
41. García, P. D.; Sapienza, R.; Blanco, Á.; López, C., Photonic glass: A novel random material for light. *Advanced Materials* **2007**, *19* (18), 2597-2602.
42. López, C., Materials aspects of photonic crystals. *Advanced Materials* **2003**, *15* (20), 1679-1704.
43. Zhao, H.; Brautigam, C. A.; Ghirlando, R.; Schuck, P., Overview of current methods in sedimentation velocity and sedimentation equilibrium analytical ultracentrifugation. *Current Protocols in Protein Science* **2013**, 20.12. 1-20.12. 49.
44. Planken, K. L.; Cölfen, H., Analytical ultracentrifugation of colloids. *Nanoscale* **2010**, *2* (10), 1849-1869.

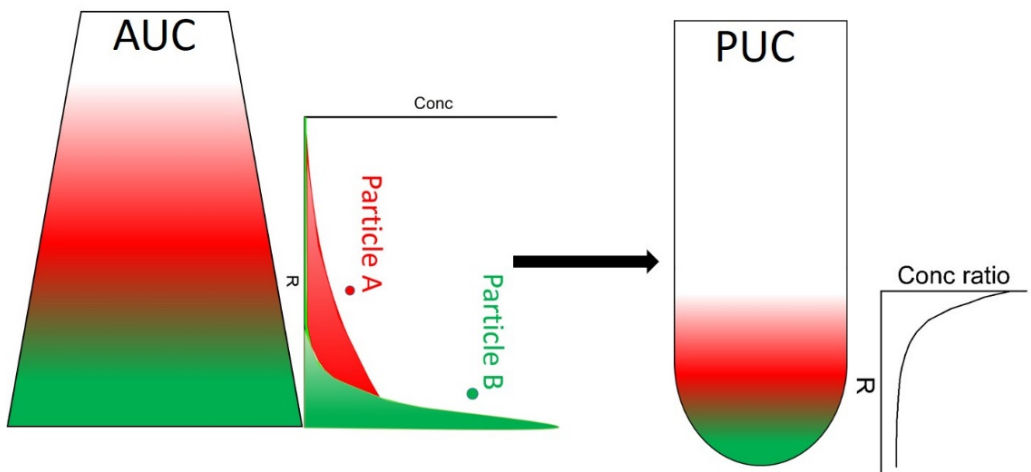
45. Svedberg, T.; Rinde, H., The determination of the distribution of size of particles in disperse systems I. *Journal of the American Chemical Society* **1923**, *45* (4), 943-954.
46. Svedberg, T.; Rinde, H., The ultra-centrifuge, a new instrument for the determination of size and distribution of size of particle in amicroscopic colloids. *Journal of the American Chemical Society* **1924**, *46* (12), 2677-2693.
47. Flegler, S. L.; Flegler, S. L., *Scanning & transmission electron microscopy*. Oxford University Press: 1997.
48. Behlke, J.; Ristau, O., Analysis of the thermodynamic non-ideality of proteins by sedimentation equilibrium experiments. *Biophysical Chemistry* **1999**, *76* (1), 13-23.
49. Schuck, P., Size-distribution analysis of macromolecules by sedimentation velocity ultracentrifugation and lamm equation modeling. *Biophysical Journal* **2000**, *78* (3), 1606-19.
50. Cölfen, H., Analytical ultracentrifugation of colloids. In *Analytical ultracentrifugation: Techniques and methods*, SCOTT, D. J., ed. and others, Ed. Cambridge: Royal Society of Chemistry: UK, 2005; Vol. 23, pp 501-583.
51. Whitesides, G. M., Nanoscience, nanotechnology, and chemistry. *Small* **2005**, *1* (2), 172-179.
52. Murty, B.; Shankar, P.; Raj, B.; Rath, B.; Murday, J., *Textbook of nanoscience and nanotechnology*. Springer Science & Business Media: 2013.
53. Maechtle, W.; Börger, L., *Analytical ultracentrifugation of polymers and nanoparticles*. Springer: Berlin ; New York, 2006; p xiii, 237 p.
54. Schuck, P.; Zhao, H.; Brautigam, C. A.; Ghirlando, R., *Basic principles of analytical ultracentrifugation*. CRC Press: 2016.
55. Pearson, J.; Walter, J.; Peukert, W.; Cölfen, H., Advanced multiwavelength detection in analytical ultracentrifugation. *Analytical Chemistry* **2018**, *90* (2), 1280-1291.
56. Karabudak, E.; Cölfen, H., The multiwavelength uv/vis detector: New possibilities with an added spectral dimension. In *Analytical ultracentrifugation: Instrumentation, software, and applications*, Uchiyama S., A. F., Stafford W., Laue T., Ed. Springer, Tokyo: 2016.
57. Walter, J.; Löhr, K.; Karabudak, E.; Reis, W.; Mikhael, J.; Peukert, W.; Wohlleben, W.; Cölfen, H., Multidimensional analysis of nanoparticles with highly disperse properties using multiwavelength analytical ultracentrifugation. *ACS Nano* **2014**, *8* (9), 8871-8886.
58. Perrin, J., *Atoms*. Van Norstrand Company: New York, 1913.
59. Gorbet, G. E.; Pearson, J. Z.; Demeler, A. K.; Cölfen, H.; Demeler, B., Chapter two - next-generation auc: Analysis of multiwavelength analytical ultracentrifugation data. In *Methods in enzymology*, Cole, J. L., Ed. Academic Press: 2015; Vol. 562, pp 27-47.
60. Davis, K. E.; Russel, W. B.; Glantschnig, W. J., Disorder-to-order transition in settling suspensions of colloidal silica: X-ray measurements. *Science* **1989**, *245* (4917), 507-510.
61. Joannopoulos, J. D.; Villeneuve, P. R.; Fan, S., Photonic crystals. *Solid State Communications* **1997**, *102* (2-3), 165-173.
62. Cecilia, J. A.; Moreno Tost, R.; Retuerto Millán, M., Mesoporous materials: From synthesis to applications. *International Journal of Molecular Science* **2019**, *20* (13), 3213.
63. Rabin, B.; Shiota, I., Functionally gradient materials. *MRS Bulletin* **1995**, *20* (1), 14-18.

CHAPTER 1

64. Luo, R.; Wu, J.; Dinh, N.-D.; Chen, C.-H., Gradient porous elastic hydrogels with shape-memory property and anisotropic responses for programmable locomotion. *Advanced Functional Materials* **2015**, *25* (47), 7272-7279.
65. Miyamoto, Y.; Kaysser, W.; Rabin, B.; Kawasaki, A.; Ford, R. G., *Functionally graded materials: Design, processing and applications*. Springer Science & Business Media: 2013; Vol. 5.
66. Cherradi, N.; Kawasaki, A.; Gasik, M., Worldwide trends in functional gradient materials research and development. *Composites Engineering* **1994**, *4* (8), 883-894.

CHAPTER 2

Hard-Sphere-Like Colloids in a Centrifugal Field at High Concentration



The results described in this chapter are based on:

X. Xu, T. Franke, K. Schilling, N.A.J.M. Sommerdijk, and H. Cölfen*. Binary Colloidal Nanoparticle Concentration Gradients in a Centrifugal Field at High Concentration. *Nano Letters* 2019 19 (2), 1136-1142.

2. Hard-sphere-like colloids in a centrifugal field at high concentration

Binary colloidal nanoparticles have been found to form different types of crystalline phases at varied radial positions in a centrifugal field by Chen et al. (*ACS Nano* **2015**, 9, 6944-50.). A variety of binary phase behaviors resulted from the two different nanoparticle concentration gradients but to date the concentration gradients can only be empirically controlled. For the first time, we can measure, fit and simulate monodisperse and binary hard sphere colloidal nanoparticle concentration gradients at high particle concentration up to 30 vol%, which enables tailor-made gradients in a centrifugal field. By this means, a continuous range of binary particle concentration ratios can be accessed in one single preparative ultracentrifugation experiment to obtain an extended phase diagram of binary superstructures in merely one centrifuge tube, rather than many parallel experiments with discrete compositions in conventional studies.

2.1. Introduction

The construction of binary colloidal crystals is currently a challenge since the crystallization process is controlled by a delicate balance of several nanoparticle properties, such as particle softness, concentration ratio, size ratio and charge ratio¹⁻³. Among these parameters, the concentration ratio is easiest to tune but it requires a large amount of experiments with discrete compositions to observe all the possible phases including different crystalline and amorphous structures. For instance, in recent years, the confinement was widely employed to induce the binary nanoparticle superlattice formation^{1, 4-5}. Although the superlattice structure was well-ordered over a large range, only one type of ordering was present in each experiment due to the fixed concentration ratio. Recently, a large variety of binary crystalline phases, including kinetic structures, have been simultaneously observed in a single experiment in a centrifugal field by Chen et al.². Different binary nanoparticle phases were formed at various radial positions due to different radial concentration gradients of two differently sized particles in a centrifugal field, while unusual kinetic crystalline phases might be formed due to kinetic spatial confinement and instability thresholds associated with the concentration gradients⁶ or the highly charged surface⁷. However, the radial concentration gradients were not yet experimentally accessible in an Analytical Ultracentrifugation (AUC) experiment because 1) the high refractive index difference between nanoparticles and water causes strong turbidity and 2) the two differently sized nanoparticles cannot be distinguished by optical detectors. Therefore, the desired correlation between the concentration gradients of two differently sized nanoparticles and the different binary colloidal phase behaviors could not be established. Besides, a very important open question is if these concentration gradients can be described by the established theory of ultracentrifugation⁸⁻⁹ and therefore be simulated in advance to reach the goal of tailor-made binary concentration gradients for the access to an extended and continuous phase diagram of the mixture of colloids¹⁰⁻¹¹. In this chapter, we report that the concentration gradients of binary fluorescent labeled silica nanoparticles in a refractive index matching solvent can be measured at high particle concentration up to 30 vol% by a multi-wavelength UV-vis detector in an analytical ultracentrifuge (MWL-AUC)¹².

Moreover, the experimentally measured concentration gradients can be fitted to the Lamm equation¹³ using for example the SEDFIT¹⁴ software with a non-interacting non-ideal sedimentation model, which provides the required parameters including the sedimentation coefficient s , the diffusion coefficient D as well as the non-ideality coefficients k_s and k_D for the subsequent simulation and prediction of binary nanoparticle concentration gradients. By using the simulated concentration gradients, the concentration ratio variation along the centrifugal field can be precisely determined and correlated with the binary nanoparticle phase behavior at each radial position as determined by the Scanning Electron Microscope (SEM). In this way a continuous and extended phase diagram can be obtained for a mixture of colloids from a single preparative ultracentrifugation (PUC) experiment instead of performing a series of experiments with many discrete compositions¹¹.

2.2. Results and discussion

In order to measure binary nanoparticle concentration gradients by MWL-AUC, fluorescent labeled polyethylene glycol (PEG) stabilized silica nanoparticles of two different sizes, namely 30 nm and 40 nm, were synthesized according to a modified protocol from combined previous works¹⁵⁻²⁰ (The detailed synthesis process is described in **SI 1**). Briefly, the protocol included three steps: 1. Two dyes, namely fluorescein isothiocyanate (FITC) and rhodamine isothiocyanate (RITC), were covalently bonded to cross linking 3-aminopropyltriethoxy-silane (APTES) to form two different fluorescent cores; 2. Hydrolyzed tetraethyl orthosilicate (TEOS) crosslinked and formed a shell surrounding the fluorescent cores. The smallest size of fluorescent labeled silica nanoparticle seeds was reported to reach 4.4 nm, only marginally larger than the free dye, and different amounts of TEOS were added to tune the final nanoparticle sizes²¹⁻²²; 3. Appropriate amounts of PEG-silane polymers were covalently linked to the surface of the above-synthesized silica nanoparticles (SNPs) as steric stabilizers, not only to suppress the irreversible agglomeration during centrifugation induced by up-concentration but also to neutralize most surface charges so that the nanoparticles can be treated as hard spheres²³. By this approach, 30 nm RITC-SNPs and 40 nm FITC-SNPs were synthesized. Moreover, a key prerequisite for a proper AUC measurement is that the turbidity of nanoparticle dispersions must be minimized. Otherwise most incident light will be scattered, and no concentration gradients can be detected by the optical system of the AUC. This issue can be solved by using a refractive-index (n) matching solvent and correcting the remaining slight turbidity at high concentration using the MWL spectra in the AUC data. In this chapter, an 80 vol% glycerol and 20 vol% water mixture was used to match the refractive index of the silica nanoparticles ($n \approx 1.45$) (**Figure S1**). It was also proven that the glycerol water mixture formed a negligible density gradient in the AUC at the applied angular velocity (The detailed calculation procedures are described in **SI 2**).

AUC has been in long-term use as a precise method²⁴⁻²⁵ for characterizing sedimentation-diffusion processes of colloidal nanoparticles *in situ*. The concentration profiles can be detected *in situ* by embedded interference optics or UV-vis absorbance optics²⁶⁻²⁷. The recent launch of multiwavelength (MWL) optical detectors^{12, 28-29} has been allowing for the simultaneous measurement of binary or even multiple nanoparticles, given that the particles are labeled with different chromophores. In a sedimentation-diffusion

CHAPTER 2

equilibrium (AUC-SE) experiment, the final equilibrium is formed due to the counterbalanced sedimentation and diffusion processes in a centrifugal field⁹. In order to fit the experimentally obtained equilibrium concentration gradients, the SEDFIT software package³⁰ was used. For fitting and simulating an experimental nanoparticle concentration gradient in this study, a non-interacting non-ideal sedimentation model embedded in the software was used because 1) The synthesized SNPs were sterically stabilized by PEG chains of a short length ($M_w = 1160$ Da, circa 1 nm) and the surface charge was mostly neutralized by the PEG-silane linkage (Zeta potential = -6 mV in water). The Van der Waals attraction was also minimized by refractive index matching. Therefore the nanoparticles can be treated as hard spheres²³; 2) The non-ideality effect must be taken into account at high concentration³¹⁻³² by including the non-ideality coefficients k_s and k_D . Both thermodynamic and hydrodynamic non-ideality²⁶ were taken into account by: $s = s_0/(1 + k_s \times c)$ and $D = D_0/(1 + k_D \times c)$ where s_0 and D_0 are the sedimentation and diffusion coefficients at infinite dilution, and s and D are the sedimentation and diffusion coefficients at concentration c . In the applied model, the experimental concentration profiles can be fitted, obtaining the sedimentation coefficient s , the diffusion coefficient D as well as the non-ideality coefficients k_s and k_D . The fitted parameters can be further used for subsequent simulations of binary concentration gradients with the goal to finally be able to simulate concentration gradients in PUC where particle concentrations are not monitored anymore.

As a first step, the separate concentration gradients of 30 nm RITC-SNPs and 40 nm FITC-SNPs were formed in AUC-SE experiments (the detailed experimental set-up is described in **SI 3**). By fitting the experimental data, s , D , k_s and k_D were obtained. More specifically, the values of s and D were first determined by fitting the sedimentation velocity (AUC-SV) experiments (**Figure S4**). Then k_s and k_D were determined by fitting the subsequent AUC-SE experiments (the detailed fitting process is described in **SI 4**). The final fitting results are shown in **Figure 2.1**. The fitting profiles agree with the experiments with randomly distributed residual signals. Quantitatively speaking, the root-mean-square deviation (RMSD) values of the concentration residuals reached only 0.037 vol% and 0.039 vol% and the maximum deviations were smaller than 0.05 vol% and 0.07 vol% for 30 nm and 40 nm SNPs separately. The s and D values used for the following simulations were also verified by calculating the densities (ρ) and molecular masses (M) of 30 nm and 40 nm SNPs³³. The calculation results agreed with the theoretical values within an acceptable relative deviation (the detailed calculation procedures and results are described in **SI 5**).

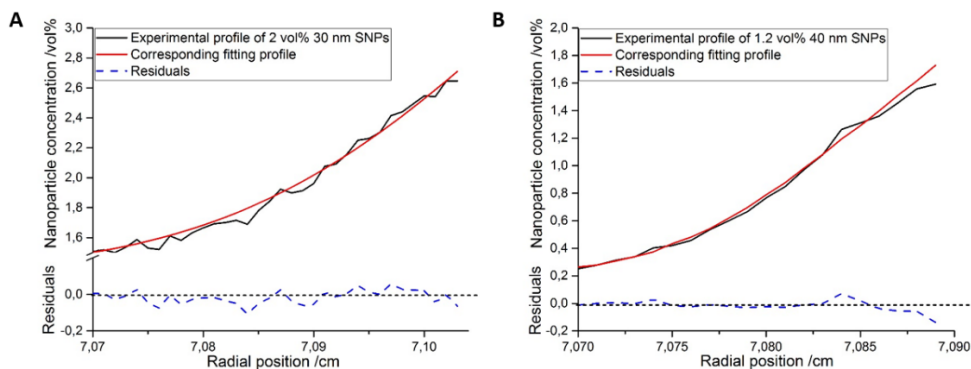


Figure 2.1: Experimental (black solid lines) and fitting (red solid lines) gradients for 30 nm RITC-SNPs of 2 vol% (A) and 40 nm FITC-SNPs of 1.2 vol% (B) in an AUC at 2800 rpm, 25 °C; The blue dashed lines are the residuals which result from fitting to the experimental data. For (A) and (B) the root-mean-square deviation (RMSD) = 0.037 vol% and 0.039 vol%, respectively.

In the following, these validated fitting parameters at moderate concentrations were used for simulations of potential concentration gradients beforehand. In order to access the reliability of the simulations, two experiments were conducted for 30 nm and 40 nm SNPs separately. Firstly, the simulation reliability was proved for an extremely high concentration (30 vol%) of 30 nm RITC-SNPs. In order to measure this extremely high concentration in the experiment, the optical pathlength had to be dramatically reduced to ca. 0.1 mm as reported by Page et al.³⁴. As shown in **Figure 2.2A**, the simulation profile agrees with the experimental result, even at this extremely high concentration. Secondly, the simulation reliability was tested for a larger column height of 40 nm FITC-SNPs. Similarly, in **Figure 2.2B**, the simulation for a larger volume is given showing that the simulation successfully predicted the experimental concentration gradient. Overall, these experiments on the two nanoparticles demonstrated that the simulations were able to predict the concentration gradients within an acceptable deviation (RMSD < 0.04) regardless of nanoparticle concentration and volume.

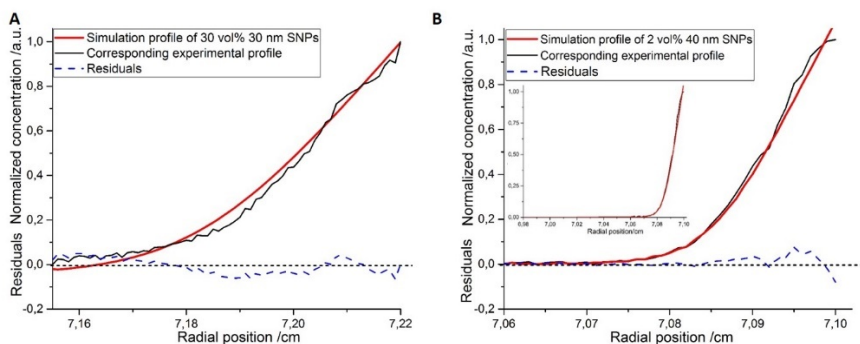


Figure 2.2: Normalized simulations (red solid lines) and corresponding experiments (black solid lines) for 30 nm RITC-SNPs of 30 vol% (A) and 40 nm FITC-SNPs of 2 vol% (B) at 2800 rpm, 25 °C (inset in (B) showed the whole sample volume). The blue dashed lines are the residuals which result from fitting to the experimental data. The experimental gradients were normalized to the range of the simulations. For (A) and (B) the RMSD = 0.034 and 0.023, respectively.

After the two monodisperse systems, we considered the binary nanoparticle mixture of 30 nm RITC-SNPs and 40 nm FITC-SNPs. The concentration profiles of these two nanoparticles were extracted separately from one absorbance spectrum (**Figure S5**) at every radial position in MWL-AUC (the detailed calculation procedures are described in **SI 6**). Because these two nanoparticles were treated as hard spheres, the non-interacting model was used and thus the two concentration profiles were simulated separately using the fitted parameters for the separate nanoparticles. The 10 vol% mixture of 30 nm and 40 nm SNPs in a volume ratio of 1:2 (**Figure 2.3A**) were simulated beforehand (another binary case with a volume ratio of 1:1 is shown in **Figure S6** in **SI 7**). Then, the experiment of the same mixture was conducted. The resulting concentration gradients were normalized to compare with the simulations. We found the simulations predicted successfully the experimental results within an acceptable deviation (RMSD < 0.03). Therefore, we can simulate and predict binary nanoparticle concentration gradients. Notably, shown in **Figure 2.3B**, the slight turbidity at very high concentration in the experiments can be corrected (the detailed turbidity correction procedure is described in **SI 8**). Correspondingly, the RMSD values changed from 0.023 and 0.019 to 0.014 and 0.023 for the 30 nm and 40 nm SNPs, respectively, after the turbidity correction. The RMSD decreased for 30 nm SNPs while the RMSD increased for 40 nm SNPs so the remaining slight turbidity insignificantly influenced the final concentration gradients. More importantly, using the confocal laser scanning microscope (CLSM), the simulations were proven valid even in preparative ultracentrifugation (PUC) (the detailed experiment and results are described in **SI 9**).

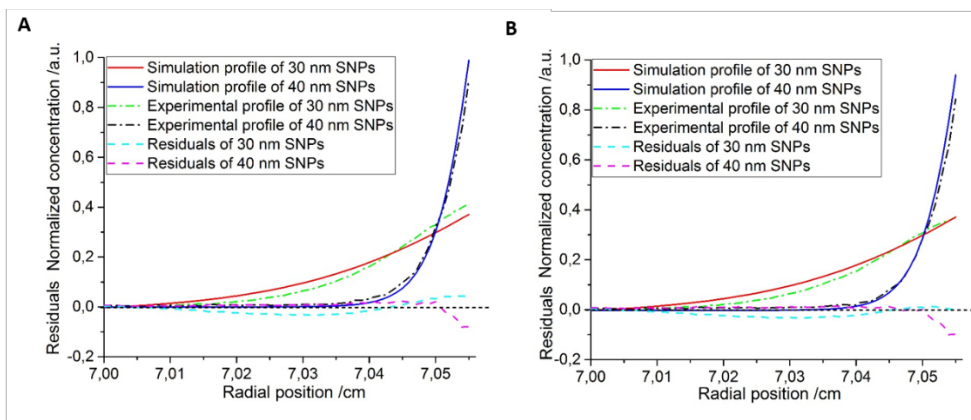


Figure 2.3: Normalized simulation (solid lines) and experimental (dash dotted lines) gradients for the 10 vol% binary mixture of 30 nm RITC-SNPs and 40 nm FITC-SNPs in a volume ratio of 1:2 at 2800 rpm, 25 °C (A). The slight turbidity influence at very high concentrations was corrected and a better agreement was achieved (B). The dashed lines are the residuals which result from fitting to the experimental data. The experimental concentration gradients were normalized to the range of the simulations. The RMSD values are 0.023 and 0.019, respectively, for the agreement of the simulations with the experiments in (A) and 0.014 and 0.023, respectively, for the agreement of the simulations with the experiments in (B).

Finally, the phase behaviors for the binary mixture of 30 nm and 40 nm SNPs along the centrifugal field were studied by SEM (the detailed PUC experiment and the sample preparation for SEM are described in **SI10**). Before the PUC experiment, the concentration gradients of the binary nanoparticle mixture were predetermined by the simulation. In **Figure 2.4A**, the concentration ratios (\approx volume ratio, since the both silica nanoparticles have approximately the same density) of the binary nanoparticle mixtures can be precisely determined to correlate with the final phase structures at each radial position (**Figure 2.4B**). In the upper part of the sediment cross-section (**Figure S9**) where the 30 nm SNPs dominated, a mixture of the 30 nm SNPs crystalline phase and a small amount of randomly distributed 40 nm SNPs were observed (**Figure 2.5A**). This phase was continuously observed from the meniscus until the radial position: 10.824 cm, 0.005 cm from the meniscus (**Figure 2.5B and C**). At the positions below this transition position, where the number of 40 nm SNPs became comparable to that of 30 nm SNPs, the crystalline phase disappeared and only a glassy mixture of 30 nm + 40 nm SNPs was observed (**Figure 2.5D**). From this continuous observation along the centrifugal field, the phase diagram was obtained (**Figure 2.4B**). The transition concentration ratio was $c_{30 \text{ nm}}/c_{40 \text{ nm}} = 4.8$ according to its corresponding radial position. When the concentration ratio was larger than 4.8, 30 nm SNPs formed crystals decorated with discrete 40 nm SNPs while when the concentration ratio decreased from 4.8 to 1.6 at the very bottom, the two nanoparticles were mixed to form an amorphous phase.

Interestingly, a perfect agreement was found with the previous work by Hunt et al.¹⁰. They studied the size ratio 0.72 ± 0.01 (correspondingly a mixture of 40 nm and 29 nm

CHAPTER 2

particles) by light scattering and found a crystalline phase of the smaller particle in the region $c_s/c_L > 5$. When the concentration ratio decreased below 5, a fluid-like amorphous phase was observed¹⁰. However, in the study, tens of mixtures with discrete compositions were prepared while by our method, only one single sample with a continuous concentration ratio was required.

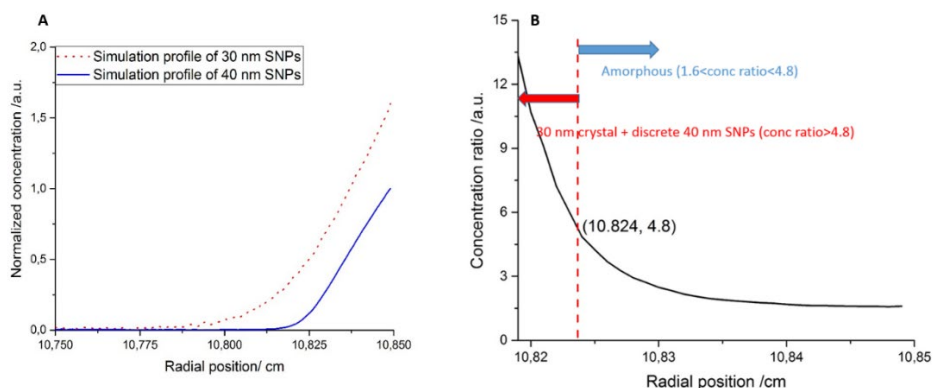


Figure 2.4: Normalized simulated concentration gradients for the 10 vol% binary mixture of 30 nm and 40 nm SNPs in a concentration ratio of 4:1 at 2800 rpm, 25 °C (A). The phase diagram of the binary mixture of 30 nm and 40 nm SNPs by means of continuous observations of the sediment along the radius (B). The concentration ratio in the transition position was determined by measuring the distance from the meniscus.

2.3. Conclusion

In conclusion, we were able to measure monodisperse and binary colloidal nanoparticle concentration gradients in the AUC by the synthesis of fluorescent labeled sterically stabilized silica nanoparticles, the employment of refractive index matching solvents, the application of turbidity correction procedures and the use of a multi-wavelength analytical ultracentrifuge (MWL-AUC). The concentration gradients of moderately (circa 2 vol%) concentrated colloids were fitted with the SEDFIT to obtain the necessary parameters including the sedimentation coefficient s , the diffusion coefficient D as well as the non-ideality coefficients k_s and k_D for subsequent simulations of the concentration gradients. The simulations proved to be valid even for very high particle concentrations up to 30 vol%. In the future, an even higher concentration may be studied to check the simulation validity limit. With this knowledge, we are now able to simulate and tailor-make binary colloidal nanoparticle concentration gradients in a centrifugal field. Moreover, the simulated concentration gradients can be used to correlate with different binary nanoparticle phases along the centrifugal field so that a continuous and extended binary nanoparticle phase diagram can be obtained simply by studying one single PUC experiment sample by SEM. In the future we will study size ratios with a richer phase behavior, especially in the size ratio regime 0.5 – 0.6^{10, 35}. These studies will help to explore a large variety of binary nanoparticle phases including different crystalline and amorphous structures, which can be formed simultaneously using PUC, in one single sample. The simulations of the concentration

gradients can be applied if the colloids can be treated as hard spheres. Moreover, nanoparticles of different shapes such as rod-like, platelet-like can be studied using the same methodology. In principle, different shapes affect the frictional ratio (f/f_0), which in turn influences the sedimentation and diffusion coefficients (s and D). These two coefficients can be determined by AUC-SV experiments shown in **SI4** and are input parameters for the simulations. Overall, our study of binary nanoparticle concentration gradients in a centrifugal field at high concentration shows a promising future in the research on the phase diagram in a continuous and handy manner for nanoparticle mixtures of multiple different sizes.

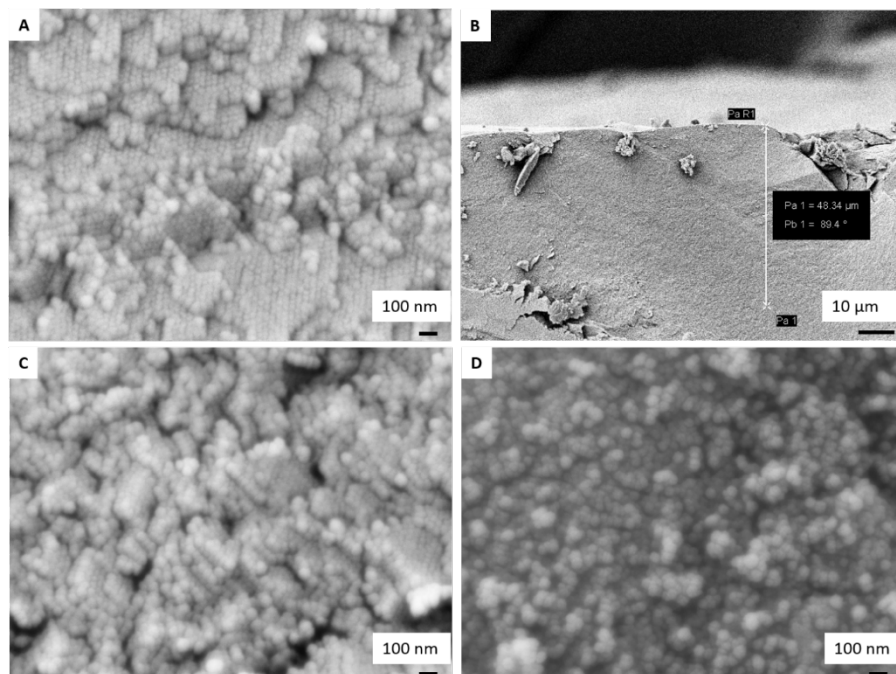


Figure 2.5: The represented SEM micrograph of the upper part in the sediment cross-section structures (A). The overview of the transition position where the last piece of crystalline phase was observed ($\approx 50 \mu\text{m}$ from the meniscus, $R = 10.824 \text{ cm}$) and the radial position was determined by measuring its distance from the meniscus (B). The zoom-in SEM micrograph of the transition position (C). The represented SEM micrograph of the binary nanoparticle packing phase below the transition position (D).

2.4. References

1. Leunissen, M. E.; Christova, C. G.; Hynninen, A. P.; Royall, C. P.; Campbell, A. I.; Imhof, A.; Dijkstra, M.; van Roij, R.; van Blaaderen, A., Ionic colloidal crystals of oppositely charged particles. *Nature* **2005**, *437* (7056), 235-40.
2. Chen, M.; Cölfen, H.; Polarz, S., Centrifugal field-induced colloidal assembly: From chaos to order. *ACS Nano* **2015**, *9* (7), 6944-50.

CHAPTER 2

3. Shevchenko, E. V.; Talapin, D. V.; Kotov, N. A.; O'Brien, S.; Murray, C. B., Structural diversity in binary nanoparticle superlattices. *Nature* **2006**, *439* (7072), 55-9.
4. Dong, A.; Chen, J.; Vora, P. M.; Kikkawa, J. M.; Murray, C. B., Binary nanocrystal superlattice membranes self-assembled at the liquid–air interface. *Nature* **2010**, *466*, 474.
5. Meder, F.; Thomas, S. S.; Bollhorst, T.; Dawson, K. A., Ordered surface structuring of spherical colloids with binary nanoparticle superlattices. *Nano Letters* **2018**, *18* (4), 2511-2518.
6. Mann, S., Self-assembly and transformation of hybrid nano-objects and nanostructures under equilibrium and non-equilibrium conditions. *Nature Materials* **2009**, *8*, 781.
7. Lu, P. J.; Weitz, D. A., Colloidal particles: Crystals, glasses, and gels. *Annual Review of Condensed Matter Physics* **2013**, *4* (1), 217-233.
8. Schuck, P.; Zhao, H.; Brautigam, C. A.; Ghirlando, R., *Basic principles of analytical ultracentrifugation*. CRC Press: 2016.
9. Fujita, H., *Foundations of ultracentrifugal analysis*. Wiley: 1975.
10. Hunt, N.; Jardine, R.; Bartlett, P., Superlattice formation in mixtures of hard-sphere colloids. *Physical Review E* **2000**, *62* (1), 900-913.
11. Royall, C. P.; Vermolen, E. C.; van Blaaderen, A.; Tanaka, H., Controlling competition between crystallization and glass formation in binary colloids with an external field. *Journal of Physics: Condensed Matter* **2008**, *20* (40), 404225.
12. Pearson, J.; Walter, J.; Peukert, W.; Cölfen, H., Advanced multiwavelength detection in analytical ultracentrifugation. *Analytical Chemistry* **2018**, *90* (2), 1280-1291.
13. Lamm, O., Zur theorie und methodik der ultrazentrifugierung. *Zeitschrift für Physikalische Chemie* **1929**, *143* (1), 177-190.
14. Schuck, P., Size-distribution analysis of macromolecules by sedimentation velocity ultracentrifugation and lamm equation modeling. *Biophysical Journal* **2000**, *78* (3), 1606-19.
15. Van Blaaderen, A.; Vrij, A., Synthesis and characterization of colloidal dispersions of fluorescent, monodisperse silica spheres. *Langmuir* **1992**, *8* (12), 2921-2931.
16. Watanabe, R.; Yokoi, T.; Kobayashi, E.; Otsuka, Y.; Shimojima, A.; Okubo, T.; Tatsumi, T., Extension of size of monodisperse silica nanospheres and their well-ordered assembly. *Journal of Colloid and Interface Science* **2011**, *360* (1), 1-7.
17. Ma, K.; Mendoza, C.; Hanson, M.; Werner-Zwanziger, U.; Zwanziger, J.; Wiesner, U., Control of ultrasmall sub-10 nm ligand-functionalized fluorescent core–shell silica nanoparticle growth in water. *Chemistry of Materials* **2015**, *27* (11), 4119-4133.
18. Verhaegh, N. A. M.; Vanblaaderen, A., Dispersions of rhodamine-labeled silica spheres - synthesis, characterization, and fluorescence confocal scanning laser microscopy. *Langmuir* **1994**, *10* (5), 1427-1438.
19. Yokoi, T.; Sakamoto, Y.; Terasaki, O.; Kubota, Y.; Okubo, T.; Tatsumi, T., Periodic arrangement of silica nanospheres assisted by amino acids. *Journal of the American Chemical Society* **2006**, *128* (42), 13664-13665.
20. Ma, K.; Zhang, D.; Cong, Y.; Wiesner, U., Elucidating the mechanism of silica nanoparticle pegylation processes using fluorescence correlation spectroscopies. *Chemistry of Materials* **2016**, *28* (5), 1537-1545.

21. Ow, H.; Larson, D. R.; Srivastava, M.; Baird, B. A.; Webb, W. W.; Wiesner, U., Bright and stable core-shell fluorescent silica nanoparticles. *Nano Letters* **2005**, *5* (1), 113-117.
22. Herz, E.; Ow, H.; Bonner, D.; Burns, A.; Wiesner, U., Dye structure-optical property correlations in near-infrared fluorescent core-shell silica nanoparticles. *Journal of Materials Chemistry* **2009**, *19* (35), 6341-6347.
23. Yethiraj, A.; van Blaaderen, A., A colloidal model system with an interaction tunable from hard sphere to soft and dipolar. *Nature* **2003**, *421* (6922), 513-517.
24. Maechtle, W.; Börger, L., *Analytical ultracentrifugation of polymers and nanoparticles*. Springer: Berlin ; New York, 2006; p xiii, 237 p.
25. Planken, K. L.; Cölfen, H., Analytical ultracentrifugation of colloids. *Nanoscale* **2010**, *2* (10), 1849-1869.
26. Laue, T.; Stafford III, W., Modern applications of analytical ultracentrifugation. *Annual review of biophysics and biomolecular structure* **1999**, *28* (1), 75-100.
27. Cole, J. L.; Lary, J. W.; Moody, T. P.; Laue, T. M., Analytical ultracentrifugation: Sedimentation velocity and sedimentation equilibrium. *Methods in Cell Biology* **2008**, *84*, 143-179.
28. Karabudak, E.; Cölfen, H., The multiwavelength uv/vis detector: New possibilities with an added spectral dimension. In *Analytical ultracentrifugation: Instrumentation, software, and applications*, Uchiyama S., A. F., Stafford W., Laue T., Ed. Springer, Tokyo: 2016.
29. Walter, J.; Löhr, K.; Karabudak, E.; Reis, W.; Mikhael, J.; Peukert, W.; Wohlleben, W.; Cölfen, H., Multidimensional analysis of nanoparticles with highly disperse properties using multiwavelength analytical ultracentrifugation. *ACS Nano* **2014**, *8* (9), 8871-8886.
30. Vistica, J.; Dam, J.; Balbo, A.; Yikilmaz, E.; Mariuzza, R. A.; Rouault, T. A.; Schuck, P., Sedimentation equilibrium analysis of protein interactions with global implicit mass conservation constraints and systematic noise decomposition. *Analytical Biochemistry* **2004**, *326* (2), 234-256.
31. Behlke, J.; Ristau, O., Analysis of the thermodynamic non-ideality of proteins by sedimentation equilibrium experiments. *Biophysical Chemistry* **1999**, *76* (1), 13-23.
32. Laue, T. M., [19] sedimentation equilibrium as thermodynamic tool. In *Methods in enzymology*, Elsevier: 1995; Vol. 259, pp 427-452.
33. Carney, R. P.; Kim, J. Y.; Qian, H.; Jin, R.; Mehenni, H.; Stellacci, F.; Bakr, O. M., Determination of nanoparticle size distribution together with density or molecular weight by 2d analytical ultracentrifugation. *Nature Communications* **2011**, *2*, 335.
34. Page, M. G.; Zemb, T.; Dubois, M.; Cölfen, H., Osmotic pressure and phase boundary determination of multiphase systems by analytical ultracentrifugation. *ChemPhysChem* **2008**, *9* (6), 882-890.
35. Bartlett, P.; Ottewill, R. H.; Pusey, P. N., Superlattice formation in binary mixtures of hard-sphere colloids. *Physical Review Letters* **1992**, *68* (25), 3801-3804.

2.5. Appendix

SI 1: The synthesis procedures of 30 nm and 40 nm fluorescent labeled PEG stabilized silica nanoparticles

(1) The synthesis procedure of 30 nm rhodamine isothiocyanate silica nanoparticles (RITC-SNPs):

A 50 ml glass reaction vessel was washed in a base bath for 60 min and subsequently rinsed by distilled water and ethanol. The cleaned vessel was finally dried in an oven for 60 min at 80 °C. In the vessel, 11.8 mg of RITC were added. 1 ml of dehydrated ethanol was then added at 400 rpm stirring. The vessel was degassed with Ar (g) for 5 min and then under continuous Ar (g) flow, 10 µl of 3-aminopropyltriethoxysilane (APS) were added. The reaction proceeded for 17 h in dark at 400 rpm stirring under Ar (g) protection.

A 50 ml three-neck flask was cleaned by the same procedure as above. Then 17 ml of water and 17.4 mg of arginine were added to the cleaned vessel. The above-synthesized APS-RITC conjugates were added by syringe under the solution surface at 600 rpm stirring. 1.11 ml of tetraethyl orthosilicate (TEOS) were then added slowly under the solution surface by syringe. The reaction proceeded at 70 °C for 24 h in dark at 700 rpm.

The average size of the synthesized RITC-SNPs was 30 nm (PDI = 0.4), characterized by dynamic light scattering (DLS). The synthesis of 40 nm (PDI = 0.3) fluorescein isothiocyanate (FITC)-SNPs was conducted using the same procedure with FITC and a different amount of TEOS addition (1.54 ml).

(2) Steric stabilization of 30 nm RITC-SNPs with trimethoxysilyl polyethylene glycol (PEG-silane):

7.5 mg of PEG-silane ($M_w = 1160$ Da) were added to 5 ml 3 mg/ml of 30 nm RITC-SNPs. The mixture was stirred at 500 rpm for 24 h. After that, the temperature was increased to 80 °C and the reaction proceeded for another 24 h without stirring. The steric stabilization of 40 nm FITC-SNPs was conducted using the same procedure with a different amount of PEG-silane addition (15 mg).

Fluorescein isothiocyanate (FITC, dye content $\geq 95\%$), rhodamine isothiocyanate (RITC), 3-aminopropyltriethoxysilane (APS, purity $\geq 99\%$), arginine and tetraethyl orthosilicate (TEOS, reagent grade, 98%) were purchased from Sigma-Aldrich. Trimethoxysilyl polyethylene glycol (PEG-silane, $M_w = 1160$ Da) was purchased from Gelest. All chemicals were used without any further purification.

SI 2: Images of the nanoparticle dispersions before and after refractive index matching and the calculation procedures to prove that the glycerol-water mixture formed a negligible density gradient in the AUC



Figure S1: The concentrated 30 nm RITC-SNPs dispersion in water (right) and in 80 vol% (83 wt%) glycerol and 20 vol% (17 wt%) water mixture (left). The SNP dispersion became nearly transparent by the refractive index matching.

To prove the density gradient formed by the glycerol water mixture (**Figure S2**) is negligible, **Equation S1**¹ was used:

$$\Delta c = \frac{J\lambda}{\frac{dn}{dc}a} \quad (\text{S1})$$

where J is the fringe difference between the meniscus and bottom of a AUC cell, Δc is the corresponding radial concentration difference, $\lambda = 675$ nm for the laser diode light source embedded in the Optima XLI, dn/dc was calculated² in **Figure S2B**. $a = 0.15$ cm for the thickness of the centerpiece used in the experiment. J was obtained from the experiment in **Figure S2A**, so by **Equation S1** the concentration difference plot was shown in **Figure S2C**. By knowing the hinge point shown in **Figure S2C**, the glycerol concentration gradient as a function of radius was plotted in **Figure S2D**. Then the dependence of the solvent density on glycerol concentration was shown in **Figure S2E**, obtained from the literature data². Therefore, the final density gradient was shown in **Figure S2F**. The density difference between the meniscus and the bottom was merely $0.0013 \text{ g}\cdot\text{cm}^{-3}$ ($1.2067 \text{ g}\cdot\text{cm}^{-3} - 1.2054 \text{ g}\cdot\text{cm}^{-3}$), so that the density gradient formed in the AUC at 2800 rpm could be neglected (the relative deviation of the density is only 0.1%).

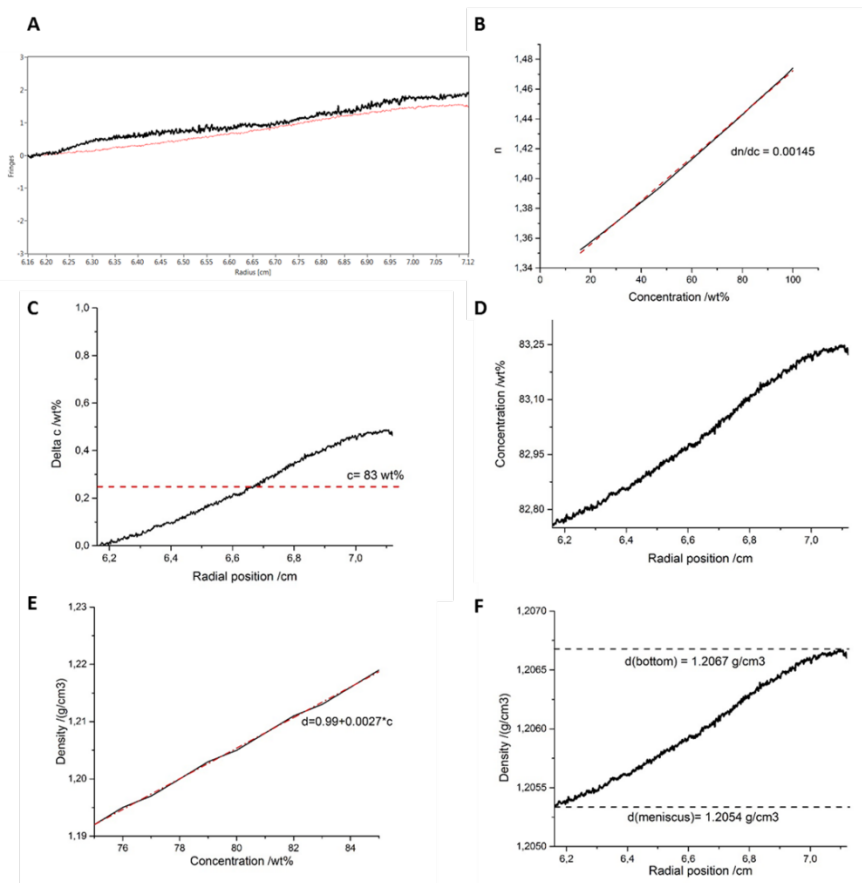


Figure S2: Interference profiles of the first scan (black) and the last scan (red) after 7 h 40 min of the 80 vol% glycerol and 20 vol% water mixture (= 83 wt% glycerol) with the reference water along the radius of an analytical ultracentrifuge (AUC) cell at 2800 rpm (A). Refractive index of the glycerol-water mixture as a function of the glycerol concentration (wt%) with the linear fitting (B). Δc of the mixture as a function of the radial position obtained by using **Equation S1** (C). Absolute concentration as a function of radial positions by knowing the hinge point (D). Density of the mixture as a function of the glycerol concentration (wt%) with the linear fitting (E). The final density gradient in the mixture from 6.16 cm to 7.12 cm (F).

SI 3: The detailed AUC sedimentation-diffusion equilibrium experimental set-up

In a typical sedimentation-diffusion equilibrium (AUC-SE) experiment, an AUC titanium centerpiece of 1.5 mm pathlength (**Figure S3**) was used. 3 μ l, 2 vol% of 30nm RITC-SNPs in 80 vol% glycerol and 20 vol% water (corresponding to 0.5 mm column length) were injected into the sample channel and 3 μ l of the 80 vol% glycerol and 20 vol% water mixtures were injected into the reference channel of the AUC cell by syringes

Hard-sphere-like colloids in a centrifugal field at high concentration

separately. The AUC cell was then assembled into a rotor and put into the chamber of a home-made Multi-Wavelength Analytical Ultracentrifuge (MWL-AUC). The measurement settings: Angular velocity 2800 rpm; Temperature 25 °C; Wavelength range 400 – 800 nm; Radial step size 10 μm ; Scan mode duplex; Scan interval: 3600 s. When the last 10 scans overlapped, the sedimentation-diffusion equilibrium was reached. The experiments of the other samples were performed with the same procedure.

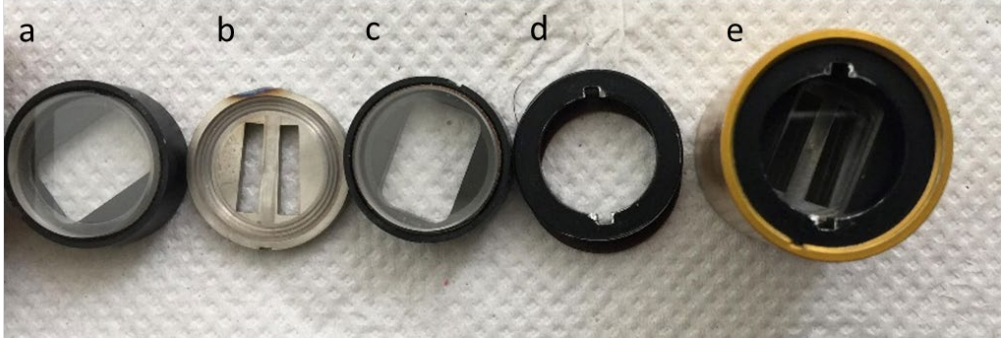


Figure S3: An AUC cell with a 1.5 mm pathlength centerpiece (e) and all the inside components including two window assemblies (a and c), a 1.5 mm pathlength titanium centerpiece (b) and a screw ring (d).

SI 4: The detailed fitting process

A typical fitting procedure includes two steps: 1) The sedimentation velocity (AUC-SV) experiment: 56 μl , 2 vol% of 30 nm RITC-SNPs in water were injected to fill the sample channel and 56 μl of water were injected to fill the reference channel of the AUC cell with a 1.5 mm pathlength centerpiece by syringes separately. The AUC cell was then assembled into a rotor and put into the chamber of the Optima XLI. The measurement settings: Angular velocity 6000 rpm; Temperature 25 °C; Scan interval: 60 s. When the sedimentation boundary reached the cell bottom, the experiment was stopped. The sedimentation coefficient (s) was obtained as a fixed value by using the ls-g*(s) model of the SEDFIT. The diffusion coefficient (D) was then obtained by the fitting the data with the c(s) with invariant D model of the SEDFIT (**Figure S4**). The corresponding s and D in 80 vol% glycerol and 20 vol% water mixture were finally calculated (2.7 S and $1.8 \times 10^{-9} \text{cm}^2 \cdot \text{s}^{-1}$ in values) by using the well-known Svedberg equation, as shown in **Equation S2** and Stokes-Einstein relation, as shown in **Equation S3**¹:

$$d_p = \sqrt{\frac{18\eta s}{(\rho_p - \rho_s)}} \quad (\text{S2})$$

$$D = \frac{k_B T}{6\pi\eta r} \quad (\text{S3})$$

CHAPTER 2

with d_p is the diameter of the spherical particle; η is the dynamic viscosity of the solvent; ρ_p is the particle density; ρ_s is the solvent density; k_B is Boltzmann's constant; T is the absolute temperature; r is the radius of the spherical particle.

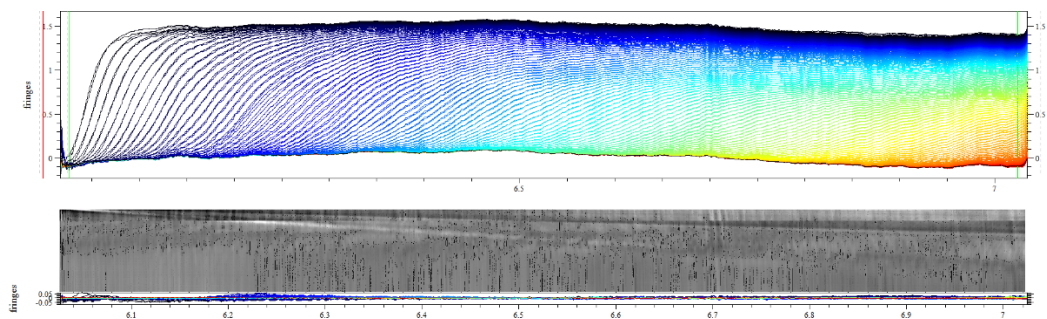


Figure S4: The fitting result of the AUC-SV data with the $c(s)$ with invariant D model in the Sedfit for 30 nm RITC-SNPs. Fitted $D = 1.33 \times 10^{-7} \text{cm}^2 \cdot \text{s}^{-1}$ in water ($= 1.8 \times 10^{-9} \text{cm}^2 \cdot \text{s}^{-1}$ in 80 vol% glycerol and 20 vol% water mixture) and fitting RMSD = 0.006920.

2) The AUC-SE experiment: After an AUC-SE experiment of 2 vol% of 30 nm RITC-SNPs described in SI3, the experimental concentration gradient was used to fit k_s and k_D by the non-ideal sedimentation model. The pre-determined s and D in step 1) were input in the model and set as fixed, and the best-fit non-ideality coefficients k_s and k_D were then obtained which are both $10^{-0.5}$ for 30 nm RITC-SNPs. The fitting procedures of 40 nm FITC-SNPs were performed in the same manner: $s = 5.9 \text{ S}$; $D = 1.2 \times 10^{-9} \text{cm}^2 \cdot \text{s}^{-1}$; $k_s = 10^{-0.5}$; $k_D = 10^{-0.5}$.

SI 5: The calculation procedures of the density (ρ) and molecular mass (M) for 30nm and 40nm SNPs

The density (ρ) and molecular mass (M) of 30 nm and 40 nm SNPs were calculated according to Equations S4 and S5³:

$$\rho_p = \rho_s + 18\eta_s s \left(\frac{1}{D} \frac{k_B T}{3\pi\eta_s} \right)^{-2} \quad (\text{S4})$$

$$M = \frac{sRT}{D} \left(1 - \frac{\rho_s}{\rho_p} \right)^{-1} \quad (\text{S5})$$

where the solvent density (ρ_s) equals $1.2 \text{ g} \cdot \text{cm}^{-3}$ and the viscosity (η_s) equals $8.4 \times 10^{-2} \text{ Pa} \cdot \text{s}$, the Boltzmann's constant (k_B) equals $1.38 \times 10^{-23} \text{ J} \cdot \text{K}^{-1}$ and the experimental temperature equals 298 K. The sedimentation coefficient (s) and the diffusion coefficient (D) were determined in SI4. By inserting the values of all these parameters into **Equation S4**, the nanoparticle density (ρ_p) was obtained. RT equals $2.48 \times 10^3 \text{ J} \cdot \text{mol}^{-1}$ in the experiment and by inserting the values of the solvent and nanoparticle densities (ρ_s and ρ_p), the nanoparticle diffusion coefficient (D) and the sedimentation coefficient (s) into **Equation S5**, the nanoparticle molecular mass (M) was obtained. In **Table S1**, the calculated densities for 30

Hard-sphere-like colloids in a centrifugal field at high concentration

nm and 40 nm SNPs were both slightly smaller than the literature value ($1.8 \text{ g}\cdot\text{cm}^{-3}$)⁴ due to the presence of the short length PEG chains. The density of the 30 nm SNPs was yet smaller than that of 40 nm SNPs because the weight ratio of the surface PEG was higher for the smaller nanoparticles. The calculated molecular masses agreed with the theoretical values with an acceptable relative deviation (< 0.1). These results proved that the parameters were valid for the subsequent simulations.

SNP	30 nm SNPs	40 nm SNPs
s (S)	2.7	5.9
D ($10^{-9} \text{ cm}^2\cdot\text{s}^{-1}$)	1.8	1.2
ρ ($\text{g}\cdot\text{cm}^{-3}$)	1.64	1.77
Theoretical ρ ($\text{g}\cdot\text{cm}^{-3}$)	1.8	1.8
M (MDa)	14	39
Theoretical M (MDa)	15	36

Table S1: The calculation results for the particle density (ρ) and molecular mass (M) of 30 nm RITC-SNPs and 40 nm FITC-SNPs to verify the values of s and D . The theoretical M was calculated from multiplying the nanoparticle density ($1.8 \text{ g}\cdot\text{cm}^{-3}$)⁴ with the nanoparticle volume (approximated as a spherical). The relative deviations of the calculated densities compared with the theoretical values are 0.08 and 0.02 for 30 nm and 40 nm SNPs separately. The relative deviations of the calculated molecular masses compared with the theoretical values are 0.07 and 0.08 for 30 nm and 40 nm SNPs separately.

SI 6: The calculation procedures of separate nanoparticle concentrations from the absorbance spectra of the binary nanoparticle mixture

It is vital to calculate separate concentrations of the two nanoparticles from one absorbance spectrum (**Figure S5**) by MWL-AUC. The two peak wavelengths, namely at 490 nm and 550 nm were not used here simply because at higher concentrations, their absorbance values easily exceeded the linearity range of the Lambert-Beer law. Instead, the following strategy was adopted: the absorbance plateau at a larger wavelength (700 nm – 800 nm) was treated as the baseline absorbance. Since the absorbance at 580 nm was only contributed by 30 nm RITC-SNPs, it could be used to calculate the concentration of 30 nm RITC-SNPs. The absorbance value at 520 nm minus the absorbance contribution from RITC-SNPs was used to calculate the concentration of FITC-SNPs. By this strategy, a larger amount of data can be collected at high concentrations rather than simply using two peak wavelengths. Only absorbance values lower than 1.4 were used in the data analysis to comply with the linearity of the Lambert-Beer law. By this way, the individual nanoparticle concentrations for the both species in all radial positions were obtained.

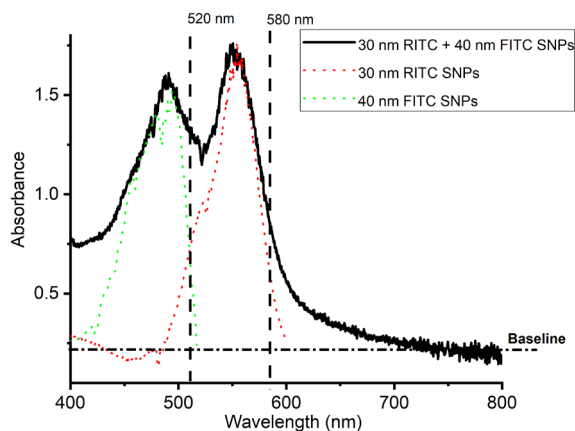


Figure S5: The UV-vis absorbance spectra in the wavelength range from 400 nm to 800 nm for 40 nm FITC-SNPs (green dotted), 30 nm RITC-SNPs (red dotted) and the binary mixture (black solid). The absorbance values at 520 nm, 580 nm were read to calculate the nanoparticle concentrations in all radial positions.

SI 7: Another simulation result of the binary case with a volume ratio of 1:1

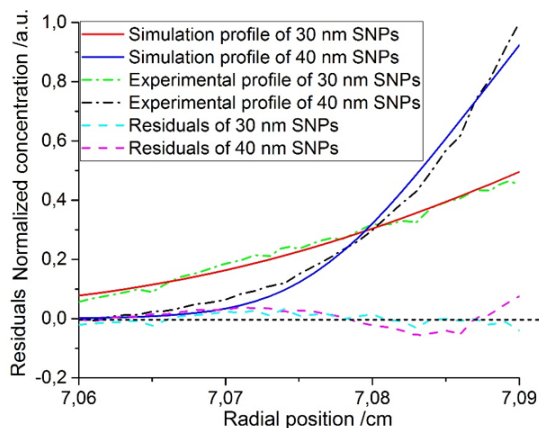


Figure S6: The normalized simulation (solid lines) and experimental (dash dot lines) concentration gradients for 10 vol% binary mixtures of 30 nm RITC-SNPs and 40 nm FITC-SNPs in a volume ratio of 1:1 at 2800 rpm, 25 °C. The dashed lines are the residuals of the fit and the experimental data. The experimental concentration profiles were normalized to the same range as the simulations. RMSD = 0.017 and 0.031 for the agreement of the experiments with the simulations.

SI 8: The turbidity correction procedure

The turbidity was corrected by applying Rayleigh scattering⁵ where the intensity of scattered light is proportional to the inverse fourth power of the wavelength. Practically, of a UV-vis spectrum in **Figure S7A** the wavelength range where the light was not absorbed due to RITC and FITC (300 nm to 400 nm and 620 nm to 700 nm) was selected for the fitting by absorption = constant/ λ^4). After that, the fitted scattering curve was subtracted from the raw data (Figure S6A). By this way, the turbidity effect was corrected from the raw data. This procedure was only applied at high concentrations while at a radius where the concentration was not that high, the turbidity effect was ignorable (**Figure S7B**).

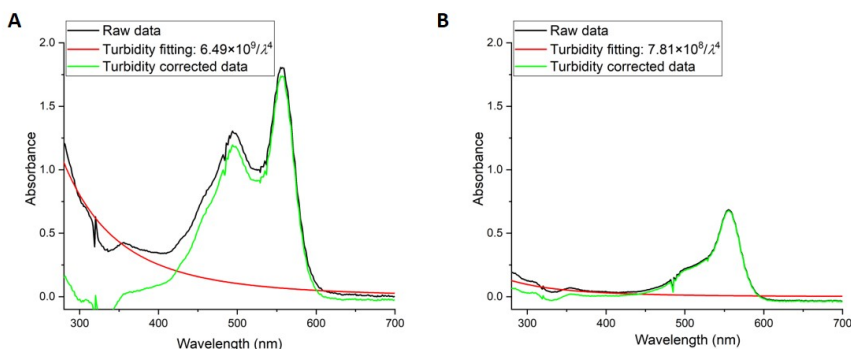


Figure S7: Two examples of the turbidity correction result. The turbidity corrected data (Green curve) was obtained by subtracting the turbidity fitting curve (Red curve) from the raw data (Black curve). The turbidity effect was ignorable at a smaller radius, when the concentration was not very high (B).

SI 9: The confocal laser scanning microscope (CLSM) experiment to prove the validity of simulations in PUC

2 μ l, 10 vol% binary mixtures of 30 nm RITC-SNPs and 40 nm FITC-SNPs in a volume ratio of about 1:2 were confined in a glass capillary (1 mm \times 1 mm, VitroCom)⁶. The one end of the capillary was glued and cured overnight in ambient conditions. The capillary was then inserted into a home-made adaptor inside a centrifuge tube for the Beckman swing out rotor SW-55 Ti. The sample was centrifuged at 2800 rpm, 25 $^{\circ}$ C in an L-70 preparative ultracentrifuge (PUC) for 10 days to reach the final sedimentation-diffusion equilibrium. After the centrifugation, the sample was quickly taken out and put into CLSM (Zeiss LSM 880) for the observation at the transmission mode. The laser light beams with the wavelength 488 nm and 561 nm were chosen to separately measure the approximate concentration of 40 nm FITC-SNPs and 30 nm RITC-SNPs. The experimentally measured absorbance/concentration gradients were normalized to compare with the simulation, which showed a good agreement (**Figure S8**).

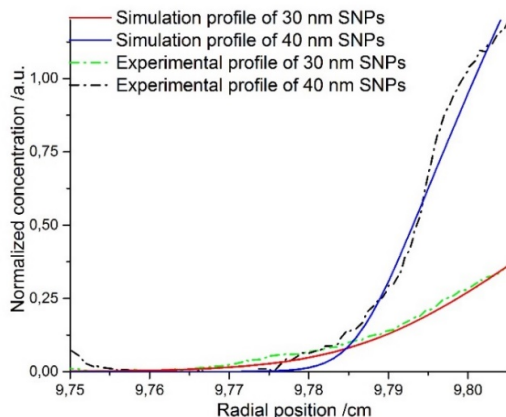


Figure S8: The normalized simulation (solid lines) and experimental (dash dot lines) concentration gradients for 10 vol% binary mixtures of 30 nm RITC-SNPs and 40 nm FITC-SNPs in a volume ratio of about 1:2 at 2800 rpm, 25 °C in a L-70 preparative ultracentrifuge (PUC). The absorbance gradients were measured by confocal laser scanning microscopy (CLSM) at the wavelength of 488 nm and 561 nm in transmission mode.

SI10: The PUC experiment and sample preparation for SEM

10 μ l, 10 vol% binary mixtures of 30 nm RITC-SNPs and 40 nm FITC-SNPs in a volume ratio of 4:1 were loaded into an ultra-clear (5 \times 41 mm) centrifuge tube. The centrifuge tube was inserted into the Beckman swing out rotor SW 55 Ti. The centrifuge was run at 2800 rpm, 25 °C for 7 h to reach the sedimentation-diffusion equilibrium (7 h was enough to reach the equilibrium according to the Sedfit simulation since in water both the sedimentation and diffusion process became much faster than in the glycerol-water mixture). The sample was placed in a desiccator with silica gel for drying overnight after the centrifugation. The dried sediment was cut by a razor blade along the cross-section direction (**Figure S9**) and then the cross-section structures along the centrifugal field were investigated by using a Zeiss 249 Cross-Beam 1540XB scanning electron microscope.

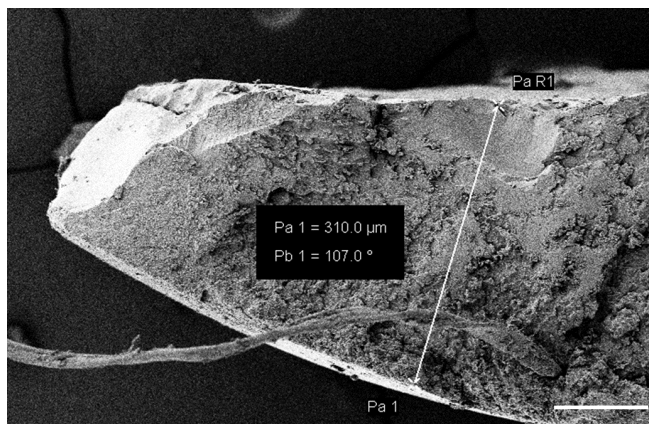


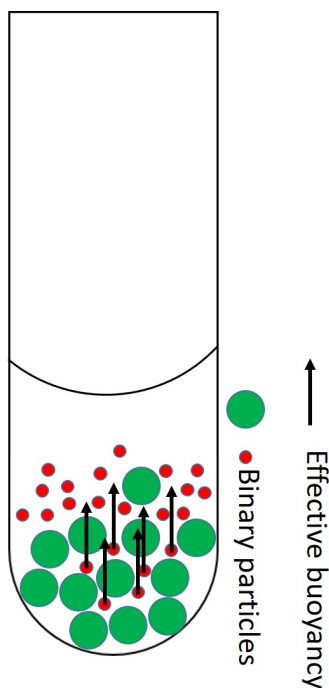
Figure S9: The cross-section structure overview of the sediment after the cut by a razor blade. The cross-section structures along the centrifugal field (marked by the white line of 310 μm in length) were investigated. The hanging long dust flied around, but it did not disturb the observation. Scale bars = 100 μm .

References

1. Maechtle, W.; Börger, L., *Analytical ultracentrifugation of polymers and nanoparticles*. Springer: Berlin ; New York, 2006; p xiii, 237 p.
2. Association, G. P., *Physical properties of glycerine and its solutions*. Glycerine Producers' Association: 1963.
3. Carney, R. P.; Kim, J. Y.; Qian, H.; Jin, R.; Mehenni, H.; Stellacci, F.; Bakr, O. M., Determination of nanoparticle size distribution together with density or molecular weight by 2d analytical ultracentrifugation. *Nature Communications* **2011**, *2*, 335.
4. Van Blaaderen, A.; Vrij, A., Synthesis and characterization of colloidal dispersions of fluorescent, monodisperse silica spheres. *Langmuir* **1992**, *8* (12), 2921-2931.
5. Barnett, C. E., Some applications of wave-length turbidimetry in the infrared. *The Journal of Physical Chemistry* **1942**, *46* (1), 69-75.
6. Leunissen, M. E.; Christova, C. G.; Hynninen, A.-P.; Royall, C. P.; Campbell, A. I.; Imhof, A.; Dijkstra, M.; Van Roij, R.; Van Blaaderen, A., Ionic colloidal crystals of oppositely charged particles. *Nature* **2005**, *437* (7056), 235.

CHAPTER 3

Binary Hard Spheres with a Large Size Ratio in a Centrifugal Field



The results described in this chapter are based on:

Xufeng Xu, Helmut Cölfen*. Binary Colloidal Nanoparticles with a Large Size Ratio in Analytical Ultracentrifugation. *ChemPhysChem* 2019, 20 (14), 1799-1803.

3. Binary hard spheres with a large size ratio in a centrifugal field

Sedimenting colloidal particles may feel a surprisingly strong buoyancy in a mixture with other particles of a considerably larger size. In this chapter we investigated the buoyancy of colloidal particles in a concentrated binary suspension *in situ* in a centrifugal field. After dispersing two different fluorescent labeled silica nanoparticles with a large size ratio (90 nm and 30 nm, size ratio = 3) in a refractive index matching solvent, we used a multi-wavelength analytical ultracentrifuge to measure the concentration gradients of both particles *in situ*. The concentration of 90 nm silica nanoparticles was used to calculate the effective solvent density for 30 nm silica nanoparticles. The exponential Boltzmann equation for the sedimentation-diffusion equilibrium with locally varying effective solvent density was then used to theoretically predict the concentration gradient of 30 nm silica nanoparticles, which describes the experimental results very well. This finding proves the validity of effective buoyancy in colloidal mixtures and provides a good model to study sedimenting polydisperse colloids.

3.1. Introduction

Colloidal particles in a natural settling are mostly of high polydispersity as species of varied sizes are dispersed in the same suspension. These polydisperse systems are nonetheless capable of remarkable self-organization, including the formation of crystalline structures such as opals¹ or demixing into different layers of higher monodispersity²⁻⁴. In recent years, researchers have been investigating colloidal mixtures of different sizes⁵⁻⁷ to model natural polydisperse colloidal particle behavior in settling processes. It was found that by carefully tuning the size ratio colloidal mixtures of two different sizes may form a variety of binary crystalline structures⁸⁻¹⁰ inspired by the opal formation¹¹. Several unexpected physical phenomena¹²⁻¹³ were also observed when the colloidal particles of different sizes settled in the dispersion. The standard Archimedes principle might even become invalid as it was found that the solvent density felt by particles may change due to the presence of other particles¹⁴. Due to the solvent density change, the smaller particles in the suspension may even be levitated, which is known as effective buoyancy¹⁵.

The effective buoyancy was theoretically investigated by Biesheuvel et al. and Piazza et al.¹⁶⁻¹⁷. They studied the behavior of a sedimenting colloidal particle mixture of unequal sizes and found that the bigger particles in the mixture contributed to the effective solvent density felt by the smaller particles. As the effective solvent density increased with the concentration of the bigger particles, it even became possible for the smaller particles to be levitated in a dispersion of concentrated bigger particles. In the sedimentation-diffusion equilibrium the total force acting on the particles was cancelled out, which was expressed in **Equation 3.1**. The osmotic pressure gradient was described as given in **Equation 3.2** by modifying the Gibbs-Duhem (GD) equation¹⁸.

$$F_i^{tot} = \frac{k_B T}{\varphi_i} \frac{\partial \varphi_i}{\partial r} - \frac{\partial \mu_i^{exc}}{\partial r} - v_i (\rho_i - \rho_F) g = 0 \quad (3.1)$$

Binary hard spheres with a large size ratio in a centrifugal field

$$\frac{\partial \Pi}{\partial r} = -g(\rho_{\text{susp}} - \rho_{\text{F}}) \quad (3.2)$$

$$\rho_{\text{susp}} = \rho_{\text{F}} + \sum_i \varphi_i (\rho_i - \rho_{\text{F}}) \quad (3.3)$$

where F_i^{tot} is the total force acting on the particle, φ_i , v_i and μ_i^{exc} are the volume fraction, volume and excess chemical potential of species i , ρ_i , ρ_{susp} and ρ_{F} are the density of species i , suspension and pure fluid respectively, Π is the osmotic pressure, r is a radial position, g is the acceleration due to gravity. As shown in **Equation 3.3**, ρ_{susp} is the volume average density of a mixture, averaging over all the particle types and the fluid. Experimentally, Piazza et al. used a quite simple and intuitive turbidity measurement for a very diluted dispersion of a copolymer fluid of poly-tetrafluoroethylene and gold particles to test the theory¹⁷. This buoyancy of small particles in a centrifugal field was also found by Chen et al.¹⁹. She observed that after the sedimentation of a binary mixture of polystyrene nanoparticles (150 nm and 300 nm), it became difficult to spot the smaller nanoparticles at the bottom of the sediment. The reason for this might be that most of the smaller nanoparticles were lifted to the upper part of the sediment. More specifically, near the bottom the high concentration of the bigger nanoparticles increased the effective solvent density dramatically, which then induced a strong buoyancy felt by the smaller nanoparticles. Besides the theoretical and limited experimental work, there is still a lack of thorough and quantitative investigation of the buoyancy effect in a concentrated binary colloidal nanoparticle suspension. In this paper, we dispersed two different fluorescent labeled (fluorescein isothiocyanate (FITC) and rhodamine B isothiocyanate (RITC)) silica nanoparticles (SNPs) in a refractive index matching solvent of 80 vol% glycerol and 20 vol% water so that we could measure the separate concentrations of the binary SNPs of a large size ratio (90 nm and 30 nm, size ratio = 3) at a total concentration as high as 10 vol% using a multi-wavelength (MWL) UV-Vis detector²⁰⁻²² embedded in the analytical ultracentrifuge (AUC). A centrifugal field was applied to the binary SNPs suspension and, after the sedimentation-diffusion equilibrium²³ (AUC-SE) was reached, the individual concentration gradients were measured for the two different nanoparticle species using a procedure described in a recent publication²⁴. It was observed that at some radial position, the buoyancy of 30 nm RITC-SNPs started to appear and proceeded. This was demonstrated by a flattening of the concentration gradient with increasing concentration of 90 nm FITC-SNPs. Quantitatively speaking, using the generalized Archimedes' principle (GAP) by Piazza et al.^{15, 17}, the effective density was calculated based on the concentration of 90 nm FITC-SNPs. The calculated effective density was then plugged into the exponential concentration distribution²⁵⁻²⁶. By these means the concentration gradient of 30 nm RITC-SNPs can be effectively buoyancy corrected. In this way the buoyancy effect was theoretically predicted, and the calculated concentration gradient agreed with the experimental data. Our binary SNPs of a large size ratio in a concentrated suspension, therefore, provide a good model to study polydisperse colloidal particle behavior in a centrifugal field or in natural sedimentation.

3.2. Results and discussion

We first analyzed the concentration gradients of the monodisperse dispersions of 90 nm FITC-SNPs and 30 nm RITC-SNPs, respectively, in AUC-SE experiments. For a very diluted dispersion, the dispersion behaves ideally²⁷ and the resulting concentration gradient in the AUC-SE simply follows the exponential concentration distribution²⁸. At a higher concentration, the second osmotic virial coefficient B_2 needs to be included in the exponential equation to account for the non-ideality²⁷. For diluted 30 nm and 90 nm SNPs dispersions with concentrations as low as 0.5 vol%, **Equation 3.4** and **3.5** were used to fit the experimental concentration profile²⁸:

$$c(r) = c(r_1) \exp\left(\frac{r^2 - r_1^2}{2L_\omega^2}\right) \quad (3.4)$$

$$L_\omega = \sqrt{\frac{k_B T}{v(\rho_p - \rho_s)\omega^2}} \quad (3.5)$$

where r is an arbitrary radial position and $c(r)$ is the corresponding nanoparticle concentration, r_1 is a reference radial position and $c(r_1)$ is the corresponding nanoparticle concentration, L_ω is the so-called centrifugal length, ρ_p is the colloidal particle density, ρ_s is the solvent density, v is the volume of one particle, ω is the angular velocity of the ultracentrifuge and $k_B T$ is the product of Boltzmann's constant k_B and temperature T .

In **Figure 3.1A** the data was fitted using Equation (4) and $L_\omega = 0.153$ cm was converted to the particle diameter $d = 87.6$ nm by using Equation (5). The particle diameter independently measured by scanning electron microscopy (SEM) in **Figure S1** is 84.0 ± 7.7 nm. The size distribution from the two independent measurements agreed with the relative deviation of ca. 4%. In **Figure 3.1B**, the fitted particle diameter $d = 33.7$ nm deviated ca. 10% from the size ($= 30$ nm) measured by the sedimentation velocity experiment (AUC-SV) in our previous publication 24. The concentration gradient of a SNPs dispersion of a concentration as high as up to 30 vol% could be fitted with non-ideality including exponential Boltzmann distribution²⁹. This is how it was possible to obtain the knowledge about the second virial coefficient B_2 ²⁴. Overall, the exponential Boltzmann distribution worked well when using the constant solvent density ($1.2 \text{ g}\cdot\text{cm}^{-3}$ for the glycerol and water mixture) for the monodisperse dispersions of 90 nm and 30 nm SNPs.

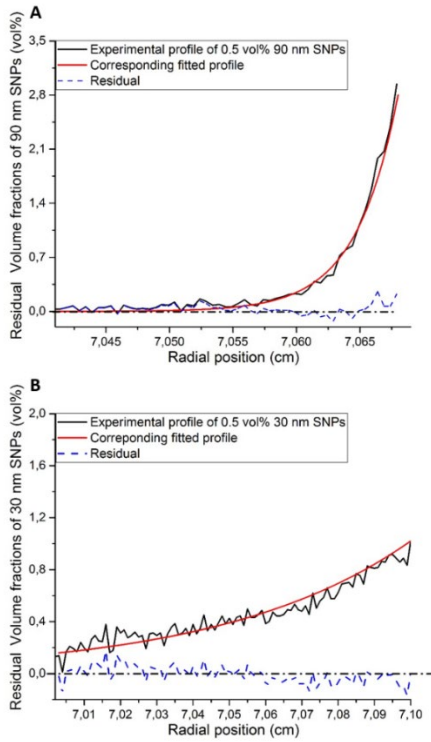


Figure 3.1: Experimental (black line) and fitted (red line) concentration gradients for A) 90 nm SNPs and B) 30 nm SNPs of 0.5 vol% in an AUC at 1100 rpm, 25 °C. The blue dashed lines indicate the residuals, which equal the difference of experimental and fitted data.

Proceeding to the binary suspension of 30 nm and 90 nm SNPs at a high concentration (1 vol% and 9 vol% separately and 10 vol% in total), the solvent density could not be considered constant anymore because under these conditions the effective buoyancy needed to be considered. Before the effective buoyancy was applied, its limits of validity were examined¹⁷: 1) 30 nm SNPs could be treated as nearly hard spheres (shown in reference 24) and at concentrations as low as 1 vol% the self-interaction could be totally neglected; 2) The centrifugal length of 90 nm SNPs ($L_\omega = 0.153$ cm) was much larger than both the radius of 30 nm and 90 nm SNPs; 3) Transport processes are totally avoided in an AUC-SE experiment. When these three constraints are satisfied, the GAP theory¹⁷ can be applied.

The fitting procedure consisted of the following two steps: Step 1 was the calculation of the effective density (ρ^*) using the Generalized Archimedes' principle (GAP). Since the binary suspension satisfied the three constraints of the GAP and the size ratio was relatively high, **Equations 3.6, 3.7** and **3.8**¹⁷ were applied:

$$\rho^* - \rho = q^3 f(\varphi_2) m_2' n_2 \quad (3.6)$$

$$f(\varphi_2) = (1 - \varphi_2)^3 / (2 \times (4 - \varphi_2)\varphi_2 + (1 - \varphi_2)^4) \quad (3.7)$$

$$m_2' = (\rho_2 - \rho)v_2 \quad (3.8)$$

where ρ is the solvent density, ρ_2 is the silica nanoparticle density²⁸, q is the size ratio, φ_2 is the volume fraction of 90 nm SNPs, v_2 is the particle volume, n_2 is the number density of 90 nm SNPs

By these means, the effective density ρ^* was calculated from the volume fraction of 90 nm SNPs (φ_2) in **Figure S2**. In **Figure 3.2** the effective (solvent) density and the constant solvent density were compared. The constant solvent density remained unchanged irrespective of the presence of multiple particles while the effective density was calculated based on the concentration of 90 nm SNPs.

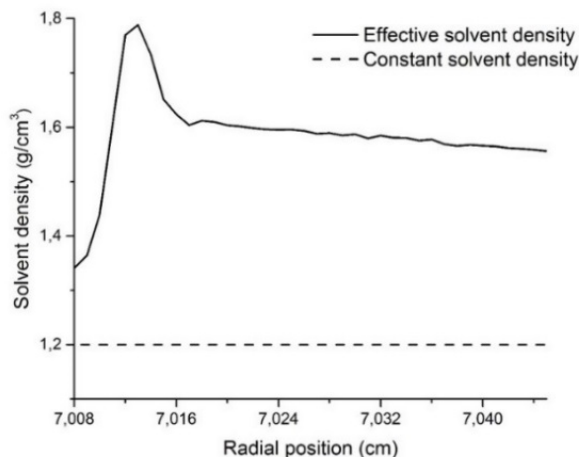


Figure 3.2: The calculated effective solvent density (solid line) and the constant solvent density (dashed line).

In **Step 2**, the effective density (ρ^*) modified exponential Boltzmann distribution was used:

$$c_r = c_0 * \exp \left(M \frac{\omega^2 (r^2 - r_0^2)}{2RT} \right) \quad (3.9)$$

$$M = M_p (1 - \rho v_{\text{bar}}) \quad (3.10)$$

where r is an arbitrary radial position and c_r is the corresponding nanoparticle concentration, r_0 is a reference radial position, c_0 is the corresponding nanoparticle concentration, ω is the angular velocity of the ultracentrifuge, M is the buoyant molar mass, M_p is the particle mass,

v_{bar} is the partial specific volume of the SNPs and RT the product of the gas constant R and temperature T .

Finally, the two concentration gradients, using the constant density and effective density separately, were plotted in **Figure 3.3**. In **Figure 3.3A**, when a fixed solvent density of $1.2 \text{ g}\cdot\text{cm}^{-3}$ was applied, we found that the fitted concentration gradients agreed with the experimental profile trend in the meniscus region. However, it predicted an exponential increase which deviated severely from the flatter experimental gradient in regions closer to the bottom. In comparison, when the effective density was used, the resulting flattened concentration gradient yielded a good fit near the bottom part of the cell, but a small discrepancy between the fitted profile and experimental data was found in the meniscus region. This might result from a dramatically increasing concentration of 90 nm SNPs in this region and the associated strong hard sphere repulsion with 30 nm SNPs (**Figure S2**). **Figure 3.3B** was plotted to demonstrate that when using the fixed solvent density, $\ln(\text{concentration})$ followed a straight line with $r^2 - r_0^2$, while after taking into account the effective density a much flattened gradient was predicted for the bottom of the cell which agreed better with the experiment as compared to the one for constant density. Another binary suspension with different concentrations in a centrifugal field with a different angular velocity is shown in **Figure S3**. The flattened part near the bottom also agreed well with experimental data by considering the effective buoyancy. The disagreement of theory and experiment in the meniscus region was also reduced when the concentration of 90 nm SNPs was lowered to 3 vol%, suppressing the hard sphere repulsion between 30 nm and 90 nm SNPs. Therefore, these two examples demonstrated that by calculating the effective density using the concentration of 90 nm SNPs and replacing the constant solvent density with the varying effective value in the Boltzmann distribution, the effective buoyancy can be considered in the binary colloidal system of 30 nm and 90 nm SNPs. Overall, the unusually flattened concentration gradient of 30 nm SNPs compared to the expected one was well fitted by employing this method. However, the effective buoyancy could not be applied to 90 nm SNPs due to their relatively high concentration and accordingly significant interparticle interaction. Moreover, the effective density felt by 90 nm SNPs was insignificant due to the low concentration of 30 nm SNPs. When using **Equation 3.11** in reference 17, the effective density (ρ^*) nearly equaled the pure solvent density (ρ), considering $q = 1/3$ and φ_2 was as low as only 0.01.

$$\rho^* - \rho = (1 + q)^3(\rho_2 - \rho)\varphi_2 \quad (3.11)$$

3.3. Conclusion

In summary, a binary mixture of fluorescent labeled 30 nm and 90 nm SNPs was dispersed in a refractive index matching solvent of 80 vol% glycerol and 20 vol% water at a high total particle concentration (10 vol%) so that the concentrations of both particles could be obtained individually by measuring the absorbance spectra in an MWL UV-vis optics embedded AUC. By applying the principle of effective buoyancy³⁰, the constant solvent density was replaced by a locally varying density which depended on the local concentration

CHAPTER 3

of 90 nm SNPs. The calculated effective density was then plugged into the exponential Boltzmann distribution and the locally density-corrected concentration gradients of 30 nm SNPs were calculated. The theoretically calculated profile was a good fit for the experimental concentration profile. The good quality of the fitted result was demonstrated by plotting $\ln(\text{concentration})$ as a function of $r^2 - r_0^2$. When considering a fixed density, the plot was linear which clearly deviated from the experimental data, while using the effective density the flattened experimental gradient was predicted well, especially for the bottom part of the cell. These findings proved the validity of the effective buoyancy in a binary colloidal nanoparticle dispersion, especially of a large size ratio and at a high concentration. For settling colloidal dispersions in practical cases³¹⁻³², the size polydispersity and the concentration are normally both high. Thus, the effective density needs to be considered for the colloidal particle behavior. In conclusion, our investigated system and the results provide a good model to study sedimenting polydisperse colloidal particles in natural and industrial cases.

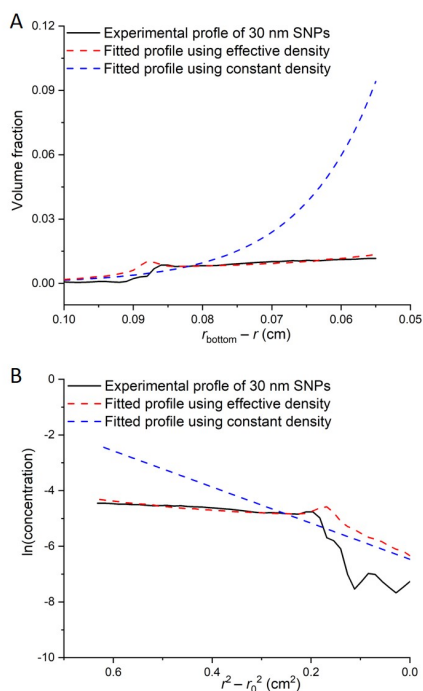


Figure 3.3: Experimental concentration profile (black line) for 30 nm SNPs in the binary suspension of 30 nm (1 vol%) and 90 nm (9 vol%) SNPs in an AUC at 2800 rpm, 25 °C. The fitted profiles for 30 nm SNPs using the constant solvent density (blue line) and the effective density (red line). Panel A shows the volume fraction as a function of $r_{\text{bottom}} - r$ and panel B shows $\ln(\text{concentration})$ as a function of $r^2 - r_0^2$, where $r_{\text{bottom}} - r$ is the distance from the cell bottom and r_0 is the meniscus radial position.

3.4. Experimental section

Synthesis of 30 nm and 90 nm fluorescent labeled silica nanoparticles (SNPs): The reaction vessels were cleaned and dried in an oven for further use. Rhodamine isothiocyanate (RITC) and aminopropyltriethoxysilane (APS) conjugate was prepared in the clean vessel by reacting the fluorescence and a two-fold amount of APS in dehydrated ethanol under an inert argon environment with continuous stirring for more than 17 h. In a clean 50 ml three necked flask, 17 ml of water and 17.4 mg of arginine were mixed with the RITC/APS conjugate and then 1.11 ml of tetraethyl orthosilicate (TEOS) were added slowly beneath the solution surface by a syringe. The reaction proceeded at 70 °C for 24 h²⁴. 30 nm RITC-labeled SNPs were synthesized. 90 nm fluorescein isothiocyanate (FITC) labeled SNPs were synthesized by the further growth of the 30 nm seed particles. In detail, 80 mg arginine, 22.5 ml water, 90 ml ethanol, 1.8 ml 30 nm SNPs dispersion and 0.55 g tetraethyl orthosilicate (TEOS) were added to a clean 250 ml glass reaction vessel. The reaction proceeded at 70°C for 5 h with continuous stirring. Thereafter, 0.55 g more TEOS was added and the reaction proceeded overnight, resulting in 90 nm FITC-labeled SNPs.

In a typical sedimentation-diffusion equilibrium (AUC-SE) experiment, a 3 μ l sample and reference were separately injected into the two channels of an AUC cell of 1.5 mm path length. The AUC cell was then placed into a custom-made^{21, 33} Multi-Wavelength Analytical Ultracentrifuge (MWL-AUC). The measurement settings: Temperature 25 °C; Wavelength range 350 – 700 nm. After a time scale of up to one week, the sedimentation-diffusion equilibrium was reached²⁴.

3.5. References

1. Sanders, J. V.; Murray, M. J., Ordered arrangements of spheres of two different sizes in opal. *Nature* **1978**, *275* (5677), 201-203.
2. Rietz, F.; Stannarius, R., On the brink of jamming: Granular convection in densely filled containers. *Physical Review Letters* **2008**, *100* (7), 078002.
3. Knight, J. B.; Ehrichs, E. E.; Kuperman, V. Y.; Flint, J. K.; Jaeger, H. M.; Nagel, S. R., Experimental study of granular convection. *Physical Review E* **1996**, *54* (5), 5726-5738.
4. Breu, A. P.; Ensner, H.-M.; Kruelle, C. A.; Rehberg, I., Reversing the brazil-nut effect: Competition between percolation and condensation. *Physical Review Letters* **2003**, *90* (1), 014302.
5. Xia, Y.; Nguyen, T. D.; Yang, M.; Lee, B.; Santos, A.; Podsiadlo, P.; Tang, Z.; Glotzer, S. C.; Kotov, N. A., Self-assembly of self-limiting monodisperse supraparticles from polydisperse nanoparticles. *Nature Nanotechnol* **2011**, *6* (9), 580-7.
6. Belli, S.; Patti, A.; Dijkstra, M.; van Roij, R., Polydispersity stabilizes biaxial nematic liquid crystals. *Physical Review Letters* **2011**, *107* (14), 148303.
7. Cabane, B.; Li, J.; Artzner, F.; Botet, R.; Labbez, C.; Bareigts, G.; Sztucki, M.; Goehring, L., Hiding in plain view: Colloidal self-assembly from polydisperse populations. *Physical Review Letters* **2016**, *116* (20), 208001.
8. Bartlett, P.; Ottewill, R. H.; Pusey, P. N., Superlattice formation in binary mixtures of hard-sphere colloids. *Physical Review Letters* **1992**, *68* (25), 3801-3804.

CHAPTER 3

9. Eldridge, M.; Madden, P.; Pusey, P.; Bartlett, P., Binary hard-sphere mixtures: A comparison between computer simulation and experiment. *Molecular Physics* **1995**, *84* (2), 395-420.
10. Shevchenko, E. V.; Talapin, D. V.; Kotov, N. A.; O'Brien, S.; Murray, C. B., Structural diversity in binary nanoparticle superlattices. *Nature* **2006**, *439* (7072), 55-9.
11. Ohara, P. C.; Leff, D. V.; Heath, J. R.; Gelbart, W. M., Crystallization of opals from polydisperse nanoparticles. *Physical Review Letters* **1995**, *75* (19), 3466-3469.
12. Philipse, A. P.; Koenderink, G. H., Sedimentation–diffusion profiles and layered sedimentation of charged colloids at low ionic strength. *Advances in Colloid and Interface Science* **2003**, *100-102*, 613-639.
13. Serrano, C. G.; McDermott, J. J.; Velegol, D., Sediments of soft spheres arranged by effective density. *Nature Materials* **2011**, *10* (9), 716-721.
14. Ruzicka, M., On buoyancy in dispersion. *Chemical Engineering Science* **2006**, *61* (8), 2437-2446.
15. Piazza, R., Settled and unsettled issues in particle settling. *Reports on Progress in Physics* **2014**, *77* (5), 056602.
16. Biesheuvel, P.; Lyklema, J., Sedimentation–diffusion equilibrium of binary mixtures of charged colloids including volume effects. *Journal of Physics: Condensed Matter* **2005**, *17* (41), 6337-6352.
17. Piazza, R.; Buzzaccaro, S.; Secchi, E.; Parola, A., On the general concept of buoyancy in sedimentation and ultracentrifugation. *Physical Biology* **2013**, *10* (4), 045005.
18. Spruijt, E.; Biesheuvel, P. M., Sedimentation dynamics and equilibrium profiles in multicomponent mixtures of colloidal particles. *Journal of Physics: Condensed Matter* **2014**, *26* (7), 075101.
19. Chen, M.; Cölfen, H.; Polarz, S., Centrifugal field-induced colloidal assembly: From chaos to order. *ACS Nano* **2015**, *9* (7), 6944-50.
20. Karabudak, E.; Cölfen, H., The multiwavelength uv/vis detector: New possibilities with an added spectral dimension. In *Analytical ultracentrifugation: Instrumentation, software, and applications*, Uchiyama S., A. F., Stafford W., Laue T., Ed. Springer, Tokyo: 2016.
21. Pearson, J.; Walter, J.; Peukert, W.; Cölfen, H., Advanced multiwavelength detection in analytical ultracentrifugation. *Analytical chemistry* **2018**, *90* (2), 1280-1291.
22. Walter, J.; Löhr, K.; Karabudak, E.; Reis, W.; Mikhael, J.; Peukert, W.; Wohlleben, W.; Cölfen, H., Multidimensional analysis of nanoparticles with highly disperse properties using multiwavelength analytical ultracentrifugation. *ACS Nano* **2014**, *8* (9), 8871-8886.
23. Zhao, H.; Brautigam, C. A.; Ghirlando, R.; Schuck, P., Overview of current methods in sedimentation velocity and sedimentation equilibrium analytical ultracentrifugation. *Current Protocols in Protein Science* **2013**, *20.12*. 1-20.12. 49.
24. Xu, X.; Franke, T.; Schilling, K.; Sommerdijk, N.; Cölfen, H., Binary colloidal nanoparticle concentration gradients in a centrifugal field at high concentration. *Nano Letters* **2019**, *19* (2), 1136-1142.
25. Planken, K. L.; Cölfen, H., Analytical ultracentrifugation of colloids. *Nanoscale* **2010**, *2* (10), 1849-1869.
26. Lamm, O., Zur theorie und methodik der ultrazentrifugierung. *Zeitschrift für Physikalische Chemie* **1929**, *143* (1), 177-190.

Binary hard spheres with a large size ratio in a centrifugal field

27. Cole, J. L.; Correia, J. J.; Stafford, W. F., The use of analytical sedimentation velocity to extract thermodynamic linkage. *Biophysical Chemistry* **2011**, *159* (1), 120-128.
28. Rasa, M.; Ern , B.; Zoetekouw, B.; van Roij, R.; Philipse, A., Macroscopic electric field and osmotic pressure in ultracentrifugal sedimentation–diffusion equilibria of charged colloids. *Journal of Physics: Condensed Matter* **2005**, *17* (15), 2293-2314.
29. C lfen, H., Analytical ultracentrifugation of colloids. In *Analytical ultracentrifugation: Techniques and methods*, SCOTT, D. J., ed. and others, Ed. Cambridge: Royal Society of Chemistry: UK, 2005; Vol. 23, pp 501-583.
30. Piazza, R.; Buzzaccaro, S.; Secchi, E.; Parola, A., What buoyancy really is. A generalized archimedes' principle for sedimentation and ultracentrifugation. *Soft Matter* **2012**, *8* (27), 7112-7115.
31. Leung, W. W.-F., *Industrial centrifugation technology*. McGraw-Hill New York: 1998.
32. Julien, P. Y., *Erosion and sedimentation*. Cambridge University Press: 2010.
33. Pearson, J.; Hofstetter, M.; Dekorsy, T.; Totzeck, M.; C lfen, H., Design concepts in absorbance optical systems for analytical ultracentrifugation. *Analyst* **2018**, *143* (17), 4040-4050.

3.6. Appendix

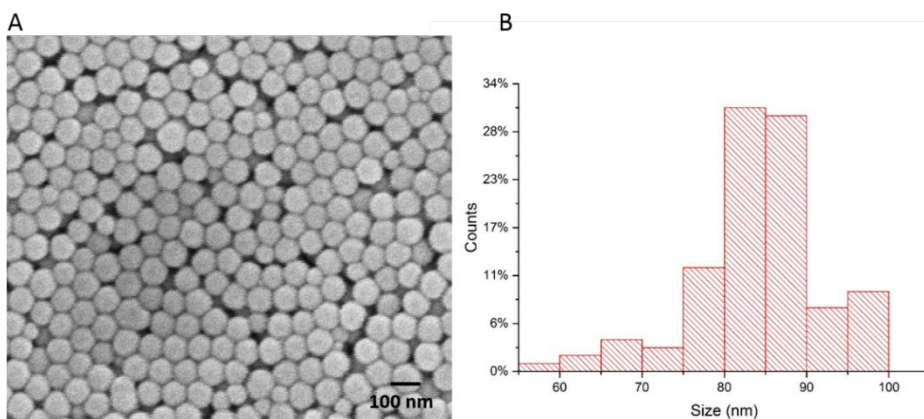


Figure S1: A scanning electron microscopy (SEM) image of the synthesized 90 nm SNPs (A) and the size distribution by counting more than 100 particle diameters using a home-made Matlab script (B). The mean particle size was 84.0 nm (± 7.7 nm where \pm indicates the size standard deviation).

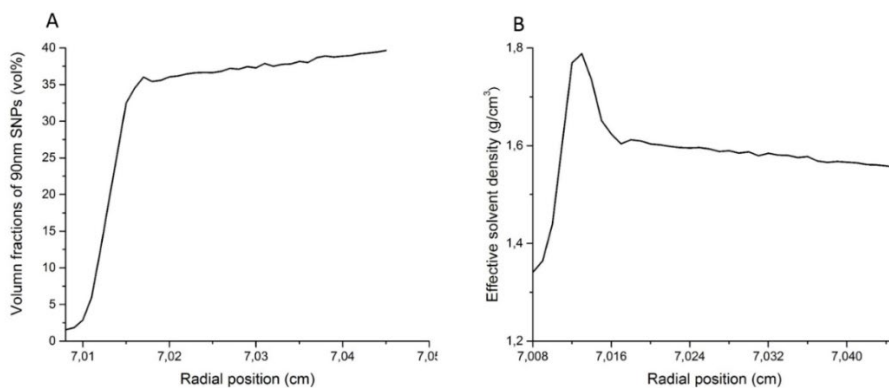


Figure S2: Experimental volume fraction gradient of 90 nm SNPs in the binary suspension of 30 nm (1 vol%) and 90 nm (9 vol%) SNPs in an AUC at 2800 rpm, 25 °C (A); The calculated effective solvent density using Equation (a) (B).

Binary hard spheres with a large size ratio in a centrifugal field

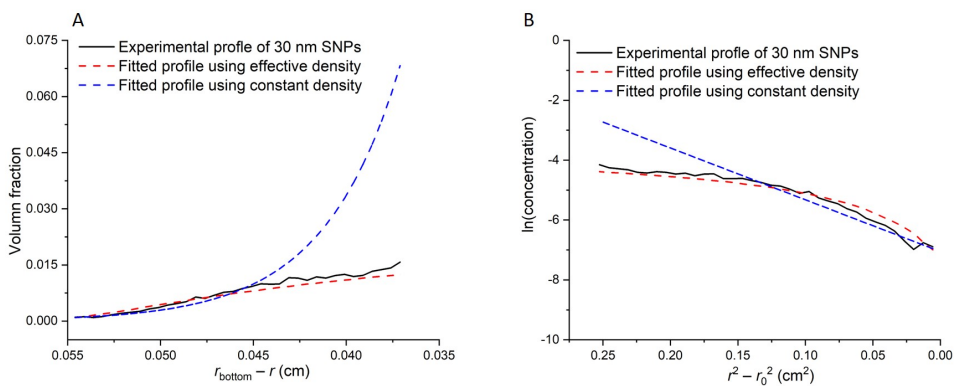
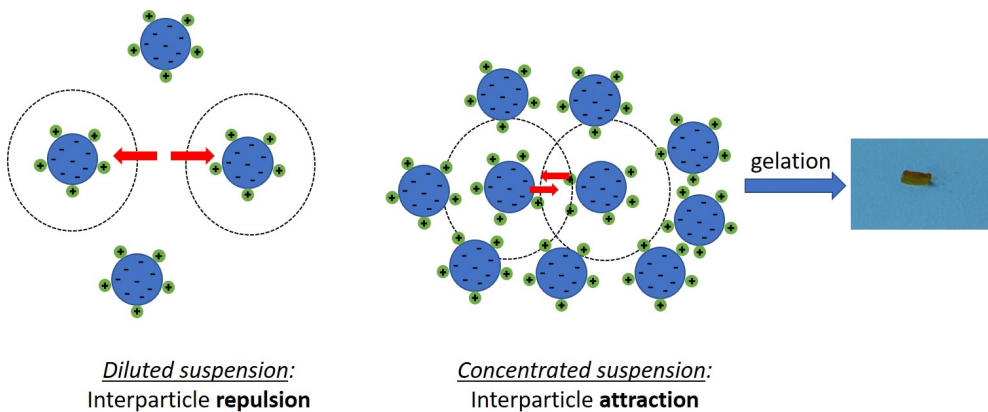


Figure S3: Experimental concentration profile (black line) for 30 nm SNPs in the binary suspension of 30 nm (1 vol%) and 90 nm (3 vol%) SNPs in an AUC at 1100 rpm, 25 °C. The fitted profiles for 30 nm SNPs using the constant solvent density (blue line) and the effective density (red line). A was plotted as volume fraction as a function of $r_{\text{bottom}} - r$ and B was plotted as $\ln(\text{concentration})$ as a function of $r^2 - r_0^2$ where $r_{\text{bottom}} - r$ is the distance from the cell bottom, r_0 is the meniscus radial position.

CHAPTER 4

Self-Association and Gelation of Like-Charged Colloids at Very High Concentration



The results described in this chapter are based on:

Xufeng Xu, Gijsbertus de With* and Helmut Cölfen*. Self-association and gelation of like-charged colloids at very high concentration. *Science Advances* 2020, in revision.

4. Self-association and gelation of like-charged colloids at very high concentration

Colloid-colloid interactions in a crowded environment are complicated and only a limited number of experimental and theoretical studies has been conducted for highly concentrated conditions where super-crowding and strong non-ideality play vital roles. Here we report quantitative molecular, microscopic and macroscopic experimental results on like-charged colloids in a concentration gradient up to 60 vol% by conducting sedimentation-diffusion equilibrium experiments in an analytical ultracentrifuge. The concentration gradient conceals important information, including size, surface charge and interparticle interaction. We surprisingly observe a steep pH gradient resulting from a Donnan equilibrium and self-association of like-charged colloids at high concentration, inducing gel formation, which is very different from particle repulsion at diluted conditions. These results are a main step forward in the study of crowding effects on matter-matter interaction.

4.1. Introduction

Sedimentation of colloids is of great importance in practice¹⁻³. Colloids sediment until a sedimentation-diffusion equilibrium state is reached and from the equilibrium concentration profile important thermodynamic information of colloids⁴ can be retrieved. The classic example is provided by Jean Baptiste Perrin who determined the Boltzmann constant by measuring the sedimentation-diffusion profile of a suspension containing microscopic gamboge particles of a uniform size under natural gravity⁵. Systematic studies on the sedimentation of colloids began with the easiest case, namely nearly hard spheres⁶⁻⁷, where only volume exclusion repulsion plays a role, and confocal laser scanning microscopy was applied to study *in-situ* the sedimentation process thoroughly⁸. The more practical but also more complicated case of charged colloids was also studied theoretically by the inclusion of the Donnan equilibrium⁹⁻¹¹, followed by analytical ultracentrifugation (AUC) experiments on charged nanoparticles at a low concentration¹². In this way, a macroscopic electric field^{4, 12} was shown to exist, which stems from the huge mass difference between the colloidal particles and the counter-ions⁹. The sedimentation-diffusion (SD) concentration profiles can be described by **Equation 4.1**. Depending on the magnitude of the non-dimensional number density y and surface charge Z of the colloids, three parts, namely a low ($y \ll Z^{-1}$), medium ($Z^{-1} \ll y \ll 1$) and high ($y \gg 1$) concentration regime can be distinguished in one SD profile:

$$P^* = y + Z(\sqrt{1 + y^2} - 1) = \begin{cases} y, & y \ll Z^{-1} \\ Zy^2/2, & Z^{-1} \ll y \ll 1 \\ (Z + 1)y, & y \gg 1 \end{cases} \quad (4.1)$$

In **Equation (4.1)**, $P^* = \frac{PZ}{2c_s kT}$ is the non-dimensional osmotic pressure, $y = \frac{Z\rho}{2c_s}$ is the non-dimensional number density of colloids, Z is the colloidal surface charge, $2c_s$ is the total ion concentration, kT is the thermal energy and ρ is the number density of colloids⁹. **Equation**

4.1 describes the SD profile of charged colloids well under the assumption that there is no interparticle interaction, that is, for diluted suspensions (up to 0.48 vol% for silica nanoparticles of diameter 60 nm¹²). However, the sedimentation of charged colloids at high concentration with a much broader practical consequence still lacks careful studies due to the experimental difficulties of significant light scattering hindering the detection of nanoparticle concentrations and complicated interparticle interactions¹³⁻¹⁴ in this crowded environment¹⁵. Here we report the SD profile of concentrated charged colloids with a concentration gradient up to as high as 60 vol% - close to the densest possible packing of spheres. We found that the SD concentration profile quantitatively unfolded the self-association among colloidal particles of the same charge when the colloidal dispersion reached an extremely high concentration. This resulted in the formation of a stable gel. A theoretical model was also raised for the origin of this unknown attractive force. As far as we are aware, this is the first time that the interparticle interaction can be quantitatively measured at such high concentration, thus revealing an unexpected attractive force.

4.2. Results and discussion

4.2.1. Sedimentation-diffusion equilibrium of negatively charged silica nanoparticles at high concentration

Silica nanoparticles (SNPs) were chosen as a model colloid because they have a relatively low refractive index ($n \approx 1.46$) and can be synthesized by well-established methods.¹⁶⁻¹⁸ To be able to evaluate the results at high concentration of SNPs, the colloids were first covalently-labeled with fluorescent molecules, such as fluorescein isothiocyanate (FITC) and rhodamine B isothiocyanate (RITC)¹⁹⁻²⁰, and thereafter dispersed in a refractive-index matching solvent (an 80 vol% glycerol and 20 vol% water mixture). The physical properties of this dispersion are listed in **Table 4.1**. The particle size was measured by scanning electron microscopy (SEM), as shown in Figure S1b and the surface charge number was measured by an electrophoretic experiment (See Methods section). The sedimentation velocity (AUC-SV) experiment was also used to in-situ characterize the colloidal composition in the dispersion. In Figure S1a, the dispersion is shown to consist of monomers and various kinds of oligomers (the term ‘oligomers’ are used as a jargon analogous to its use in polymer science), which were introduced in a reproducible way by the synthesis protocol described in Materials and Methods section (detailed analysis of oligomer peaks shown in S11). The presence of oligomers induced an environment of super-crowding, which for a monodisperse dispersion is hardly reached (as shown in Figure S2). dispersion (by a different synthesis protocol described in SI2) is hardly reached (as shown in Figure S2). Without any oligomer, the highest volume fraction only reached ca. 40 vol% while with the presence of oligomers, the particle can reach 60 vol%. Therefore, interparticle distance became smaller and this high density was labeled as an environment of super-crowding. For concentrated charged colloids during sedimentation, the interparticle interaction needs to be considered, which is taken into account by employing the second virial coefficient (B_2).²¹⁻²² Correspondingly, **Equations 4.2 – 4.4** are obtained by modifying **Equation 4.1** to be able to apply the analysis of charged colloids at a considerably higher concentration:

CHAPTER 4

$$\text{Region I:} \quad c(r) = c(r_1) \exp\left(\frac{r^2 - r_1^2}{2L_\omega^2}\right) \quad (4.2)$$

$$\text{Region II:} \quad c(r) = c(r_2) + \frac{r^2 - r_2^2}{zL_\omega^2/c_s} \quad (4.3)$$

$$\text{Region III:} \quad c(r) = c(r_3) \exp\left(\frac{\omega^2(1-v\rho)}{2RT} M_{\text{app}}(r^2 - r_3^2) - B_2 M(c(r) - c(r_3))\right) + E \quad (4.4)$$

In **Equations 4.2 – 4.4**, $c(r)$ is the mass density of colloids, $L_\omega = \sqrt{\frac{kT}{V(\rho_p - \rho_s)\omega^2}}$ is the so-called centrifugal length with ρ_p the colloidal particle density, ρ_s the solvent density, V the volume of one particle and ω the angular velocity of the rotor. Further, $M_{\text{app}} = M/(Z + 1)$ is the apparent molar mass with the real molecular mass M and the colloidal surface charge Z . The parameters r_1 , r_2 and r_3 are radial reference points, B_2 is the second virial coefficient and E is the baseline offset. As shown in **Figure 4.1**, a typical SD profile of SNPs at an initial concentration of 15 vol% contains three regions (the SD profiles of a different concentration and a different batch are shown in **Figure S3** which both share the same three-region feature). In *Region I*, at low concentration, the concentration profile follows the typical exponential barometric increase, which was fitted with **Equation 4.2**. From the fitted L_ω value the nanoparticle size was calculated, as shown in **Table 4.2**. The fitted particle size 81 nm agrees perfectly with the size of 84 nm as measured by SEM (**Table 4.1**), the relative deviation being 3.6 %. In *Region II*, at somewhat higher concentration, a quadratic profile appears which was fitted by **Equation 4.3**. The particle surface charge number Z was calculated from the fit, as shown in **Table 4.2**. The fitted value $Z = 54$ is consistent with the value of $Z = 49$ as measured by a reference electrophoresis experiment (the value for Z is shown in **Table 4.1**). In *Region III*, at even higher concentration, the barometric exponential was extended with a B_2 term. The fitted value for B_2 turned out to be negative, meaning that the net interparticle interaction is attractive at this high concentration for particles having the same charge (the inclusion of a higher order virial coefficient discussed in SI3). No attraction but only a plateau profile was found in *Region III* in case only monomers are present, as shown in **Figure S2b**. The sedimentation profiles at various angular velocities, from which the true molecular mass M can be estimated, are illustrated and discussed in **SI 4**. The self-association of colloids in this crowded environment is also indicated by the formation of a phase boundary, as shown in **Figure 4.2a**.

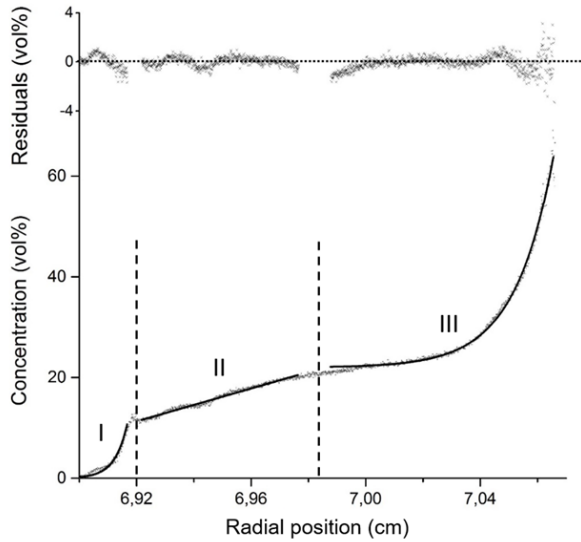


Figure 4.1: A typical experimental sedimentation-diffusion equilibrium concentration profile (dotted line), corresponding fitting profiles (solid line) and the residual difference (dotted line) for a SNP dispersion at an initial concentration of 15 vol%, at 1100 rpm. Three regions marked as I, II and III are divided by dashed lines.

d (nm)	σ	ρ (g·cm ⁻³)	Z
84	0.09	1.6 ± 0.2	49

Table 4.1: The physical properties of fluorescent labeled silica nanoparticles dispersed in an 80 vol% glycerol and 20 vol% water mixture. The parameters d and σ are the diameter and size polydispersity from scanning electron microscopy (SEM) while ρ is the density taken from the literature (15) and Z is the surface charge number, estimated from the electrophoretic mobility.

Volume fraction (vol%)	$d_{\text{Region I}}$ (nm)	$Z_{\text{Region II}}$	$B_2_{\text{Region III}}$ (mol·(kg·vol%) ⁻¹)
15	81	54	-7.8·10 ⁻⁸

Table 4.2: Fitting results from the analysis of the sedimentation-diffusion equilibrium concentration profile of **Figure 1**.

4.2.2. Molecular and macroscopic views into the interparticle attraction

A dramatic pH gradient from pH 7 to pH 13 (detailed measurement and calibration procedure is described in **SI 6**) was established due to a pronounced Donnan potential at high concentration, as shown **Figure 4.3a**. It can be proven since the electric field generated by Donnan potential has almost the same strength as that calculated from pH gradient. The electric field in *region III* can be estimated from the Donnan potential by using the equation²³:

$E = -m\omega^2 r / (1 + Z)e$, where m is the particle molecular mass (3×10^5 kg/mol), ω is the angular velocity (523 rad/s), r is the radial position in *region III* (7 cm) and Z is the particle surface charge number in *region III* (49). The electric field E can be thus calculated as ca. 10 V/cm. The electric field in *region III* can be also estimated by the pH jump. The pH value close to the sediment was ca. 13, while in the meniscus part the pH was about 7. Therefore, the ion concentration jump is 10^6 . The electric field can be calculated using the Nernst equation $E = \frac{kT}{e} \ln \frac{c}{c_0}$, where c is the concentration of ions close to the sediment and c_0 is the initial ion concentration near the meniscus. This leads to $E \cong 7$ V/cm (with as distance from the meniscus to *region III* ca. 0.06 cm). These two values agree reasonably well in terms of the order of magnitude. Therefore, such a steep pH gradient can be a result from the Donnan effect.

Furthermore, the presence of approximately 4.4 hydroxide groups per nm^2 on the silica nanoparticle surface was estimated using the data for *region III*, and this value agrees with the literature value²⁴ (detailed calculation is described in **SI 7**). At the end of *region III*, the pH value decreases from pH 13 to pH 12, which means that the amount of available deprotonated hydroxide groups on the surface decreases at this extremely high concentration at the very bottom of the sediment. This agrees well with the counter-ion bridge hypothesis: As nanoparticles get very close, a small amount of surface counter ions (protons) between the deprotonated surface hydroxide groups on both particles leads to their protonation and this decreases the amount of deprotonated hydroxide groups. The presence of attractive interaction was further verified by the observation that a stable self-standing gel was created (as shown in **Figure 4.3b**, more images shown in **Figure S12**), which de-swelled upon increase of the centrifugal field, as is expected for gels²⁵ (as shown in **Figure S6a**). In the gel, the silica nanoparticles are arranged in a glassy close packing (**Figure S13**). The gel stability was monitored in the refractive index matching solvent and it was found that the gel stayed intact, and the mass hardly changed even after 3 days (**Figure S14** and the detailed experiment described in **SI 8**). The reversibility of the gel was examined at different angular velocities in the AUC, as shown in **Figure 4.3c** and **Figure 4.3d**. When the angular velocity was decreased from 40000 rpm to 1100 rpm, the gel structure became irreversible with a hardly changed B_2 value as compared to the value at 40000 rpm. When the angular velocity was decreased from 5000 rpm to 1100 rpm, the fitted B_2 value was decreased by a factor of 100 to the value as initially obtained at 1100 rpm. This indicates that the structural change in the gel is still reversible when the angular velocity remains below 5000 rpm. The gel was also studied after the addition of 1 M NaCl solution and the typical gel shrinkage with solvent expulsion was observed as a result of additional counter-ion bonding, as shown in **Figure S15**. This leads to a stronger gel.

4.2.3. Theoretical discussion on interparticle attraction

There are several theories proposed for like-charge attraction, including counter-ion condensation theory²⁶, confinement induced attraction theory²⁷⁻²⁸ and volume theory²⁹. In the counter-ion condensation theory, Manning considered the contribution from non-electrostatic components, which originate from both condensed and uncondensed counterions, besides the normal electrostatic attraction²⁶. In the confinement induced attraction

theory, Grier claimed that charged walls somehow modified the interaction of charged colloids, making it inconsistent with mean-field theory³⁰. Van Roij proposed that a density dependent volume term should be included in the interaction in addition to the normal two-body term³¹, a proposition known as volume theory. We consider here that the net attractive force may be related to the presence of counter ions between charged colloids³²⁻³³. Bridging counter ions between like-charge colloids can lead to attraction, as indicated in **Figure 4.2b**. Moreover, this interparticle attractive force (in *Region III*) appears to have a long range up to ca. 30 nm, as judged from the knee in the sedimentation concentration profile at the radial position of ca. 7.07 cm (see **Figure S4**). In **Figure 4.2c**, a qualitative picture of the total interparticle potential is given. For the potential only the Keesom-Debye part (zero frequency part, $\nu = 0$) is considered, because the (frequency-dependent dispersion part, $\nu > 0$) is assumed to be negligible due to refractive index matching³⁴. At a short range there is the electrostatic repulsion³⁵. From the fact that a gel made at a low angular velocity is reversible (**Figure 4.3c**) and at a high velocity is irreversible (**Figure 4.3d**), we conclude that, when particles approach each other, a relatively low secondary barrier must be present in the potential energy landscape, followed by a secondary minimum (the reversible gel state). After passing the primary barrier, the primary minimum (the irreversible gel state) is reached, as shown in **Figure 4.2c**. The secondary barrier is felt when the interparticle distance decreases below ~ 30 nm (corresponding to ca. 30 vol%, the starting concentration of region III) and approximately equal to the screening length. A counter-ion bridge attraction is likely responsible for the secondary minimum. An estimate of the values involved can be made. To that purpose we distinguish between the forward barrier (approaching particles from “infinity”) and the return barrier (separating particles from the secondary minimum). As the dispersion does not form a gel spontaneously, the forward barrier must at least a few kT , say $2kT$ to $4kT$. An estimate based the angular velocity yields a similar value. The reversible gel, formed at a low angular velocity, reptizes again within about 8 h, suggesting a return barrier of about $4kT$ to $6kT$. The irreversible gel, formed at a high angular velocity, is stable for at least 8 days, suggesting a (primary return) barrier height of at least about $25kT$. Conditions for reptization have been discussed by Frens and Overbeek³⁶ and Poovarodom and Berg³⁷. Ion bridging has been discussed by Liu et al.³⁸. The chemical potential was further calculated to illustrate the driving force for gel formation (detailed calculation is given in **SI 5**) and **Figure S8** shows that the decrease in chemical potential with the particle concentration increase drove the gel formation at high concentration. As other mechanisms can also lead to gel formation, the various options were discussed in **SI 9**.

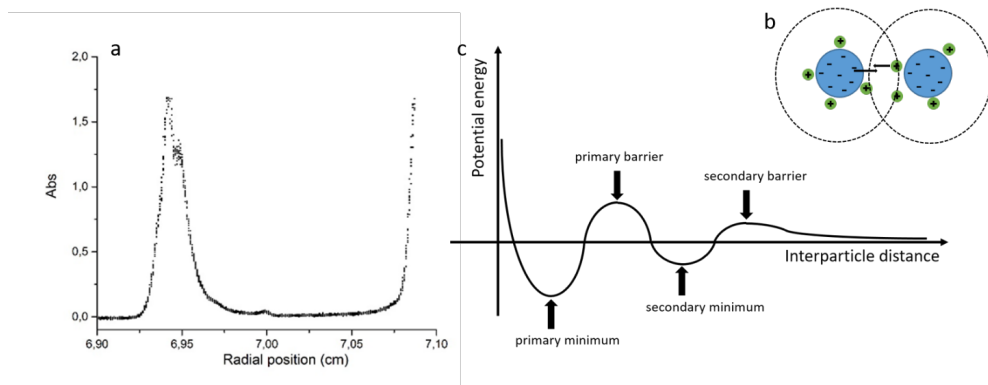


Figure 4.2: a. A typical absorbance profile showing the presence of a phase boundary at ca. 6.94 cm, at an arbitrary wavelength (700 nm) after the sedimentation-diffusion equilibrium was reached for SNPs of an initial concentration of 15 vol% at 1100 rpm. Such a phase boundary is also observed using other wavelengths; b. Schematic picture of the counter-ion bridge force. The negatively charged particles are indicated by the two spheres with the sign '-'. The double layer region is indicated by the ring around the particles. The positively charged counter-ions are indicated as black spheres with the sign '+' and the counter-ion bridge attraction between the two particles is indicated by the arrows; c. A schematic picture of the potential energy as a function of interparticle distance.

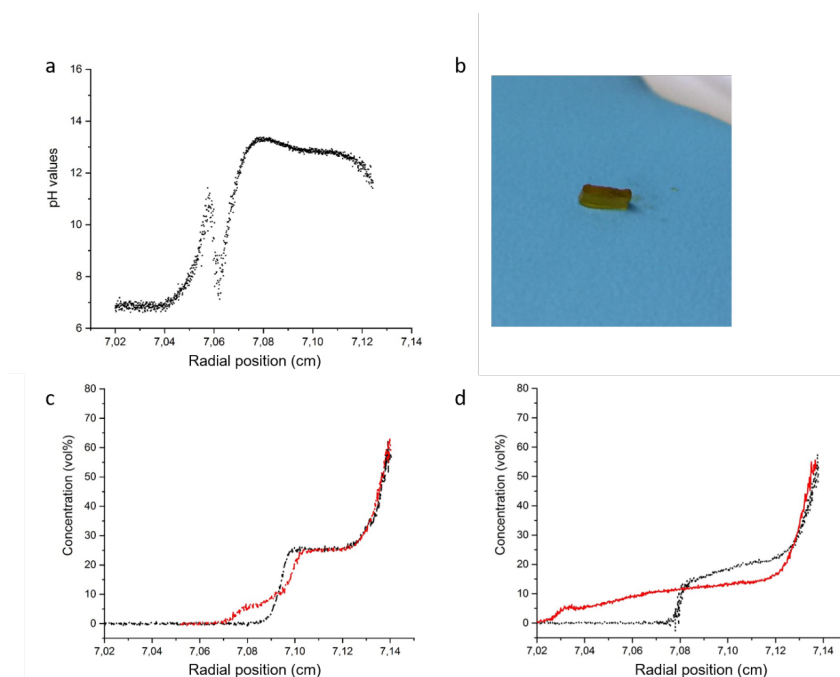


Figure 4.3: a. pH gradient along the radius, characterized by a pH indicator at the sedimentation-diffusion equilibrium for SNPs of an initial concentration of 15 vol% at 5000

Self-association and gelation of like-charged colloids at very high concentration

rpm. A phase boundary is located at about 7.06 cm and therefore an artificial bump appears; b. A typical picture of a stable self-standing gel (yellowish color from the fluorescence) after the sedimentation-diffusion equilibrium for SNPs of an initial concentration of 15 vol% at 40000 rpm. c. Experimental sedimentation-diffusion equilibrium concentration profile for SNPs of an initial concentration of 15 vol% at 40000 rpm (black) and at 1100 rpm (red) after having been subjected to 40000 rpm; d. Experimental sedimentation-diffusion equilibrium profile for SNPs of an initial concentration of 15 vol% at 5000 rpm (black) and at 1100 rpm (red) after having been subjected to 5000 rpm.

4.3. Conclusion

In summary, we have experimentally demonstrated that very concentrated charged colloids can be studied by sedimentation-diffusion equilibria in the AUC up to extremely high concentrations of 60 vol%. The obtained three-region concentration profile can be fitted by appropriate equations with the inclusion of charge effects and interparticle interactions for colloids. The colloidal particle size can be obtained in *Region I*, matching well with an independent SEM estimate, while for *Region II* the fitted colloidal surface charge agrees well with the electrophoresis experiments. Most surprisingly, the net interparticle interaction obtained in the highly crowded region (*Region III*) turned out to be attractive, which probably stems from counter-ion bridging forces. At this high concentration, a dramatic pH increase results from Donnan equilibrium and a slight pH decrease at very high concentration at the bottom of the sediment may be explained by counter-ion bridges. The gel formed at this high concentration is stable in the supernatant solvent and may be further strengthened with external salt. The research described in this paper thus provides deeper insight into the behavior of colloids in an extremely crowded environment, as relevant for many fields in science and technology.

4.4. References

1. Vanoni, V. A. In *Sedimentation engineering*, American Society of Civil Engineers: 2006.
2. Kynch, G. J., A theory of sedimentation. *Transactions of the Faraday society* **1952**, *48*, 166-176.
3. Julien, P. Y., *Erosion and sedimentation*. Cambridge University Press: 2010.
4. Rasa, M.; Ern , B.; Zoetekouw, B.; van Roij, R.; Philipse, A., Macroscopic electric field and osmotic pressure in ultracentrifugal sedimentation–diffusion equilibria of charged colloids. *Journal of Physics: Condensed Matter* **2005**, *17* (15), 2293-2314.
5. Perrin, J., *Atoms*. Van Norstrand Company: New York, 1913.
6. Pusey, P. N.; van Megen, W., Phase behaviour of concentrated suspensions of nearly hard colloidal spheres. *Nature* **1986**, *320* (6060), 340-342.
7. Davis, K. E.; Russel, W. B.; Glantschnig, W. J., Disorder-to-order transition in settling suspensions of colloidal silica: X-ray measurements. *Science* **1989**, *245* (4917), 507-510.
8. Van Blaaderen, A.; Ruel, R.; Wiltzius, P., Template-directed colloidal crystallization. *Nature* **1997**, *385*, 321.

CHAPTER 4

9. Van Roij, R., Defying gravity with entropy and electrostatics: Sedimentation of charged colloids. *Journal of Physics: Condensed Matter* **2003**, *15* (48), S3569-S3580.
10. Overbeek, J. T., The donnan equilibrium. *Prog. Biophys. Biophys. Chem* **1956**, *6* (1), 57-84.
11. Donnan, F. G., Theorie der membrangleichgewichte und membranpotentiale bei vorhandensein von nicht dialysierenden elektrolyten. Ein beitrag zur physikalisch - chemischen physiologie. *Zeitschrift für Elektrochemie und angewandte physikalische Chemie* **1911**, *17* (14), 572-581.
12. Raşa, M.; Philipse, A. P., Evidence for a macroscopic electric field in the sedimentation profiles of charged colloids. *Nature* **2004**, *429*, 857.
13. Lyklema, J., *Fundamentals of interface and colloid science: Soft colloids*. Elsevier: 2005; Vol. 4.
14. Wills, P. R.; Scott, D. J.; Winzor, D. J., Thermodynamics and thermodynamic nonideality. In *Encyclopedia of biophysics*, Roberts, G. C. K., Ed. Springer Berlin Heidelberg: Berlin, Heidelberg, 2013; pp 2583-2589.
15. Xu, X.; Franke, T.; Schilling, K.; Sommerdijk, N. A. J. M.; Cölfen, H., Binary colloidal nanoparticle concentration gradients in a centrifugal field at high concentration. *Nano Letters* **2019**, *19* (2), 1136-1142.
16. Verhaegh, N. A.; van Blaaderen, A., Dispersions of rhodamine-labeled silica spheres: Synthesis, characterization, and fluorescence confocal scanning laser microscopy. *Langmuir* **1994**, *10* (5), 1427-1438.
17. Stöber, W.; Fink, A.; Bohn, E., Controlled growth of monodisperse silica spheres in the micron size range. *Journal of Colloid and Interface Science* **1968**, *26* (1), 62-69.
18. Yokoi, T.; Sakamoto, Y.; Terasaki, O.; Kubota, Y.; Okubo, T.; Tatsumi, T., Periodic arrangement of silica nanospheres assisted by amino acids. *Journal of the American Chemical Society* **2006**, *128* (42), 13664-13665.
19. Van Blaaderen, A.; Vrij, A., Synthesis and characterization of colloidal dispersions of fluorescent, monodisperse silica spheres. *Langmuir* **1992**, *8* (12), 2921-2931.
20. Ow, H.; Larson, D. R.; Srivastava, M.; Baird, B. A.; Webb, W. W.; Wiesner, U., Bright and stable core-shell fluorescent silica nanoparticles. *Nano Letters* **2005**, *5* (1), 113-117.
21. Haschemeyer, R. H.; Bowers, W. F., Exponential analysis of concentration or concentration difference data for discrete molecular weight distributions in sedimentation equilibrium. *Biochemistry* **1970**, *9* (2), 435-445.
22. McRorie, D. K.; Voelker, P. J., *Self-associating systems in the analytical ultracentrifuge*. Beckman Instruments Fullerton, CA: 1993.
23. Philipse, A. P., Remarks on the donnan condenser in the sedimentation-diffusion equilibrium of charged colloids. *Journal of Physics: Condensed Matter* **2004**, *16* (38), S4051-S4062.
24. Zhuravlev, L., Concentration of hydroxyl groups on the surface of amorphous silicas. *Langmuir* **1987**, *3* (3), 316-318.
25. Cölfen, H., Analytical ultracentrifugation of gels. *Colloid and Polymer Science* **1995**, *273* (12), 1101-1137.
26. Manning, G. S., Counterion condensation theory of attraction between like charges in the absence of multivalent counterions. *The European Physical Journal E* **2011**, *34* (12), 132.

Self-association and gelation of like-charged colloids at very high concentration

27. Grier, D. G., When like charges attract: Interactions and dynamics in charge-stabilized colloidal suspensions. *Journal of Physics: Condensed Matter* **2000**, *12* (8A), A85-A94.
28. Larsen, A. E.; Grier, D. G., Like-charge attractions in metastable colloidal crystallites. *Nature* **1997**, *385* (6613), 230-233.
29. Van Roij, R.; Dijkstra, M.; Hansen, J.-P., Phase diagram of charge-stabilized colloidal suspensions: Van der waals instability without attractive forces. *Physical Review E* **1999**, *59* (2), 2010-2025.
30. Han, Y.; Grier, D. G., Confinement-induced colloidal attractions in equilibrium. *Physical Review Letters* **2003**, *91* (3), 038302.
31. Van Roij, R., Attraction or repulsion between charged colloids? A connection with debye-hückel theory. *Journal of Physics: Condensed Matter* **2000**, *12* (8A), A263-A267.
32. Van Rijssel, J.; Peters, V. F.; Meeldijk, J. D.; Kortschot, R. J.; van Dijk-Moes, R. J.; Petukhov, A. V.; Erne, B. H.; Philipse, A. P., Size-dependent second virial coefficients of quantum dots from quantitative cryogenic electron microscopy. *Journal of Physical Chemistry B* **2014**, *118* (37), 11000-5.
33. Hill, T. L., *An introduction to statistical thermodynamics*. Courier Corporation: 1986.
34. Israelachvili, J. N., *Intermolecular and surface forces*. Academic press: 2015.
35. I. Hogg, R.; W. Healy, T.; W. Fuerstenau, D., *Mutual coagulation of colloid dispersions*. 1966; Vol. 62.
36. Frens, G.; Overbeek, J. T. G., Repeptization and the theory of electrostatic colloids. *Journal of Colloid and Interface Science* **1972**, *38* (2), 376-387.
37. Poovarodom, S.; Berg, J. C., Spontaneous repeptization of colloidal dispersions. *Colloids and Surfaces A: Physicochemical and Engineering Aspects* **2009**, *342* (1-3), 16-23.
38. Liu, X.; Feilberg, K. L.; Yan, W.; Stenby, E. H.; Thormann, E., Electrical double-layer and ion bridging forces between symmetric and asymmetric charged surfaces in the presence of mono- and divalent ions. *Langmuir* **2017**, *33* (18), 4426-4434.

4.5. Appendix

4.5.1. Materials and methods

Synthesis of fluorescein/rhodamine labeled silica nanoparticles

Fluorescein/rhodamine labeled silica nanoparticles (diameter = 84 nm, PDI = 0.09) were regrown from 30 nm fluorescent labeled silica core particles¹. 80 mg arginine, 22.5 ml water, 90 ml ethanol, 1.8 ml core dispersion and 0.55 g tetraethyl orthosilicate (TEOS) were added to a clean 250 ml glass reaction vessel. The reaction was carried out at 70 °C with stirring for 5 h. Thereafter, 0.55 g TEOS was added and the reaction was continued overnight. The size of the synthesized silica nanoparticles was characterized by scanning electron microscopy (SEM), dynamic light scattering (DLS) and AUC. The synthesized nanoparticles were purified by dialysis or repeated centrifugation until a constant conductivity was reached.

Analytical ultracentrifugation set-up

In a typical sedimentation-diffusion equilibrium (AUC-SE) experiment, a home-made multi-wavelength analytical ultracentrifuge²⁻³ (MWL-AUC) with AUC titanium double sector cells of 1.5 mm pathlength (Nanolytics GmbH, Potsdam, Germany) was used. The settings for the home-made MWL-AUC are: Temperature 25 °C; Wavelength range: 250 – 700 nm (spectrometer resolutions 1 nm); Radial step: 1 or 2 μm; Scan interval: 3600 s. Typically, sedimentation-diffusion equilibrium was reached after 7 days. Equilibrium was checked by an unchanged concentration gradient for 10 h.

Electrophoretic experiment

The ion concentration for the silica dispersion was estimated from the electrical conductivity, as measured by a conductivity meter (Schott Instruments, Lab 960). The zeta potential was measured by a Malvern Zetasizer Nano ZSP. The conversion from electrophoretic mobility to zeta potential was achieved by using Henry Equation. The smoluchowski approximation was used because it is suitable for samples suspended in aqueous solutions. The colloidal concentration used was very diluted. The solvent composition used was 65 vol% glycerol + 35 vol% water. When the volume fraction of glycerol increased above 65%, the signal became extremely weak due to nearly refractive index matching. The surface charge number Z was finally estimated using the Debye-Hückel approximation⁴: $ze = 4\pi\epsilon_0\epsilon_r|\xi|R(1 + R\kappa)$ where ϵ_0 and ϵ_r are the electric permittivity of vacuum and the relative permittivity of the solvent, respectively, ξ is the surface potential, R is the particle radius and κ^{-1} is the Debye length.

4.5.2. Supplementary text

SI 1: The analysis of oligomer peaks from sedimentation velocity (AUC-SV) experiment

The sedimentation coefficients s of oligomers can be calculated from the s value of monomers by using the translational diffusion coefficient D_t ratio of oligomers over monomers in the literature⁵ (Table S1) and applying Equation S1.

Self-association and gelation of like-charged colloids at very high concentration

$$\frac{s}{D_t} = \frac{M(1-\bar{v}\rho_s)}{RT} \quad (S1)$$

with M the particle molecular mass, \bar{v} the partial specific volume of particles and ρ_s the solvent density. With the molecular mass ratios of oligomers and monomers known, the specific volume of the particles and the solvent density are fixed, and the sedimentation coefficients s of oligomers can be calculated from the s value of the monomer using the normalized translational diffusion coefficient D_t . **Table S1** was given as an example for the clusters of 2 and 3 particles.. The calculation results and a comparison with the experimental data are shown in **Table S2**. An excellent agreement is obtained, and all the peaks can be recognized in **Figure S1a**. Larger clusters with more complicated configurations are also present in the suspension.

Oligomer	Monomer	Dimer	Trimer triangle	Trimer linear	Large cluster
Normalized D_t	1	0.75	0.66	0.60	...

Table S1: Normalized translational diffusion coefficients D_t of different oligomers, such as dimers and trimers from the literature⁵.

Oligomers	Monomer	Dimer	Trimer (triangle)	Trimer (linear)
s_{theo} (S)	53	79	105	95
s_{exp} (S)	53	78	105	93
Deviation (%)	0	1	0	2

Table S2: Theoretical and experimental sedimentation coefficients of different oligomers, such as dimers and trimers

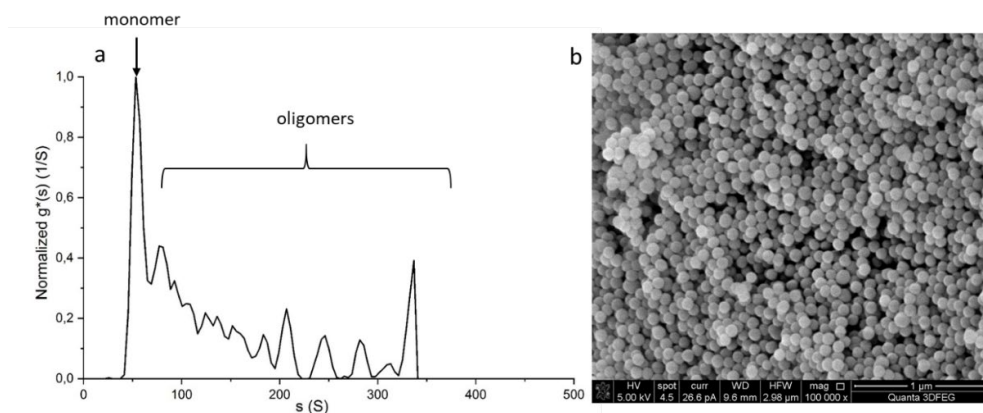


Figure S1: a) Distribution of the sedimentation coefficient s of SNPs in dispersion, measured by an AUC sedimentation velocity (AUC-SV) experiment using the $g^*(s)$ model with the software Sedfit⁶; b) A representative scanning electron microscopy (SEM) image of the synthesized SNPs after drying.

SI 2: AUC-SV and AUC-SE experiments for a monodisperse sample at a high concentration

A reverse micro-emulsion method⁷ and a subsequent seeded Stöber method⁸ were used for monodisperse, fluorescent-labeled silica nanoparticle synthesis with a final size of ca. 100 nm (as shown in **Figure S2a**). The detailed synthesis route is followed: Fluorescein/rhodamine labeled silica nanoparticles were regrown from 60 nm fluorescent labeled silica core particles. 3 ml (6.7 mg/ml) silica core dispersion was diluted with 1.5 ml 25% ammonia and 15.5 ml ethanol in a clean 50 ml glass reaction vessel. A mixture of 0.28 ml tetraethyl orthosilicate (TEOS) and 0.56 ml ethanol was then added. The reaction was carried out at room temperature with stirring at 800 rpm for overnight and results in particles of 100 nm. The surface charge number of the synthesized nanoparticle was ca. 130. As can be seen in **Figure S2b**, the concentration gradient formed in this case can only rise until ca. 40 vol% and Region III is missing, as compared to **Figure 4.1**.

Self-association and gelation of like-charged colloids at very high concentration

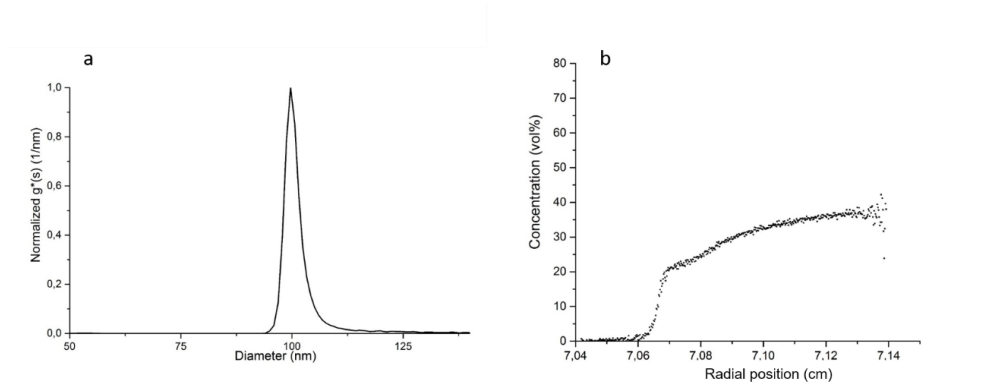


Figure S2: a) Size distribution by AUC-SV and b) Experimental sedimentation-diffusion equilibrium concentration profiles for the concentrated charged SNP suspensions at an initial concentration of ca. 15 vol% at 1100 rpm.

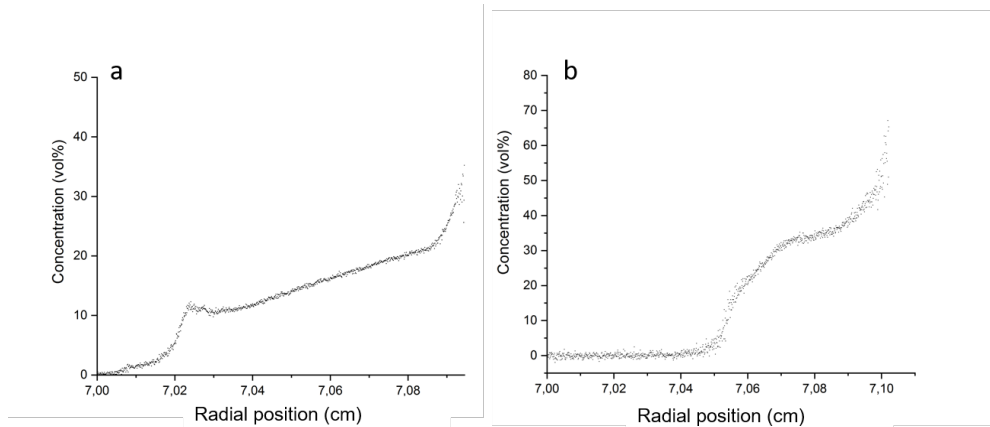


Figure S3: a) Experimental sedimentation-diffusion concentration equilibrium profiles for a concentrated charged SNP suspension at an initial concentration of 4 vol% and b) Experimental sedimentation-diffusion equilibrium profiles for a concentrated charged SNP at an initial concentration of 10 vol% of a different batch (diameter 140 nm).

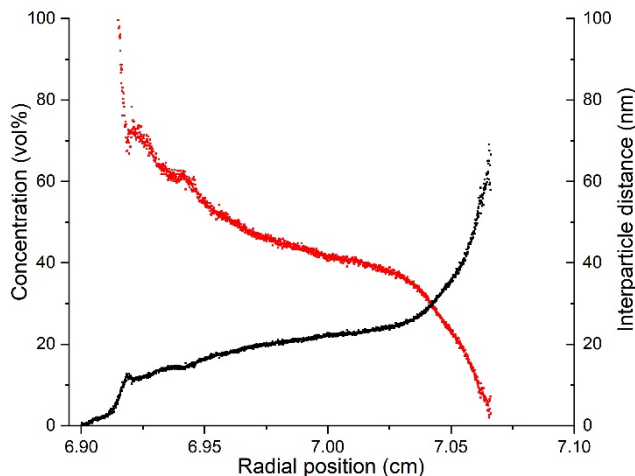


Figure S4: Experimental sedimentation-diffusion equilibrium concentration profile (black line) of 15 vol% SNPs at 1100 rpm and the conversion⁹ of the volume concentration to interparticle distance (red line) by the equation $d = 2r[(\varphi_m/\varphi)^{1/3} - 1]$, where d is the interparticle distance, r the particle radius, and φ and φ_m the volume concentration and the maximum volume concentration, respectively.

SI 3: The inclusion of a higher order virial coefficient

It might also be argued that using only a second virial coefficient (B_2) cannot describe the interactions properly. To verify whether adding a third virial coefficient (B_3) improves the fit, we excluded and included the third virial coefficient, as shown in Figure S5. The fit value for B_3 obtained is $1.1 \times 10^{-24} \pm 4.3 \times 10^{-14} \text{ mol}^2/(\text{kg}^2 \cdot \text{vol}\%)^2$, which is not significantly different from zero. An F-test was conducted to check whether adding B_3 is statistically necessary: at a significance level of 5%, the F-value must be smaller than 0.89 to make adding B_3 significant. The F-value can be calculated as the ratio of the two adjusted R-Square values in the two fits as shown in Figure S5: $0.99567/0.99646 = 0.999 > 0.89$. Thus, B_3 does not significantly improve the fit and we can omit higher order virial coefficients in our case. Qualitatively speaking, silica nanoparticles are so much larger than molecules that their number density is still low, although their volume fraction is high. Therefore, a higher order virial coefficient is not needed.

Self-association and gelation of like-charged colloids at very high concentration

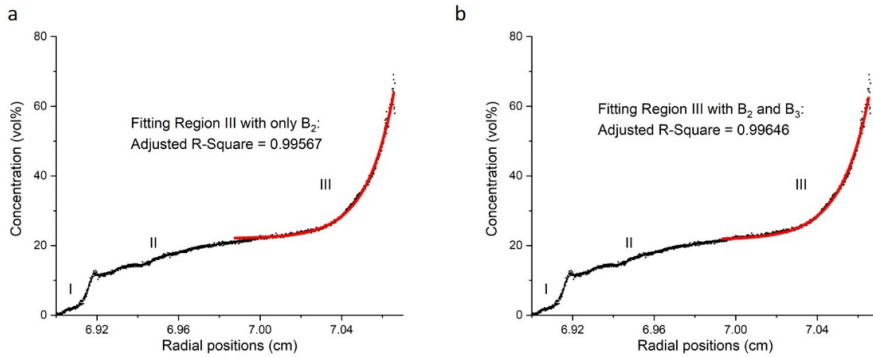


Figure S5: Fitting results of the region III by the inclusion of (a) only B_2 and (b) both B_2 and B_3 . Using B_2 only results in $B_2 = -7.8 \times 10^{-8} \pm 8.1 \times 10^{-10} \text{ mol}/(\text{kg}\cdot\text{vol}\%)$, while adding B_3 results in $B_2 = -9.4 \times 10^{-8} \pm 2.1 \times 10^{-7} \text{ mol}/(\text{kg}\cdot\text{vol}\%)$ and $B_3 = 1.1 \times 10^{-24} \pm 4.3 \times 10^{-14} \text{ mol}^2/(\text{kg}^2\cdot\text{vol}\%^2)$.

SI 4: Study of SD concentration profiles at various angular velocities

The value of L_ω is proportional to the reciprocal of ω , hence with increasing ω , L_ω becomes smaller, resulting in a much steeper slope for Region I and II. Therefore, at a high angular velocity, the profiles for Region I and II become nearly vertical. Thus, region III dominates the whole profile. **Equation 4.2** fitted the Region III profiles well and the obtained and the apparent molecular mass decreased with the angular velocity, as shown in **Figure S6b**. The fitted profile, as described by **Equation S2**, was extrapolated to zero angular velocity and the so-obtained apparent molecular mass equaled $2.7 \times 10^5 \text{ kg mol}^{-1}$, which agrees reasonably well with the actual molecular mass of the nanoparticles ($3.2 \times 10^5 \text{ kg}\cdot\text{mol}^{-1}$).

$$M \sim 1447 + 2.7 \times 10^5 \exp(-1 \times 10^{-3} \omega) \quad (\text{S2})$$

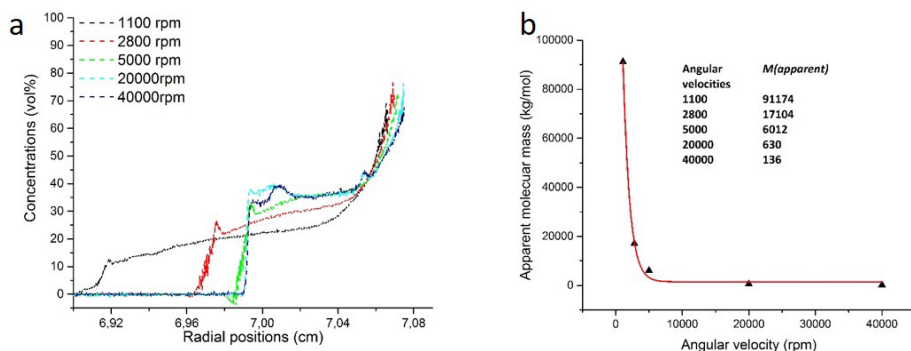


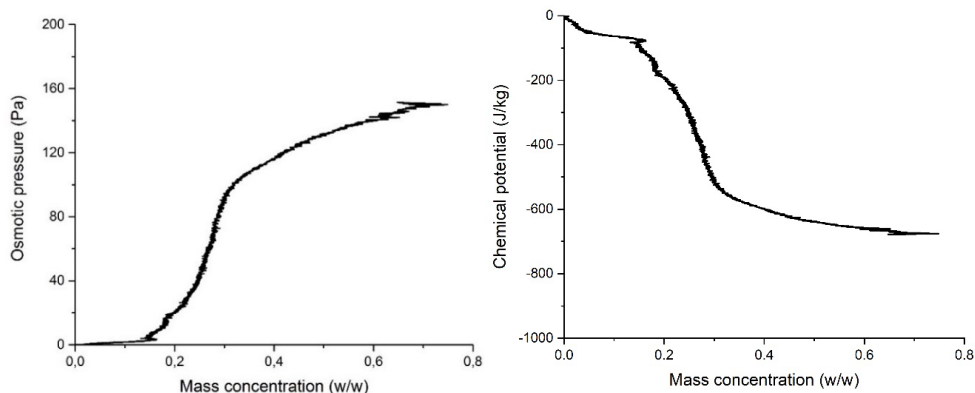
Figure S6: a. Sedimentation-diffusion equilibrium concentration profiles at different angular velocities ranging from 1100 rpm to 40,000 rpm; b. The fitted apparent molecular mass as a function of the angular velocity.

SI 5: The calculation of the chemical potential to illustrate the driving force for the gel formation

The sedimentation-diffusion equilibrium profile can be converted to an osmotic pressure difference $\Delta\Pi$ using **Equation S3**¹⁰:

$$\Delta\Pi = \omega^2 \left(\frac{\partial \rho}{\partial c} \right)_\mu \int_{r_m}^{r_1} c(r) r \, dr \quad (\text{S3})$$

where c is the mass concentration of the solute species, ω the angular velocity (equals 1100 rpm), and $\left(\frac{\partial \rho}{\partial c} \right)_\mu$ the density increment of the sample at constant chemical potential of water and salt, which was approximated using the density of the pure solvent and solid nanoparticles. By using **Equation S3**, **Figure S7** was calculated from **Figure 1** as a typical example.



Self-association and gelation of like-charged colloids at very high concentration

Figure S7 (left): Osmotic pressure change with mass concentration of concentrated charged silica nanoparticles, calculated from Figure 1 using **Equation (S3)**.

Figure S8 (right): Chemical potential change with mass concentration of concentrated charged silica nanoparticles.

The solvent chemical potential difference ($\Delta\mu$) can be calculated by the generalized Svedberg-Pedersen equation¹¹, as shown in **Equation S4**:

$$\Delta\mu = \omega^2 \int_{r_m}^r (1 - \rho\nu) r dr \quad (\text{S4})$$

where ν is the partial molar volume of the solvent and ρ is the gel density. By using **Equation S4**, **Figure S8** was calculated.

SI 6: pH gradient measurement and calibration

McCrumb indicator¹² is a universal pH indicator which changes color from red to brownish and then to violet with pH value increase. Therefore, the absorbance spectrum can be used to detect a pH value change along the concentration gradient of the silica nanoparticles. A series of calibrations was firstly done with dispersions of known pH values. As it is shown in **Figure S9a**, the absorbance at 430 nm was used to characterize the pH change in our system (the absorbance peak at 650 nm overlaps with the fluorescence absorption peaks, which induces errors). The relation between the absorbance and pH value was fitted as linear, shown in **Figure S9b**. Therefore, the absorbance difference at 430 nm before and after the addition of a tiny amount (ca. 1 μ l) of McCrumb indicator (**Figure S10**) can be converted to pH values. Thus, **Figure 4.3a** is plotted.

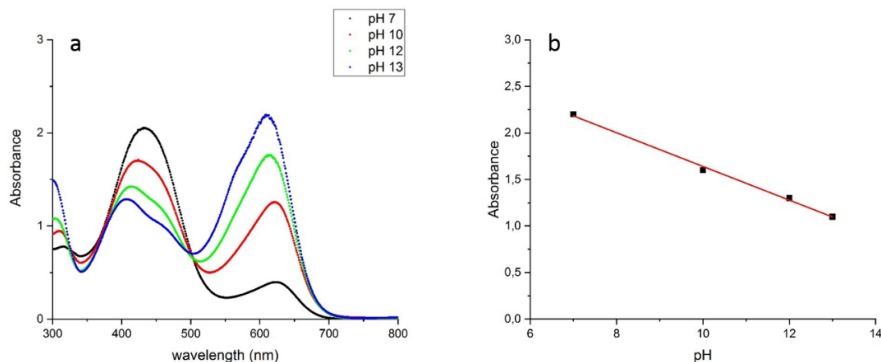


Figure S9: a) The absorbance spectrum of the home-made McCrumb indicator in dispersions of different known pH values; b) The absorbance at 430 nm at different pH values (black dots) and the plots follow a linear fitting curve (red): $y = 3.4 - 0.2x$ from pH 7 to pH 13.

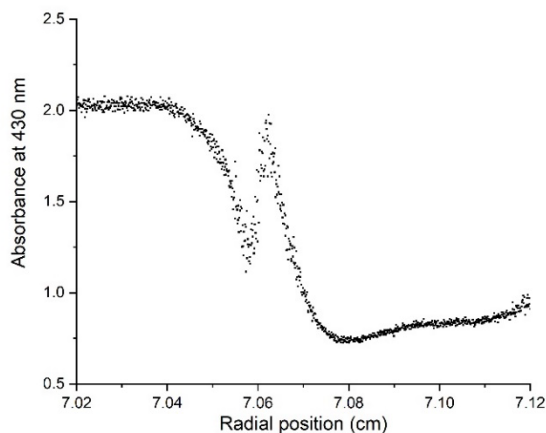


Figure S10: The absorbance gradient (at 430 nm) along the radius, characterized by pH indicator at the sedimentation-diffusion equilibrium for SNPs of an initial concentration of 15 vol% at 5000 rpm. The spike at the radius of ca. 7.06 cm is due to the phase boundary, similarly, as shown in **Figure 4.2a**.

SI 7: The calculation of hydroxide group density

When the concentration gradient reached the plateau, as shown in **Figure S11** (radial: 7.09 cm to 7.11 cm), the concentration is ca. 20 vol% and the pH value is 13 (as shown in **Figure 3a**). Since the diameter of SNPs is ca. 90 nm, the volume concentration (20 vol%) can be converted to the mole fraction ($9 \times 10^{-7} \text{ mol} \cdot \text{l}^{-1}$). As the dissociation constant for the water-glycerol mixture¹³ is about 14, the concentration of surface hydroxide groups (deprotonated) can be calculated from the pH value to be $1 \times 10^{-1} \text{ mol} \cdot \text{l}^{-1}$. Therefore, the number of hydroxide groups (deprotonated) can be estimated to be 4.4 per nm^2 . From the literature¹⁴, the surface silanol group concentration is 4.9 OH groups nm^{-2} so it means that due to the Donnan potential, 90% of silanol groups are deprotonated due to negative charge. At a higher radius of 7.12 cm, the concentration increased above 40 vol% and the pH value was found to decrease to 12, which means 10 times fewer hydroxyl groups were deprotonated. The counter-ion bridge at super crowding environment agrees very well with these findings.

Self-association and gelation of like-charged colloids at very high concentration

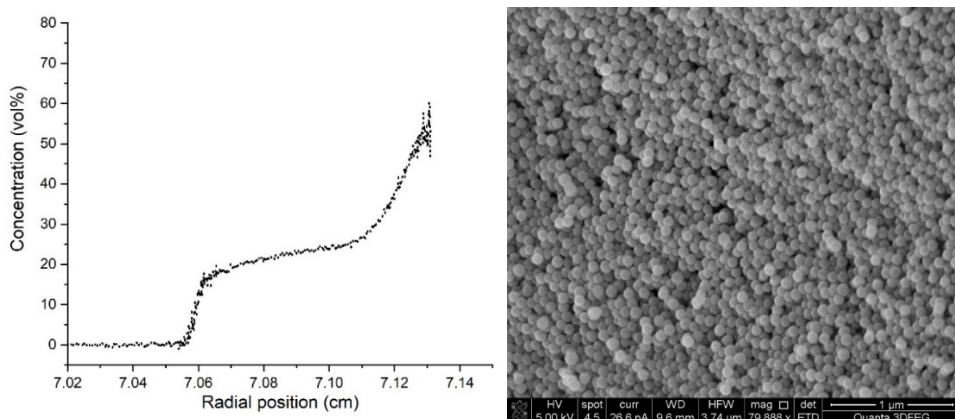


Figure S11 (left): Experimental sedimentation-diffusion equilibrium concentration profile at 5000 rpm for SNPs of an initial concentration of 15 vol% at 5000 rpm.

Figure S13 (right): The silica nanoparticles inside the gel. The gel was freeze-dried before SEM observation.

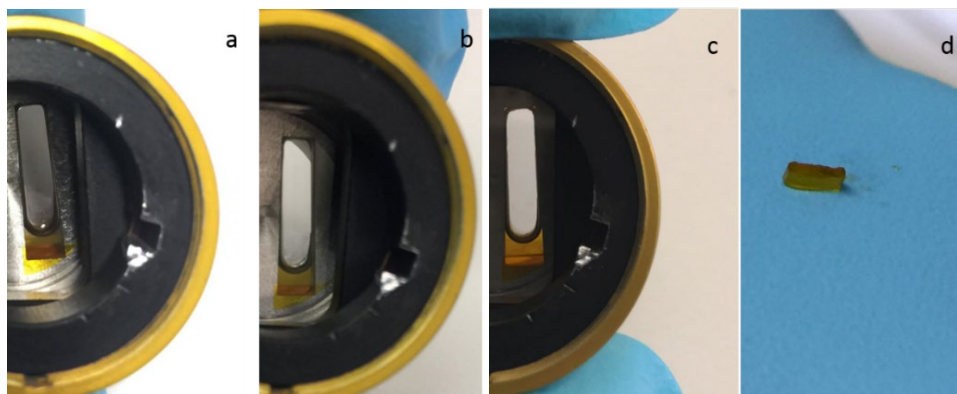


Figure S12: Images of the gel phase a) just after the AUC-SE experiment; b) overnight after the AUC-SE experiment; c) one month after the AUC-SE experiment and d) after taking the gel out of the AUC cell for 15 vol% SNPs.

SI 8: Gel stability experiment

The gel (size: ca.0.6 mm x 3 mm x 1.5 mm) formed after the sedimentation equilibrium experiment was taken out of the AUC cell by a tweezer and immersed in a glass vessel containing 1 ml supernatant solvent (80 vol% glycerol + 20 vol% water). The gel was weighed after 0.5 h, 1.5 h, 3.5 h 19 h and 67 h separately. The gel formed by the monodisperse nanoparticles, described in S12 is used as a reference. The gel mass change plot is shown in **Figure S14**.

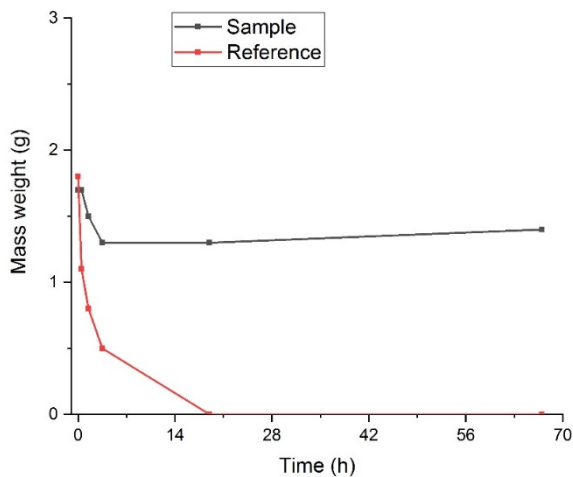


Figure S14: The gel weight change with time. After 19 h, the reference gel (formed by monodisperse nanoparticles, described in S12) was torn into pieces while the sample gel was still intact.

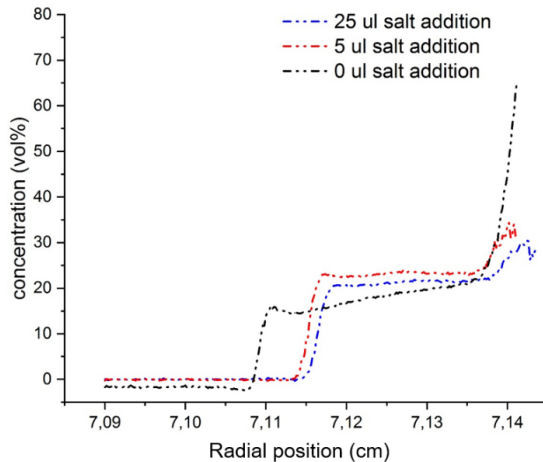


Figure S15: Experimental sedimentation-diffusion equilibrium concentration profiles after the addition of 1 M NaCl (in refractive index matching solvent) of 0 μ l, 5 μ l and 25 μ l into the AUC cell for 15 vol% SNPs at 5000 rpm.

SI 9: Other options for gel formation

First, residual van der Waals attraction. The residual vdW attraction and the electrostatic repulsion can be estimated¹⁵⁻¹⁶.

$$U_A = -\frac{A}{6} \left(\frac{2a^2}{(2a+H)^2 - 4a^2} + \frac{2a^2}{(2a+H)^2} + \ln \frac{(2a+H)^2 - 4a^2}{(2a+H)^2} \right) \quad (S5)$$

$$U_R = 2\pi\epsilon_r\epsilon_0 a \left(\frac{4kT}{ze} \tanh(ze\Psi_0/4kT) \right)^2 \ln[1 + \exp(-\kappa H)] \quad (S6)$$

$$A = A_{v=0} + A_{v>0} \approx \frac{3}{4} kT \left(\frac{\epsilon_1 - \epsilon_2}{\epsilon_1 + \epsilon_2} \right)^2 + \frac{3h\nu_e}{16\sqrt{2}} \frac{(n_1^2 - n_2^2)^2}{(n_1^2 + n_2^2)^{3/2}} \quad (S7)$$

where ϵ_1 is the dielectric constant of solvents, ϵ_2 is the dielectric constant of nanoparticles, n_1 is the refractive index of solvents, n_2 is the refractive index of nanoparticles, a is the particle radius, H is the interparticle distance and A is the Hamaker constant. Furthermore, Ψ_0 is the surface potential (approximated by the zeta potential ζ), κ is the reciprocal Debye length, z is the valency, e is the unit charge, ν_e is the so-called plasma frequency of the free electron gas, typically in the range $(3-5) \times 10^{15} \text{ s}^{-1}$ and h is the Planck constant.

For a typical sample of SiO_2 , the refractive index (n_2) at ca. 600 nm (the average wavelength used in AUC experiments) is 1.46. The extreme (unlikely) case is that glycerol might be preferably adsorbed on the surface of silica, which makes the solvent refractive index $n_1 = 1.47$. Moreover, the density inhomogeneity can be included: the vdW attraction is proportional to the density squared. If the density fluctuation $\Delta\rho$ in the silica particles is 0.2 g/cm^3 (which is already a large fluctuation) and silica has a density ρ of 1.6 g/cm^3 , the relative contribution of the fluctuations to the residual vdW force is about 26%. By considering these two effects, $U_A + U_R$ can be calculated, as shown in Figure S16. The repulsion force dominates when the interparticle distance is larger than 1 nm, amounts to about $7kT$ at 5 nm and the total interparticle interaction is not attractive until the interparticle distance is decreased below 0.2 nm. Therefore, the residual vdW attraction is unlikely to be the major contribution to the long-distance attraction in our findings, even if both the density fluctuation and refractive index change are considered.

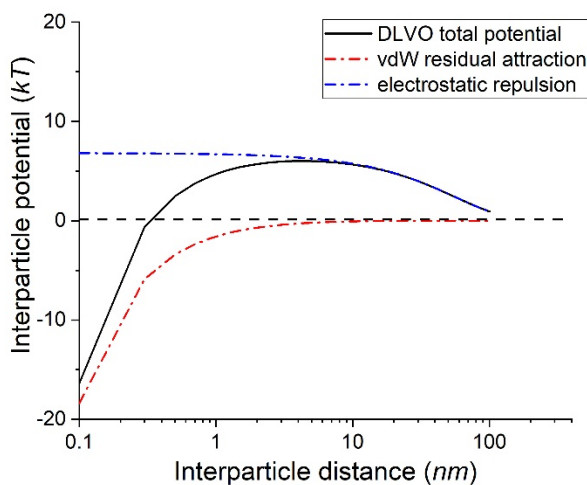


Figure S16: Interparticle potential versus interparticle distance. The residual vdW attraction and electrostatic repulsion are calculated to verify whether a residual vdW attraction and refractive index change due to glycerol adsorption could be the major reason for the long-distance attraction observed.

Second, particles may stick together because glycerol preferentially adsorbs on the silica particles and glycerol forms hydrogen bonds with silica surface silanols¹⁷. On the one hand, most of the experiments reported deal, however, with largely non-aqueous solvents¹⁸. The presence of excess of water in our system ($n(\text{glycerol}):n(\text{water}) = 1:1.05$) and the strong attraction between water and glycerol¹⁹ makes significant absorption of glycerol on silica unlikely due to the competitive hydrogen bonding formation among glycerol, water and the silica surface. On the other hand, even if it is true that glycerol is selectively adsorbed onto silica surface, making the refractive index 1.47, the residual vdW attraction is still too weak to induce net attraction at interparticle distance larger than 1 nm, as shown in Figure S16. The barrier height is about $7kT$, located at about 5 nm, while the contour length of glycerol is about $\sin(\tau/2) \times n \times l = 0.75$ nm. Here we assume that for glycerol the bond angle $\tau = 109^\circ$, so that $\sin(\tau/2) = 0.83$ and an average bond length $l = 0.15$ nm for the $n = 6$ bonds. As 5 nm $\gg 0.75$ nm, a liquid bridge is unlikely.

Third, a high pH might result in a rise in ionic strength because of dissolution of silica as the solubility of silica in water increases with pH, from about 100 ppm of dissolved silica to around 1000 ppm at pH 10¹⁷. The implication might be that silica on the surface can be dissolved into the form of H_3SiO_4^- ions in the glycerol-water mixture in Region III, which may suppresses double-layer repulsion to some extent. However, the aggregation due to the presence of these H_3SiO_4^- ions is highly unlikely because 1) the gel was shown to be reversible when made at a low rpm and 2) from the SEM image (Figure S12), signs of significant agglomeration are difficult to detect.

Self-association and gelation of like-charged colloids at very high concentration

Fourth and finally, soluble silica induces aggregation or gelation¹⁷ because when two particles are in (or close to in) contact, some silica may precipitate in the ‘neck’ between adjacent particles. However, the attraction in our case starts to work when the interparticle distance is ca. 30 nm (where Region III starts). In this case, particles are still too far to contact and form a precipitated ‘neck’. Moreover, the aggregation due to the presence of these H_3SiO_4^- ions is highly unlikely because, as indicated before, the gel was shown to be reversible when made at a low rpm and significant agglomeration is difficult to detect from the SEM image (Figure S12).

References

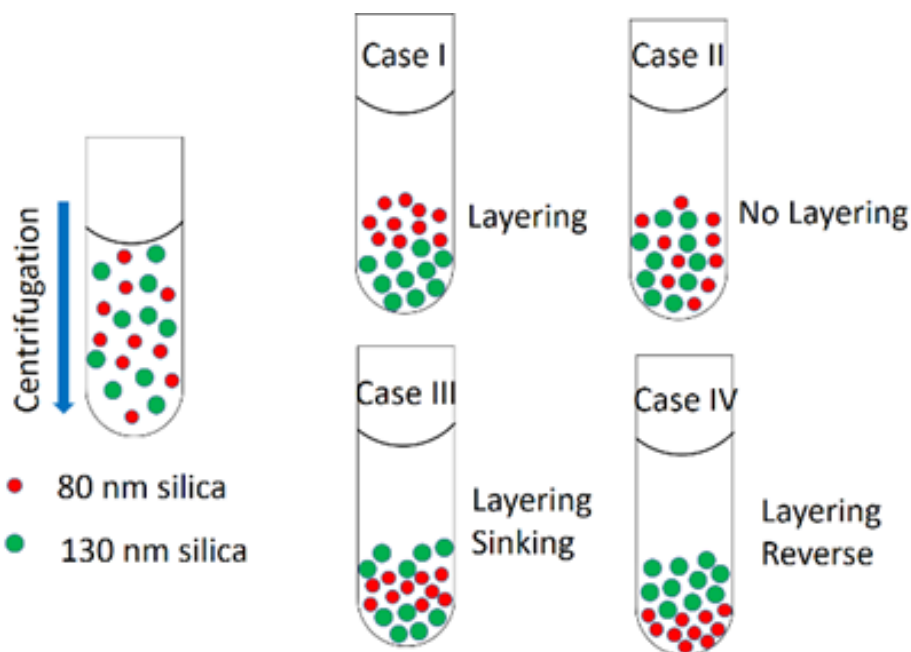
1. Xu, X.; Franke, T.; Schilling, K.; Sommerdijk, N. A. J. M.; Cölfen, H., Binary colloidal nanoparticle concentration gradients in a centrifugal field at high concentration. *Nano Letters* **2019**, *19* (2), 1136-1142.
2. Karabudak, E.; Cölfen, H., The multiwavelength uv/vis detector: New possibilities with an added spectral dimension. In *Analytical ultracentrifugation: Instrumentation, software, and applications*, Uchiyama S., A. F., Stafford W., Laue T., Ed. Springer, Tokyo: 2016.
3. Pearson, J.; Walter, J.; Peukert, W.; Cölfen, H., Advanced multiwavelength detection in analytical ultracentrifugation. *Analytical Chemistry* **2018**, *90* (2), 1280-1291.
4. Rasa, M.; Ern , B.; Zoetekouw, B.; van Roij, R.; Philipse, A., Macroscopic electric field and osmotic pressure in ultracentrifugal sedimentation–diffusion equilibria of charged colloids. *Journal of Physics: Condensed Matter* **2005**, *17* (15), 2293-2314.
5. Nieduszynski, I., Dynamic properties of biomolecular assemblies: Edited by se harding and aj rowe, royal society of chemistry, cambridge, 1989, pp. 374. Elsevier: 1990.
6. Schuck, P., Size-distribution analysis of macromolecules by sedimentation velocity ultracentrifugation and lamm equation modeling. *Biophysical Journal* **2000**, *78* (3), 1606-19.
7. Osseo-Asare, K.; Arriagada, F., Preparation of sio2 nanoparticles in a non-ionic reverse micellar system. *Colloids and Surfaces* **1990**, *50*, 321-339.
8. Giesche, H., Synthesis of monodispersed silica powders i. Particle properties and reaction kinetics. *Journal of the European Ceramic Society* **1994**, *14* (3), 189-204.
9. Hao, T.; Riman, R. E., Calculation of interparticle spacing in colloidal systems. *Journal of Colloid and Interface Science* **2006**, *297* (1), 374-377.
10. Brian, A.; Frisch, H.; Lerman, L., Thermodynamics and equilibrium sedimentation analysis of the close approach of DNA molecules and a molecular ordering transition. *Biopolymers: Original Research on Biomolecules* **1981**, *20* (6), 1305-1328.
11. Cölfen, H., Analytical ultracentrifuge technologies for the characterization of biopolymer gels and microgels. *Biotechnology and Genetic Engineering Reviews* **1999**, *16* (1), 87-140.
12. McCrumb, F., Use of wide-range indicators for determination of ph. *Industrial & Engineering Chemistry Analytical Edition* **1931**, *3* (3), 233-235.
13. Perrin, D. D., *Dissociation constants of organic bases in aqueous solution: Supplement 1972*. Butterworths: 1972.
14. Zhuravlev, L., Concentration of hydroxyl groups on the surface of amorphous silicas. *Langmuir* **1987**, *3* (3), 316-318.

CHAPTER 4

15. Physical–chemical aspects, *Polymer coatings*, With, G. d., Ed. Wiley - VCH Verlag GmbH & Co. KGaA: 2018.
16. Israelachvili, J. N., *Intermolecular and surface forces*. Academic press: 2015.
17. Iler, R. K., The chemistry of silica john wiley & sons. *New York* **1979**, 30-62.
18. Mazzieri, V.; Yori, J. C., Adsorptive properties of silica gel for biodiesel refining. *Energy & Fuels* **2008**, 22, 4281-4284.
19. Marcus, Y., Some thermodynamic and structural aspects of mixtures of glycerol with water. *Physical Chemistry Chemical Physics* **2000**, 2 (21), 4891-4896.

CHAPTER 5

Layering of Bidisperse Charged Nanoparticles in Sedimentation



The results described in this chapter are based on:

Xufeng Xu*, P.M. Biesheuvel, Helmut Cölfen and Evan Spruijt*. Layering of bidisperse charged nanoparticles in sedimentation. *Soft Matter* 2020, 16, 4718-4722

5. Layering of bidisperse charged nanoparticles in sedimentation

Layering of particle mixtures is common in nature. The most well-known example is called the Brazil nut effect¹⁻². Upon shaking or vibration, Brazil nuts, which are usually the largest nuts in the system, end up on top in a mixture of nuts with various sizes³. A reverse Brazil nut effect⁴⁻⁵ has also been reported in granular matter, as larger objects may sink to the bottom depending on the size and density of the mixture⁶. Going to smaller objects, the layering of micrometre-sized colloidal particles was recently observed in binary dispersions of particles of different sizes but identical density upon sedimentation by Velegol et al.⁷. They found smaller polystyrene latex (PSL) localized in a sharp layer above larger PSL after the sedimentation-diffusion equilibrium⁸ (SDE) was reached, which is fully reproducible in the size range from 1 μm to 5 μm . Due to the micrometre size range of the colloids, only the dominant gravitational energy of the system was considered to explain the spontaneous layering behaviour. The contribution of entropy and interparticle interaction to the system Gibbs free energy were both negligible. By contrast, in nanometre-sized particle mixtures, these two factors may play a prominent role, and research into their effects on layering is still missing. Moreover, different parameters including particle size, particle charge and relative g -force of the centrifugation would affect both the extent and position of layering by changing the system Gibbs free energy.

5.1. Introduction

In our study, we used bidisperse charged silica nanoparticles in a refractive index matching solvent as a model system to study the layering of nanometre-sized particles in the SDE. The advantage of this model system is that the normally occurring strong light scattering and severe turbidity at high colloidal concentrations⁹⁻¹⁰ can be minimized by the refractive index matching between silica and the glycerol water mixture (80 vol% + 20 vol%). Moreover, fluorescent labeling¹¹⁻¹³ of the silica nanoparticles (SNPs) was used to quantitatively measure the radial concentration of both particles at very high concentration in the analytical ultracentrifuge cell, which was achieved by multi wavelength analytical ultracentrifugation¹⁴⁻¹⁶ (MWL-AUC). From a theoretical perspective, we calculated the full sedimentation-diffusion equilibrium profiles using the Boublik–Mansoori–Carnahan–Starling–Leland (BMCSL) approximation for the hard-core excluded volume interactions, complemented with a Poisson-Boltzmann term to account for electrostatic interactions.¹⁷⁻¹⁸ We solved the ensuing differential equations numerically to simulate the layering of binary charged nanoparticles in the SDE, which carefully took into account both the entropic and enthalpic contributions to the system Gibbs free energy. From both the experimental and theoretical aspects, we found that the layering of nanoparticles was observed upon sedimentation which can be controlled by changing particle size, surface charge and centrifugal field strength (g -force), as shown in **Figure 5.1**. Counterintuitively, lighter nanoparticles were found to move below heavier ones when the surface charge was tuned carefully, which was demonstrated both by experiments and theoretical calculations. Overall, our study is a first step to quantitatively understand and delicately control the layering of

nanoparticle mixtures in sedimentation¹⁹, the concept of which can be used in sorting biological mixtures of different components and purifying polydisperse colloidal mixtures in the future.

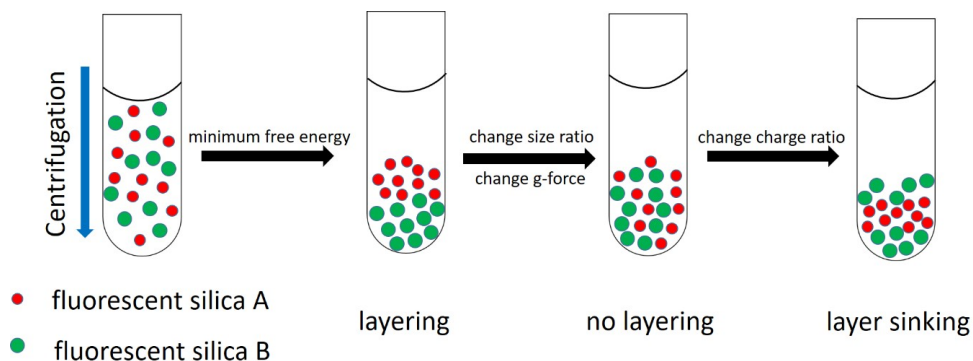


Figure 5.1: The schematic illustration of the layering. The layering can be formed by the sedimentation of bidisperse charged silica nanoparticles due to the minimum system Gibbs free energy. Layering can be suppressed by changing the size ratio of the particle mixture or the angular velocity of the centrifugation while layer sinking (the layer of the smaller nanoparticles sinks towards the bottom) can be observed by changing the charge ratio of the particle mixture.

5.2. Results and discussion

The fluorescent labeled SNPs with the diameter of 80 nm, 100 nm and 130 nm were synthesized by following the literature procedures²⁰⁻²² in two steps: 1) the particle core of 60 nm was first synthesized by the reverse micro-emulsion method²¹ and 2) different final sizes were then synthesized by the seeded Stöber growth method²² (the size distribution characterization by the analytical ultracentrifuge (AUC) and dynamic light scattering (DLS) is shown in **Figure S1** and **Figure S2**). The SDE profile for a binary mixture of 80 nm and 130 nm SNPs is shown in **Figure 5.2a** (the detailed AUC experiment set-up is described in **SI 1**) and the corresponding theoretical calculation result is shown in **Figure 5.2b** (the detailed theoretical calculation steps are described in **SI 2**). Qualitatively speaking, the experimental layering position of the smaller particles agreed very well with the theoretical result and the increasing concentration trend of the larger particles was described well by the theoretical calculation. However, experimentally the glass transition occurred at a significantly lower volume fraction due to the extended double layer²³⁻²⁴ (Debye length = 14 nm) for the charged colloids²⁵ in dispersion of a low ionic strength (0.5 mM). Therefore, the concentration gradient reached a plateau at 36 vol%. In comparison, the BMCSL model did not consider the glass transition but kept an increasing trend of the particle concentration along the radius. This leads to the deviation in **Figure 5.2b** (also in **Figure 5.3** and **Figure 5.4**). Nevertheless, by knowing the plateau concentration the effective hard sphere diameter can be estimated. The maximum effective hard sphere volume fraction is 64% (theoretical value for the Bernal (random close-packed) hard-sphere glass²⁶) and the particle volume fraction is 36% (experimental plateau value) for 130 nm SNPs. By using **Equation 5.1**, the

effective hard sphere diameter should be 1.2 times particle diameter and thus ca. 13 nm need to be added to the radius to compensate the electric double layer contribution (Debye length = 14 nm) to the effective hard sphere size.

$$\frac{\varphi_{\text{eff}}}{\varphi_{\text{p}}} = \left(\frac{\sigma_{\text{eff}}}{\sigma_{\text{p}}} \right)^3 \quad (5.1)$$

where φ_{eff} and φ_{p} are volume fraction of effective hard spheres and particles separately and σ_{eff} and σ_{p} are effective hard sphere diameter and particle diameter separately.

A solvent of a very high ionic strength (0.1 M) was used to induce a nearly hard sphere situation (as shown in **Figure S3**). By this means, the maximum total concentration reached 62 vol%, which is considerably close to the theoretical value for the random close-packed hard-sphere glass (64 vol%). The small deviation (2 vol%) can be explained by a thin layer of sterically stabilizing polyethylene glycol (PEG1000 Da, Flory radius 2.3 nm) which was used to avoid aggregation at this high ionic strength.

On the other hand, in order to quantify the layering, the layering extent (indicated as p value) for the binary nanoparticle mixture is introduced, as shown in **Equation 5.2**.

$$p = r_{\text{L}}^2 - r_{\text{S}}^2 \quad (5.2)$$

where r_{L} and r_{S} is the position of the largest first derivative value (steepest slope) for the larger and smaller SNPs, respectively.

Plot	r_{L}^2 (cm ²)	r_{S}^2 (cm ²)	p (cm ²)
experimental	49.98	49.77	0.21
theoretical	49.98	49.76	0.22

Table 5.1: The experimental and theoretical values of r_{L}^2 , r_{S}^2 and p corresponding to **Figure 5.2**.

The two typical positions r_{L} and r_{S} for the binary mixture of 80 nm and 130 nm SNPs are indicated in **Figure 5.2a**. The experimental and theoretical values were calculated and shown in **Table 5.1**. The agreement between the experimental and theoretical values is quite good (relative deviation of p value: 0.05). The same binary mixture of 80 nm and 130 nm SNPs with a varied number ratio (1/2), ionic strength (5 mM) and total volume (20 μ l) were also tested, as shown in **Figure S4** and **Table S2**. The steady values of p (0.19 ± 0.03 cm²) in these cases demonstrate that the layering effect is repeatable regardless of the number ratio of the binary particles, the total sample volume and the ionic strength (up to 50 mM). The dynamics of the sedimentation process is also briefly illustrated by two snapshots at time 11h and 21h during the sedimentation process. In **Figure 5.2c** and **d**, a typical concentration bump of the slow sedimenting species (80 nm SNPs) appeared, centripetal to the boundary of the fast sedimenting species (130 nm SNPs) during the sedimentation process. This interesting hydrodynamic phenomenon is known as the Johnston-Ogston²⁷⁻²⁹ effect (J-O effect), which is due to hydrodynamic interaction between the two sedimenting species during the

Layering of bidisperse charged nanoparticles in sedimentation

centrifugation process. The dynamic sedimentation process^{18, 30} may be simulated by Newtonian hydrodynamics.

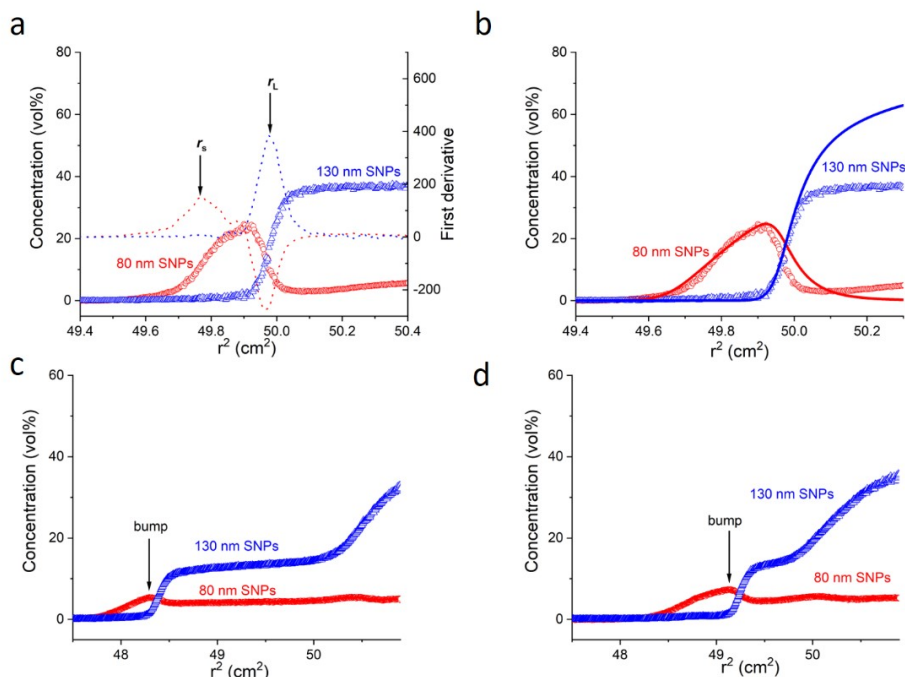


Figure 5.2: Experimental sedimentation-diffusion equilibrium (SDE) profiles for the binary mixture of 80 nm RITC-SNPs and 130 nm FITC-SNPs (number ratio: 1:1, sample volume 10 μ l, initial concentration 20 vol%, ionic strength 0.5 mM) at 1100 rpm and 25 $^{\circ}$ C. In a) the positions of r_s and r_L are indicated. In b) the theoretically calculated profiles (solid line) are overlapped with the experimental profiles (scatter). The parameters used in the calculation are described in SI 2. c) and d) are two snapshots of the concentration profiles at 11 h and 21 h after the sedimentation is executed (at 41 h the equilibrium is reached). The concentration bump due to the Johnston-Ogston effect is marked by arrows.

The effects of relative g-force/centrifugal field strength and particle size ratio are both shown in **Figure 5.3**. In **Figure 5.3a**, when a higher g force was applied with the angular velocity increasing from 1100 rpm to 5000 rpm, both nanoparticles moved closer to the bottom and no obvious layering was found any longer with the p value decreasing to 0.02 cm² from 0.19 cm² (the detailed calculation is shown in **Table S3**). The theoretical values of r_L^2 , r_S^2 and p agreed well with the experimental values while for the concentration gradient profiles, the only discrepancy occurred approaching the bottom. The experimental profile reached a plateau due to the glass transition which was not considered in the BMCLS model. In **Figure 5.3b**, when the particle size ratio decreased slightly from 1.6 to 1.3 (130 nm/80 nm to 130 nm/100 nm), the layering became much less pronounced with the layering extent p value decreasing to 0.07 cm² from 0.19 cm². This demonstrates that the size ratio affects

strongly the layering. The theoretical calculation also succeeded to predict the layering extent value p very well, as shown in **Table S3**. Overall, both increasing g -force and decreasing particle size can reduce the layering significantly, which was demonstrated from both experimental and theoretical aspects.

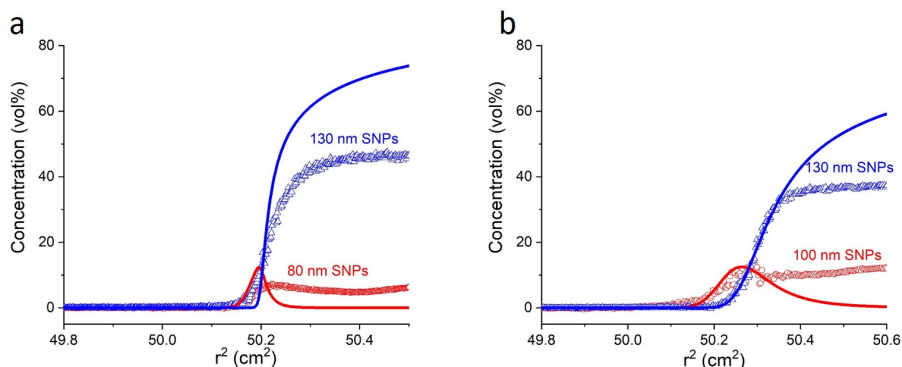


Figure 5.3: Experimental (scatter) and theoretical (solid line) sedimentation-diffusion equilibrium (SDE) profiles for a) the binary mixture of 80 nm RITC-SNPs and 130 nm FITC-SNPs at 5000 rpm and 25 °C and b) the binary mixture of 100 nm RITC-SNPs and 130 nm FITC-SNPs at 1100 rpm and 25 °C. The parameters used in the calculation are described in **SI 2**.

To investigate the effect of the particle surface charge on the layering, two strategies were used: the chargeable surface hydroxyl groups were mostly passivated by reaction with PEG-silane and their charge could be restored by reaction with an amino-silane. From the theoretical calculation¹⁸, lighter (smaller) particles are expected to sink below heavier (bigger) ones when the surface charge of heavier particles is significantly larger than that of the lighter ones. This was achieved experimentally by the introduction of amino groups³¹ to 130 nm SNPs (the experimental details are shown in **SI 3**). In an acidic environment (pH 2 and 3), the remaining hydroxide groups on the silica surface after the PEG-silane reaction were neutralized while the charge of amino groups was tuned by varying acidities (from 10^{-3} M HCl in **Figure 5.4a** to 10^{-2} M HCl in **Figure 5.4b**). Therefore, the surface charge of 130 nm SNPs was tuneable while 80 nm SNPs remained neutral (**Table S5**). In **Figure S5**, with the increasing acidity the layer of the smaller nanoparticles gradually moves towards the bottom and the p value gradually decreases (detailed calculations are shown in **Table S4**). More intriguingly, the ‘reverse’ layering might occur, predicted from the theoretical calculation, as shown in **Figure 5.5**. When the surface charge number (Z) of the larger nanoparticles is substantially increased (from 200 to 950) and the charge of smaller ones is kept close to zero, the layering can be reversed which indicates that heavier nanoparticles can float above lighter ones.

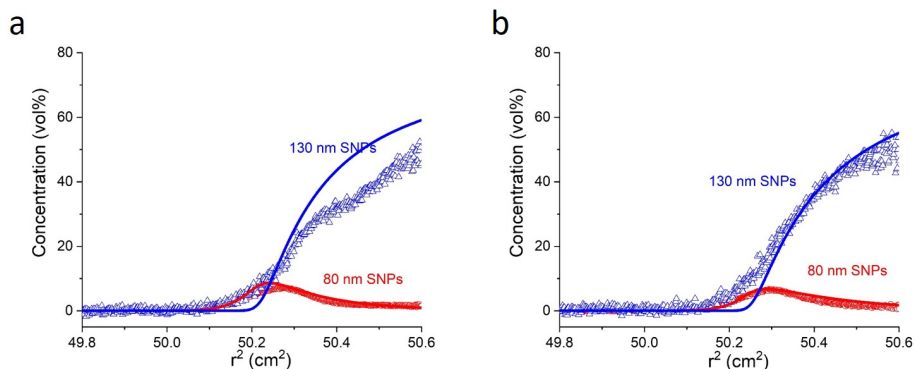


Figure 5.4: Experimental (scatter) and corresponding theoretical (solid line) sedimentation-diffusion equilibrium (SDE) profiles for the binary mixture of 80 nm RITC-SNPs and 130 nm FITC-SNPs at 1100 rpm and 25 °C of different acidities: a) 0.001M HCl; b) 0.01M HCl. The parameters used in the calculations are described in **SI 2**.

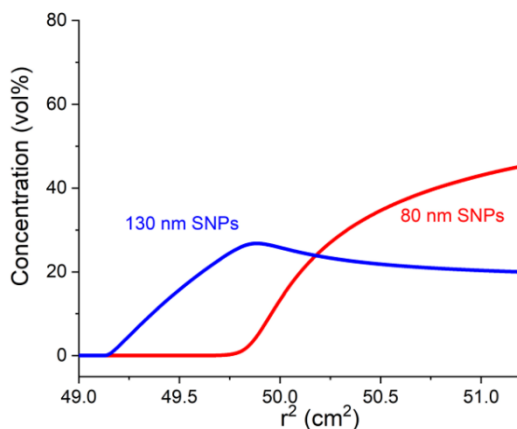


Figure 5.5: 'Reverse' layering predicted by the theoretical calculation. 130 nm SNPs reverse and layer above 80 nm SNPs when the charge of 130 nm SNPs is substantially increased while the charge of 80 nm SNPs remains nearly neutral.

5.3. Conclusion

In summary, we showed that bidisperse nanoparticles can be segregated and layered in the sedimentation-diffusion equilibrium due to thermodynamic driving force/ lowest system Gibbs energy. By applying an accurate equation of state for multicomponent mixtures (of particles of unequal sizes), the layering can be predicted quite well, with the consideration of hard-core excluded volume interactions and electrostatic interactions in addition to gravitational energy¹⁷. The layering was also shown to disappear by applying a stronger g-force or decreasing the size ratio. More interestingly, by tuning the particle surface charge

carefully, the layering of lighter nanoparticles is illustrated to be able to move below the heavier nanoparticles. The theoretical calculation even predicts a ‘reverse’ layering when the surface charge of larger nanoparticles is extensively increased. This study can be applied to particle segregation in the dispersions of polydisperse particles, which is very common in research and industry. In addition, the purification of polydisperse particles remains an intriguing topic and this paper may give some hints to use thermodynamic driving force to purify colloidal particles, which is another approach besides to high-speed ultracentrifugation assisted purification due to kinetic driving force³²⁻³⁴.

5.4. References

1. Brown, R., The fundamental principles of segregation. *The Institute of Fuel* **1939**, *13*, 15-23.
2. Möbius, M. E.; Lauderdale, B. E.; Nagel, S. R.; Jaeger, H. M., Brazil-nut effect: Size separation of granular particles. *Nature* **2001**, *414* (6861), 270.
3. Rosato, A.; Strandburg, K. J.; Prinz, F.; Swendsen, R. H., Why the brazil nuts are on top: Size segregation of particulate matter by shaking. *Physical Review Letters* **1987**, *58* (10), 1038.
4. Huerta, D. A.; Ruiz-Suárez, J. C., Vibration-induced granular segregation: A phenomenon driven by three mechanisms. *Physical Review Letters* **2004**, *92* (11), 114301.
5. Breu, A. P.; Ensner, H.-M.; Kruelle, C. A.; Rehberg, I., Reversing the brazil-nut effect: Competition between percolation and condensation. *Physical Review Letters* **2003**, *90* (1), 014302.
6. Shinbrot, T., The brazil nut effect — in reverse. *Nature* **2004**, *429* (6990), 352-353.
7. Serrano, C. G.; McDermott, J. J.; Velegol, D., Sediments of soft spheres arranged by effective density. *Nature Materials* **2011**, *10* (9), 716-721.
8. Cölfen, H., Analytical ultracentrifugation of colloids. In *Analytical ultracentrifugation: Techniques and methods*, SCOTT, D. J., ed. and others, Ed. Cambridge: Royal Society of Chemistry: UK, 2005; Vol. 23, pp 501-583.
9. Xu, X.; Franke, T.; Schilling, K.; Sommerdijk, N. A. J. M.; Cölfen, H., Binary colloidal nanoparticle concentration gradients in a centrifugal field at high concentration. *Nano Letters* **2019**, *19* (2), 1136-1142.
10. Xu, X.; Cölfen, H., Binary colloidal nanoparticles with a large size ratio in analytical ultracentrifugation. *ChemPhysChem* **2019**, *20* (14), 1799-1803.
11. Van Blaaderen, A.; Vrij, A., Synthesis and characterization of colloidal dispersions of fluorescent, monodisperse silica spheres. *Langmuir* **1992**, *8* (12), 2921-2931.
12. Verhaegh, N. A.; van Blaaderen, A., Dispersions of rhodamine-labeled silica spheres: Synthesis, characterization, and fluorescence confocal scanning laser microscopy. *Langmuir* **1994**, *10* (5), 1427-1438.
13. Ma, K.; Mendoza, C.; Hanson, M.; Werner-Zwanziger, U.; Zwanziger, J.; Wiesner, U., Control of ultrasmall sub-10 nm ligand-functionalized fluorescent core-shell silica nanoparticle growth in water. *Chemistry of Materials* **2015**, *27* (11), 4119-4133.
14. Karabudak, E.; Cölfen, H., The multiwavelength uv/vis detector: New possibilities with an added spectral dimension. In *Analytical ultracentrifugation: Instrumentation, software, and applications*, Uchiyama S., A. F., Stafford W., Laue T., Ed. Springer, Tokyo: 2016.

15. Pearson, J.; Walter, J.; Peukert, W.; Cölfen, H., Advanced multiwavelength detection in analytical ultracentrifugation. *Analytical Chemistry* **2018**, *90* (2), 1280-1291.
16. Zhao, H.; Brautigam, C. A.; Ghirlando, R.; Schuck, P., Overview of current methods in sedimentation velocity and sedimentation equilibrium analytical ultracentrifugation. *Current Protocols in Protein Science* **2013**, 20.12. 1-20.12. 49.
17. Biesheuvel, P.; Lyklema, J., Sedimentation–diffusion equilibrium of binary mixtures of charged colloids including volume effects. *Journal of Physics: Condensed Matter* **2005**, *17* (41), 6337-6352.
18. Spruijt, E.; Biesheuvel, P. M., Sedimentation dynamics and equilibrium profiles in multicomponent mixtures of colloidal particles. *Journal of Physics: Condensed Matter* **2014**, *26* (7), 075101.
19. Julien, P. Y., *Erosion and sedimentation*. Cambridge University Press: 2010.
20. van der Hoeven, J. E.; van der Wee, E. B.; de Winter, D. M.; Hermes, M.; Liu, Y.; Fokkema, J.; Bransen, M.; van Huis, M. A.; Gerritsen, H. C.; de Jongh, P. E., Bridging the gap: 3d real-space characterization of colloidal assemblies via fib-sem tomography. *Nanoscale* **2019**, *11* (12), 5304-5316.
21. Osseo-Asare, K.; Arriagada, F., Preparation of sio2 nanoparticles in a non-ionic reverse micellar system. *Colloids and Surfaces* **1990**, *50*, 321-339.
22. Giesche, H., Synthesis of monodispersed silica powders i. Particle properties and reaction kinetics. *Journal of the European Ceramic Society* **1994**, *14* (3), 189-204.
23. Bryant, G.; Williams, S. R.; Qian, L.; Snook, I.; Perez, E.; Pincet, F., How hard is a colloidal “hard-sphere” interaction? *Physical Review E* **2002**, *66* (6), 060501.
24. Royall, C. P.; Poon, W. C.; Weeks, E. R., In search of colloidal hard spheres. *Soft Matter* **2013**, *9* (1), 17-27.
25. Van der Linden, M. N.; El Masri, D.; Dijkstra, M.; van Blaaderen, A., Expansion of charged colloids after centrifugation: Formation and crystallisation of long-range repulsive glasses. *Soft Matter* **2013**, *9* (48), 11618-11633.
26. Pusey, P. N.; van Megen, W., Phase behaviour of concentrated suspensions of nearly hard colloidal spheres. *Nature* **1986**, *320* (6060), 340-342.
27. Soda, A.; Fujimoto, T.; Nagasawa, M., Johnston-ogston effect in sedimentation. *The Journal of Physical Chemistry* **1967**, *71* (13), 4274-4281.
28. Correia, J. J.; Johnson, M. L.; Welss, G. H.; Yphantis, D. A., Numerical study of the johnston-ogston effect in two-component systems. *Biophysical chemistry* **1976**, *5* (1-2), 255-264.
29. Johnston, J. P.; Longuet-Higgins, H. C.; Ogston, A. G., On the distribution of the molecular weights of proteins. *Transactions of the Faraday Society* **1945**, *41* (0), 588-593.
30. Dhont, J. K. G., Thermodiffusion of interacting colloids. I. A statistical thermodynamics approach. *The Journal of Chemical Physics* **2004**, *120* (3), 1632-1641.
31. Pham, K. N.; Fullston, D.; Sagoe-Crentsil, K., Surface modification for stability of nano-sized silica colloids (retraction of vol 315, pg 123, 2007). *Journal of Colloid and Interface Science* **2010**, *342* (2), 643-643.
32. Chen, G.; Wang, Y.; Tan, L. H.; Yang, M.; Tan, L. S.; Chen, Y.; Chen, H., High-purity separation of gold nanoparticle dimers and trimers. *Journal of the American Chemical Society* **2009**, *131* (12), 4218-4219.

CHAPTER 5

33. Sun, X.; Tabakman, S. M.; Seo, W. S.; Zhang, L.; Zhang, G.; Sherlock, S.; Bai, L.; Dai, H., Separation of nanoparticles in a density gradient: FeCo@ c and gold nanocrystals. *Angewandte Chemie International Edition* **2009**, *48* (5), 939-942.
34. Qiu, P.; Mao, C., Viscosity gradient as a novel mechanism for the centrifugation-based separation of nanoparticles. *Advanced Materials* **2011**, *23* (42), 4880-4885.

5.5. Appendix

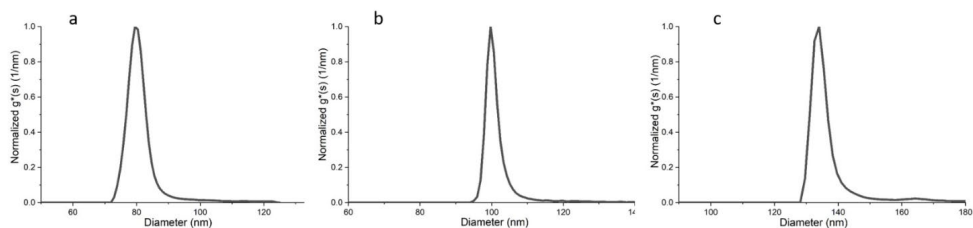


Figure S1: Particle size distributions of the three different types of silica nanoparticles (SNPs), used in the study, including a) 80 nm Rhodamine (RITC)-labeled SNPs; b) 100 nm RITC-labeled SNPs and c) 130 nm Fluorescein (FITC)-labeled SNPs, converted from the sedimentation coefficient distribution¹ and measured by analytical ultracentrifugation (AUC).

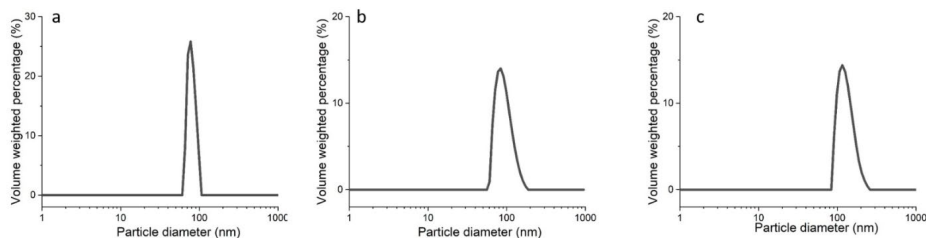


Figure S2: Particle size distributions of the three different types of silica nanoparticles (SNPs), used in the study, including a) 80 nm RITC-labeled SNPs; b) 100 nm RITC-labeled SNPs and c) 130 nm FITC-labeled SNPs, measured by Dynamic Light Scattering (Litesizer™ 500, Anton-Paar). The polydispersity index (PDI) of the three types of SNPs were 3.5%, 1.5% and 3.1% separately which indicated the high monodispersity of the samples.

SI 1: Detailed AUC experiment set-up

In a typical sedimentation–diffusion equilibrium (SDE) experiment, a 10 μl sample of the binary nanoparticle dispersion at a typical initial concentration of 20 vol% was mixed well and injected into the sample channel of an AUC cell of 1.5 mm pathlength. A 20 μl solvent of 80 vol% glycerol + 20 vol% water was injected into the reference cell. The filled AUC cell was then placed into a custom-made Multi-Wavelength Analytical Ultracentrifuge²⁻⁴ (MWL-AUC). The measurement settings were: Temperature 25°C; Wavelength range 250–700 nm; Radial step size: 2 μm . After the time scale of about 4 days, the sedimentation–diffusion equilibrium was normally reached by checking if the sedimentation profiles of the last 10 h overlapped.

SI 2: Detailed theoretical calculation steps

To calculate sedimentation-diffusion equilibrium (SDE) profiles in a mixture of charged, spherical particles at high volume fractions, we follow the general approach outlined in the literature⁵. Briefly, we consider a mixture of particles $i = 1:M$ with hard cores diameters σ_i , mass densities ρ_i and total charge $Q_i = Z_i e$, with a (local) volume fraction $\phi_i(r)$ in a continuum fluid a mass density ρ_F . For every type of particle, the total potential can be written as the sum of its electrochemical potential, contribution due to the external (centrifugal) field, and the insertion potential against the total pressure:

$$\begin{aligned}\mu_i^{\text{tot}} &= \mu_i^{\text{id}} + \mu_i^{\text{exc}} + \mu_i^{\text{el}} + \mu_i^{\text{ext}} + v_i P^{\text{tot}} \\ &= \ln \phi_i + \mu_i^{\text{exc}} + Q_i \psi + \frac{m_i \omega^2 r^2}{2} + v_i (P^h - \Pi)\end{aligned}\quad (\text{S1})$$

where $\mu_i^{\text{id}} + \mu_i^{\text{exc}}$ is the chemical potential split into an ideal contribution $\mu_i^{\text{id}} = \ln \phi_i$ and an excess contribution (for which very good empirical expressions exist, such as BMCSL for mixtures of hard spheres). $\mu_i^{\text{el}} = Q_i \psi = k_B T Z_i y$ is the contribution due to the electrostatic potential of charged particles in a mean-field approximation ($Q_i = Z_i e$ is the particle charge, and $y = e\psi/k_B T$ is the dimensionless electrostatic potential). μ_i^{ext} is the contribution due to an external field; in this section we will specifically consider a centrifugal field, hence, $\mu_i^{\text{ext}} = m_i \omega^2 r/2$. Finally, $v_i P^{\text{tot}}$ is the insertion energy, required to insert a particle of type i against the total pressure.

The expression for the total potential in **Equation S1** can be written in terms of forces, by taking the derivative with respect to z ($F = -\partial\mu^{\text{tot}}/\partial r$). The SDE profile of a particle can be found by requiring that the net force acting on the particle is 0 (which is an optimization of the total potential μ_i^{tot}). The gradient of the hydrostatic pressure, $\frac{\partial P^h}{\partial r} = -\rho_{\text{susp}} \omega^2 r$, and in SDE, $\frac{\partial \Pi}{\partial r} = -\omega^2 r (\rho_{\text{susp}} - \rho_F)$. Hence, in SDE, the density difference between the particle and the fluid can be used to calculate the SDE profiles.

After some rewriting, this gives for mixture of particles in a centrifugal field:

$$\frac{r}{L_{\omega,i}^2} = -\frac{1}{\phi_i} \frac{\partial \phi_i}{\partial r} - \beta \sum_j \frac{\partial \mu_i^{\text{exc}}}{\partial \phi_j} \frac{\partial \phi_j}{\partial r} + \frac{\partial Z_i}{\partial r} y - Z_i \frac{\partial y}{\partial r}\quad (\text{S2})$$

where $\beta = 1/k_B T$ and $L_{\omega,i} = \sqrt{\frac{k_B T}{v_i (\rho_i - \rho_F) \omega^2}}$ is the centrifugal length. For particles with a fixed charge Z_i , the term $(\partial Z_i / \partial r)$ equals 0.

The mean-field electrostatic potential is related to the particle volume fraction via the condition of local electro-neutrality⁵:

$$\sum_j \frac{Z_j \phi_j}{v_j} - 2n_b (1 - \tilde{\phi}) \sinh y = 0\quad (\text{S3})$$

Layering of bidisperse charged nanoparticles in sedimentation

where n_b is the number density of monovalent ions in the bulk, and $\bar{\phi} = \sum_j \phi_j$ is the total fraction of the volume occupied by particles at a particular position r . Note that we do not explicitly calculate the counterion concentration profiles across the SDE profiles, and thus, we do not account for the locally enhanced number densities of counterions in the sediments with very high volume fractions of particles. To do so, one would have to include an additional force balance for the ions and solve their concentration profile self-consistently with the SDE profiles of the colloids. We plan to address the contribution of this in a future contribution.

Here, we assume that the all particles have a fixed charge Z_i . For an explanation how to take into account charge regulation of the particle charge, we refer to the literature⁶. For the experimental profiles shown in the main text, we found that including a regulated surface charge does not substantially change the SDE profiles for the experimentally determined particle charges and fitted ionic strength.

If all particles have a fixed charge, **Equation S3** can be rewritten, leading to the following expression for the electrostatic potential y :

$$y = \operatorname{arcsinh} \left(\sum_i \frac{Z_i \phi_i}{2n_b v_i (1-\bar{\phi})} \right) \quad (\text{S4})$$

The derivative of the electrostatic potential that is included in **Equation S2**, can then be written as follows:

$$\frac{\partial y}{\partial r} = \frac{1}{\sqrt{\alpha^2 + (1-\bar{\phi})^2}} \sum_i \frac{\partial \phi_i}{\partial r} \left(\frac{Z_i}{2n_b v_i} + \frac{\alpha}{(1-\bar{\phi})} \right) \quad (\text{S5})$$

with $\alpha = \sum_j \frac{Z_j \phi_j}{2n_b v_j}$. To find the SDE profiles of all charged particles in a mixture, we insert **Equation S5** in the force balance of **Equation S2** and collect all derivatives of the concentration profiles, and write the set of equations in matrix form⁵:

$$-\begin{pmatrix} 1/L_{\omega,1}^2 \\ 1/L_{\omega,2}^2 \\ \dots \end{pmatrix} = \begin{pmatrix} \mu_{11} & \mu_{12} & \dots \\ \mu_{21} & \mu_{22} & \dots \\ \dots & \dots & \dots \end{pmatrix} \begin{pmatrix} \partial \phi_1 / r \partial r \\ \partial \phi_2 / r \partial r \\ \dots \end{pmatrix} \quad (\text{S6})$$

where:

$$\mu_{ij} = \mu_{ij}^{\text{id}} + \mu_{ij}^{\text{exc}} + \mu_{ij}^{\text{el}}$$

and:

$$\begin{aligned} \mu_{ii}^{\text{id}} &= \frac{1}{\phi_i} & \mu_{ii}^{\text{exc}} &= \frac{\partial \mu_i^{\text{exc}}}{\partial \phi_i} & \mu_{ii}^{\text{el}} &= \frac{Z_i^2}{2n_b v_i \sqrt{\alpha^2 + (1-\bar{\phi})^2}} + \frac{Z_i \alpha}{\sqrt{\alpha^2 (1-\bar{\phi})^2 + (1-\bar{\phi})^4}} \\ \mu_{ij}^{\text{id}} &= 0 & \mu_{ij}^{\text{exc}} &= \frac{\partial \mu_i^{\text{exc}}}{\partial \phi_j} & \mu_{ij}^{\text{el}} &= \frac{Z_i Z_j}{2n_b v_j \sqrt{\alpha^2 + (1-\bar{\phi})^2}} + \frac{Z_i \alpha}{\sqrt{\alpha^2 (1-\bar{\phi})^2 + (1-\bar{\phi})^4}} \end{aligned}$$

CHAPTER 5

Hard sphere excluded volume interactions can be included using the empirical BMCSL equation of state. The expression for μ_i^{exc} and the analytical expression for the partial derivative ($\mu_{ij}^{exc} = \partial\mu_i^{exc}/\partial\phi_j$) can be found elsewhere⁵.

For a two-component mixture, the expressions for $\partial\phi_1/\partial r$ and $\partial\phi_2/\partial r$ can be written explicitly:

$$\frac{\partial\phi_1}{r\partial r} = \frac{\mu_{12}/L_{\omega,2}^2 - \mu_{22}/L_{\omega,1}^2}{\mu_{11}\mu_{22} - \mu_{12}\mu_{21}} \qquad \frac{\partial\phi_2}{r\partial r} = \frac{\mu_{21}/L_{\omega,1}^2 - \mu_{11}/L_{\omega,2}^2}{\mu_{11}\mu_{22} - \mu_{12}\mu_{21}}$$

We solve this set of equations numerically in Matlab using a finite difference scheme. The resulting profiles are shown in the main text as solid lines.

In the theoretical calculations, the surface charges used for different SNPs are listed in **Table S1**. They can be experimentally estimated by using the Debye-Hückel approximation⁷. From the theoretical calculations, the surface particle charge cannot be neutralized completely and there is always a small amount of charge left even after reacting with PEG-silane and being dispersed in acidic environment. The ionic strength used in the calculations (3 mM) is slightly higher than the experimental value (0.5 mM). The deviation may due to the counter-ion accumulation with a higher particle concentration in the sedimentation.

Particles	Surface charge number (<i>Z</i>)
80 nm SNPs	110
100 nm SNPs	130
130 nm SNPs	200
80 nm s-SNPs	12
130 nm APTS-s-SNPs (in 0.001M HCl)	80
130 nm APTS-s-SNPs (in 0.001M HCl)	90

Table S1: The surface charge number *Z* used in the theoretical calculations.

Layering of bidisperse charged nanoparticles in sedimentation

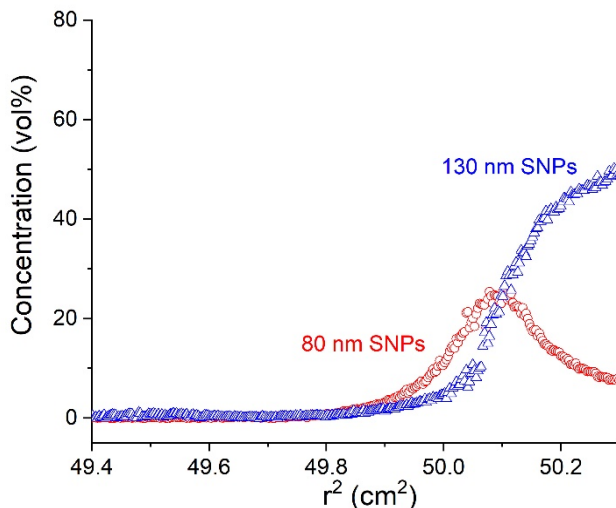


Figure S3: Experimental SDE profiles for the binary mixture of 80 nm Polyethylene glycol (PEG) stabilized RITC-SNPs and 130 nm PEG stabilized FITC-SNPs at an ionic strength of 0.1M at 1100 rpm and 25 °C (the molecular weight of PEG is 1000 Da). At this high ionic strength, particles behave nearly like hard spheres. The maximum concentration reaches 54 vol% (130 nm SNPs) + 8 vol% (80 nm SNPs) at the very bottom.

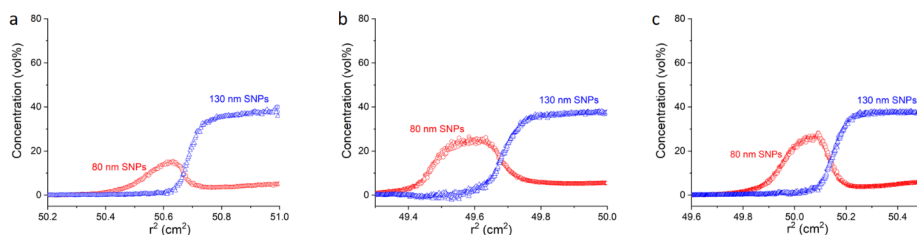


Figure S4: Experimental sedimentation-diffusion equilibrium (SDE) profiles for the binary mixture of 80 nm RITC-SNPs and 130 nm FITC-SNPs at 1100 rpm and 25 °C of a) a varied number ratio: $n(80 \text{ nm}) : n(130 \text{ nm}) = 1:2$; b) a larger sample volume: 20 ul and c) a slightly higher ionic strength 5mM.

Plot	r_L^2 (cm ²)	r_S^2 (cm ²)	P (cm ²)
a	50.69	50.54	0.15
b	49.67	49.47	0.20
c	49.96	50.15	0.19

Table S2: The calculated values of r_L^2 , r_S^2 and p for **Figure S4 a, b and c.**

Plot	r_L^2 (cm ²)	r_S^2 (cm ²)	P (cm ²)
experimental (80 nm+130 nm)	50.21	50.19	0.02
theoretical (80 nm +130 nm)	50.21	50.18	0.03
experimental (100 nm+130 nm)	50.30	50.23	0.07
theoretical (100 nm +130 nm)	50.29	50.22	0.07

Table S3: The calculated values of r_L^2 , r_S^2 and p for **Figure 4.3.**

Plot	r_L^2 (cm ²)	r_S^2 (cm ²)	P (cm ²)
experimental (0.001M HCl)	50.30	50.19	0.11
theoretical (0.001M HCl)	50.29	50.15	0.14
experimental (0.01M HCl)	50.32	50.24	0.08
theoretical (0.01M HCl)	50.25	50.16	0.09

Table S4: The calculated values of r_L^2 , r_S^2 and p for **Figure 4.4 a and b.**

SI 3: Experimental steps for the introduction of amino groups for 130 nm SNPs

In a typical reaction, 5 μ l (3-Aminopropyl) triethoxysilane (APTS) was diluted with 100 μ l Tetrahydrofuran (THF). The as-prepared APTS solution was added to 360 μ l PEG-stabilized 130 nm SNPs of ca. 6 mg/ml. The mixture was kept under 500 rpm stirring for 1.5 h. Then the dispersion was purified by the centrifugation for 3 times and re-dispersed in the solvents of varied acidities.

Aminopropyltriethoxysilane (purity \geq 99%) and Tetrahydrofuran were purchased from Sigma-Aldrich. All chemicals were used without any further purification.

Layering of bidisperse charged nanoparticles in sedimentation

Particles	Acidity (M HCl)	Zeta potential (mV)
80 nm s-SNPs	0.001	0
130 nm APTS-s-SNPs	0.001	+ 16
130 nm APTS-s-SNPs	0.01	+ 18

Table S5: The zeta potential measurements (by LitesizerTM 500) for 80 nm sterically stabilized silica nanoparticles (s-SNPs) and 130 nm APTS functionalized, sterically stabilized silica nanoparticles (APTS-s-SNPs) in different acidities, namely 0.01 M and 0.001 M HCl.

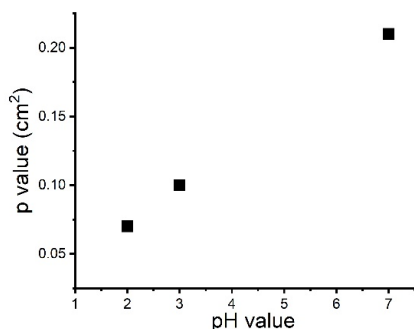


Figure S5: The change of the p values with the pH value of the suspension.

References

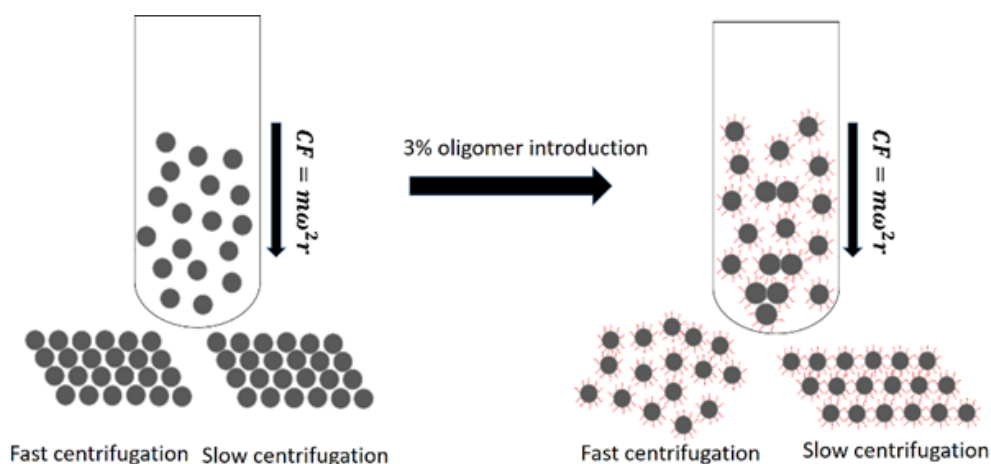
1. Chen, M.; Fischli, D.; Schertel, L.; Aubry, G. J.; Häusele, B.; Polarz, S.; Maret, G.; Cölfen, H., Free-standing photonic glasses fabricated in a centrifugal field. *Small* **2017**, *13* (34), 1701392.
2. Pearson, J.; Walter, J.; Peukert, W.; Cölfen, H., Advanced multiwavelength detection in analytical ultracentrifugation. *Analytical Chemistry* **2018**, *90* (2), 1280-1291.
3. Pearson, J.; Hofstetter, M.; Dekorsy, T.; Totzeck, M.; Cölfen, H., Design concepts in absorbance optical systems for analytical ultracentrifugation. *Analyst* **2018**, *143* (17), 4040-4050.
4. Karabudak, E.; Cölfen, H., The multiwavelength uv/vis detector: New possibilities with an added spectral dimension. In *Analytical ultracentrifugation: Instrumentation, software, and applications*, Uchiyama S., A. F., Stafford W., Laue T., Ed. Springer, Tokyo: 2016.
5. Spruijt, E.; Biesheuvel, P. M., Sedimentation dynamics and equilibrium profiles in multicomponent mixtures of colloidal particles. *Journal of Physics: Condensed Matter* **2014**, *26* (7), 075101.
6. Biesheuvel, P. M., Evidence for charge regulation in the sedimentation of charged colloids. *Journal of Physics: Condensed Matter* **2004**, *16* (49), L499-L504.

CHAPTER 5

7. Rasa, M.; Ern , B.; Zoetekouw, B.; van Roij, R.; Philipse, A., Macroscopic electric field and osmotic pressure in ultracentrifugal sedimentation–diffusion equilibria of charged colloids. *Journal of Physics: Condensed Matter* **2005**, *17* (15), 2293-2314.

CHAPTER 6

Superstructure Control for Monodisperse Nanoparticles with a Low Peclet Number in Ultracentrifugation



The results described in this chapter are based on:

Xufeng Xu, Baohu Wu, Helmut Cölfen* and Gijsbertus de With*. Superstructure control for monodisperse nanoparticles with a low Peclet number in ultracentrifugation. *Journal of Colloid and Interface Science* 2020, in revision.

6. Superstructure control for monodisperse nanoparticles with a low Peclet number in ultracentrifugation

The sedimentation of monodisperse colloidal nanoparticles is a quick and universal approach to form superstructure assemblies and fabricate macroscopic materials. However, so far it is still difficult to control the superstructure assembly after nanoparticle sedimentation due to their low Peclet number. More specifically, the intrinsic high diffusion rate results in an extremely fast crystallization process and instant formation of colloidal crystals even at an ultracentrifugal field of an extremely high angular velocity. Here we show that, by introducing a very small amount (as low as 3%) of oligomers (the term ‘oligomers’ are used as a jargon analogous to its use in polymer science) in the sedimentation process, the superstructure assembly becomes easily tunable between glass and crystal in ultracentrifugation. In this study sodium dodecyl sulfate stabilized polystyrene nanoparticles are dispersed in a solution of high ionic strength. The colloids stay well dispersed solely due to steric repulsion afforded by the surfactants. When these colloids sediment in an ultracentrifugal field, a tiny amount (3%) of oligomers forms, which is detected by analytical ultracentrifugation (AUC). The presence of these oligomers frustrates the fast crystallization process and the colloidal assembly ordering can then be easily tuned, by changing angular velocities. Therefore, this work provides a novel handle to fabricate superstructure assembly of tunable packing ordering for colloids with a low Peclet-number. This is achieved by introducing a very small amount (3%) of oligomers on purpose during sedimentation, in preparative ultracentrifugation.

6.1. Introduction

Colloidal particles are promising building blocks for the fabrication of micro-, meso- and macro-scale materials with controlled properties and functions.¹⁻² For example, colloidal particle based materials are widely used for carbon dioxide capture,³ as catalyst support⁴ and for fuel cell construction.⁵ Among these, the assembly of monodisperse colloidal particles⁶⁻⁷ represents the simplest case. There are currently a wide variety of bottom-up assembly methods available including controlled evaporation, vertical deposition, spin coating and so on.⁷⁻⁸ Among these methods, sedimentation induced assembly is a fast and versatile approach⁹⁻¹⁰ and the superstructure assembly is well described by the Peclet number (Pe)¹¹: A low value of Pe leads to a crystalline structure, while a high Pe value leads to a glassy one. In principle, the Peclet number is the ratio between the initial sedimentation rate ($\Delta\rho g^* a^2$) and the crystallization rate (kT/a^2), described in **Equation 6.1**:

$$Pe = \frac{\Delta\rho g^* a^4}{kT} \quad (6.1)$$

where $\Delta\rho$ is the density difference between the colloids and the solvent, g^* is the force due to the centrifugal field, a is the particle radius and kT is the thermal energy. As clear from **Equation (6.1)**, Pe is proportional to a^4 , which means the possibility of forming a glassy

Superstructure control for monodisperse nanoparticles with a low Peclet number in ultracentrifugation

structure is increasing rapidly with particle size. Accordingly, tuning of superstructure assembly was shown successful for micrometer-sized colloids.^{10, 12} However, for nano-size colloids, fast sedimentation was tested to be completely unsuccessful to realize a glassy structure¹³⁻¹⁴. As shown in **Figure 6.1A, B and C**, only a crystalline structure was formed even when Pe increased to 0.1 with a centrifugal field as strong as 153,900 g. The reason is that for monodisperse nanoparticles, the crystal nucleation and growth rate are much faster than the sedimentation rate during ultracentrifugation.¹⁵⁻¹⁶ In this paper we show that the assembly ordering for monodisperse colloidal particles can be simply controlled in an ultracentrifugal field. The strategy used is the introduction of a tiny amount (as low as 3%) of oligomers during the sedimentation process. The presence of this small amount of oligomers slightly increase the size polydispersity of the nanoparticles in dispersion, which in turn raises the crystal nucleation barrier significantly¹⁵. This leads to a delayed crystallization process¹⁷ which makes it possible for monodisperse colloids to form glassy superstructure in a strong centrifugal field. The method provides a novel way to control the assembly ordering for monodisperse nanoparticles.

6.2. Results and discussion

The dispersion of monodisperse polystyrene (PS) beads ($a = 50$ nm) was at first purified by dialysis and then mixed with a small amount of sodium dodecyl sulfate (SDS) (0.8 mM) to obtain sterically stabilized nanoparticles (the detailed preparation is described in **SI 1**). An extensive study¹⁸ of SDS adsorption on PS in water shows that the surface coverage can reach about 3 SDS/nm². As our conditions are rather similar to those used by Turner et al.¹⁸, a similar adsorption is present. To estimate the surface coverage, we use the data as given by Turner et al.¹⁸ Neutron reflection and infrared measurements were employed over a range of SDS concentrations using PS as a substrate in water. At the critical micelle concentration (cmc) of 8 mM, the area per SDS was estimated as 42 Å². Moreover, the surface coverage was given as 4.0 μmol/m² at the cmc and 1.7 μmol/m² at 0.8 mM. Hence in our case the surface coverage is $(4.0/1.7)42$ Å² or ca. 1 SDS per nm² (A similar estimation using the PS bead size and concentration, and assuming that all the SDS molecules adsorb on the PS surface results in the same value). In order to suppress the electrostatic repulsion between the negatively charged PS nanoparticles, the nanoparticles were dispersed in a high-ionic-strength buffer (0.1 M, the detailed composition is described in **SI 1**). In this case, these PS nanoparticles were solely stabilized by the surface bound surfactants. Dynamic light scattering (DLS), very-small angle neutron scattering (VSANS) (the detailed VSANS experiment is described in **SI 2**) and analytical ultracentrifugation (AUC) (as shown in **Figure S1 – S4**) all showed no aggregates present in the dispersion, due to the steric stabilization. In this way, sterically stabilized monodisperse PS nanoparticles with a polydispersity index as low as 0.07 were prepared for further use (detailed comparison of the polydispersity obtained from different techniques is discussed **SI 3**).

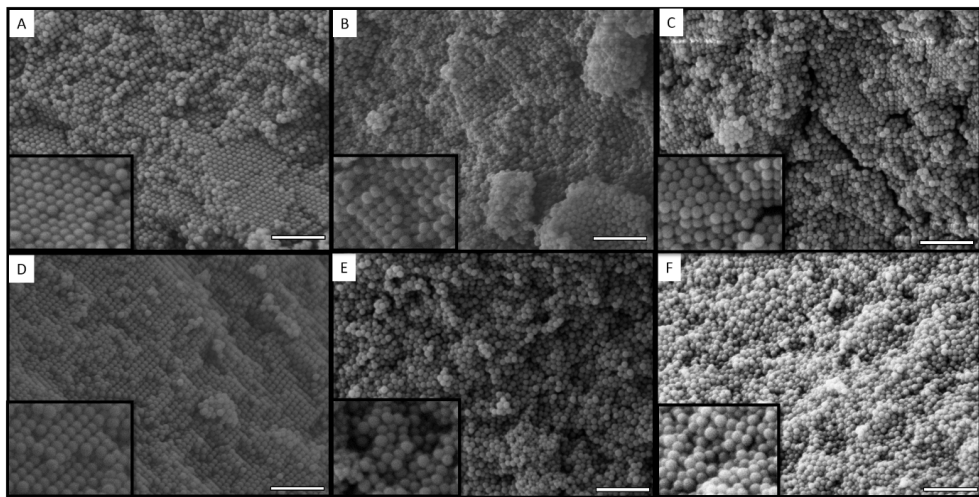


Figure 6.1: SEM images of colloidal assembly structures after complete sedimentation of charge stabilized PS nanoparticles in water at A 12,000 rpm (17,100 g), B 24,000 rpm (68,400 g) and C 36,000 rpm (153,900 g) and of SDS-stabilized PS nanoparticles in pH2 buffer at D 12,000 rpm (17,100 g), E 24,000 rpm (68,400 g) and F 36,000 rpm (153,900 g). The scale bar is 1 μm . The insets are magnified views of part of each image.

As can be seen from **Figure 6.1A to C**, charge stabilized PS nanoparticles were not sensitive to the angular velocity change at all and only the crystalline structures were formed (detailed sample preparation for SEM is described in **SI 4**). The reason is that the Pe value is still as low as 0.1 even when the angular velocity was increased to as high as 36,000 rpm (the force due to the centrifugal field $g^* \approx 153,900 g$ as the distance from the rotation center to the center of the sample is 105.5 mm using a SW-55 Ti rotor). In contrast, SDS-stabilized PS nanoparticles assembled into a crystalline structure at 12,000 rpm ($g^* \approx 17,100 g$), while they packed into a glassy structure at an angular velocity higher than 24,000 rpm ($g^* \geq 68,400 g$), as shown in **Figure 6.1D to F**. For the colloids of the same low Pe value, colloidal assembly ordering control is much more easily realized for surfactant stabilized colloids by tuning the sedimentation rate, while for charge stabilized colloids, ordering control is not possible in the same angular velocity range. In this case, analytical ultracentrifugation (AUC) mounted with Rayleigh interference optics was used to monitor the sedimentation process (we used the same initial volume fraction in the AUC and PUC experiments so that any effect due to the volume fraction is ruled out.) to reveal the mechanism for the assembly ordering control. **Figure 6.2A** shows that the sedimentation coefficient distribution of SDS-stabilized PS nanoparticles at 15,000 rpm ($g^* \approx 17,100 g$). It shows a pronounced ‘tailing’ in the higher s value end (s is sedimentation coefficient which is defined as the ratio of a particle's sedimentation velocity to the applied acceleration causing the sedimentation. The unit is in svedberg (S) and equals to 10^{-13} s). The tailing can be resolved into three oligomer peaks by using the diffusion corrected $c(s)$ model in the software Sedfit¹⁹. These three oligomers peaks are identified as the dimer, trimer linear and trimer triangular peaks respectively, according to their sedimentation coefficients²⁰⁻²¹, as shown in **Table 6.1**. Moreover, by integration of

Superstructure control for monodisperse nanoparticles with a low Peclet number in ultracentrifugation

these peaks, the fraction of oligomers consists of 3% of the sedimenting particles. In comparison, as shown in **Figure 6.2B**, the sedimentation coefficient distribution of charge stabilized PS nanoparticles shows no ‘tailing’ in the higher s value end and no oligomer peaks can be observed by using the $c(s)$ model. Overall, as VSANS experiments of the suspension showed no agglomeration (**SI 1**) and the AUC experiments indicated the presence of oligomers after sedimentation, we conclude that the oligomers with an amount of as small as 3% are most likely formed during the sedimentation process, which may disturb the whole crystallization process¹⁵. In this way, superstructure assembly ordering control can be achieved by playing with the angular velocity of the centrifugal field in a reachable range, from 12,000 rpm to 36,000 rpm.

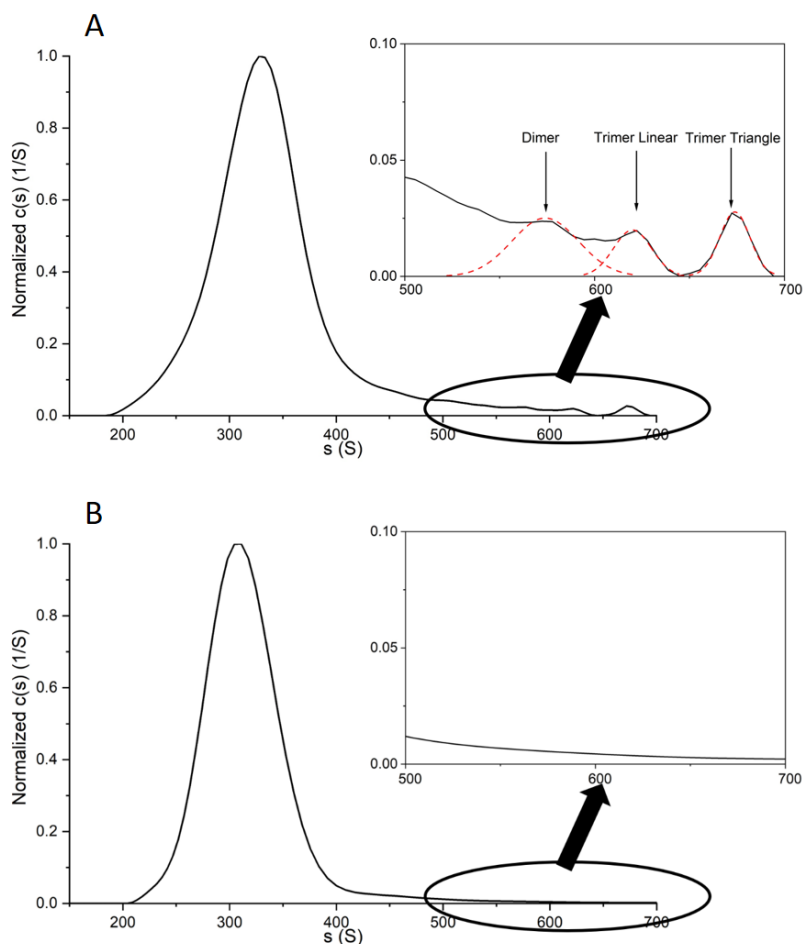


Figure 6.2: The sedimentation coefficient distribution using the $c(s)$ model with the software *Sedfit*¹⁹ of SDS-stabilized PS nanoparticles in pH2 buffer (A) and charge stabilized PS nanoparticles in water (B) of 1 wt% and at 15,000 rpm (17,100 g) by the AUC. The inlet

CHAPTER 6

figures zoom in the range from 500 S to 700 S and show whether there is the presence of oligomers. By the Gaussian fitting (red dashed curves) of the oligomer peaks, the amount of the oligomers was estimated to be ca. 3%.

Oligomer Peak	Monomer	Dimer	Trimer linear	Trimer triangle
s value (S)	335	570	620	670

Table 6.1: Sedimentation coefficients (*s* values) of the monomer and three different oligomers, obtained from **Figure 6.2A**.

The mechanism of the oligomer formation in the ultracentrifugal field is investigated by considering the interparticle interactions in a centrifugal field. The total interparticle potential of PS nanoparticles (U_{tot}) consists of the electrostatic repulsion (U_{R}) and the van der Waals attraction (U_{A}) according to the DLVO theory²². An additional repulsive steric potential U_{S} is also considered due to the presence of surface bound SDS chains. Therefore,

$$U_{\text{tot}} = U_{\text{R}} + U_{\text{A}} + U_{\text{S}} \quad (6.2)$$

U_{R} and U_{A} can be approximated by using **Equation 6.3** and **6.4** according to the DLVO theory²³:

$$U_{\text{R}} = 2\pi\epsilon_r\epsilon_0a\left(\frac{4kT}{ze}\tanh(ze\Psi_0/4kT)\right)^2\ln[1 + \exp(-\kappa H)] \quad (6.3)$$

and

$$U_{\text{A}} = -\frac{A}{6}\left(\frac{2r^2}{(2r+H)^2-4r^2} + \frac{2r^2}{(2r+H)^2} + \ln\frac{(2r+H)^2-4r^2}{(2r+H)^2}\right) \quad (6.4)$$

U_{S} can be estimated by using the Alexander-de Gennes polymer brush model²⁴⁻²⁶ which is applicable when $0 < H < 2L$:

$$U_{\text{S}} = \frac{16k_{\text{B}}T\pi aL^2\sigma^{\frac{3}{2}}}{35}\left[28\left(\left(\frac{2L}{H}\right)^{\frac{1}{4}} - 1\right) + \frac{20}{11}\left(1 - \left(\frac{H}{2L}\right)^{\frac{11}{4}}\right) + 12\left(\frac{H}{2L} - 1\right)\right] \quad (6.5)$$

Here ϵ_r is the relative permittivity, ϵ_0 is the vacuum permittivity, a is the particle radius, Ψ_0 is the surface potential (approximated by zeta potential ζ), κ is the reciprocal Debye length, H is the interparticle distance, z is the valency, e is the unit charge, A is the Hamaker constant, σ is the surfactant density on the particle surface, and L is the surfactant chain length.

For PS nanoparticles in water, $\kappa a = 5.2$ and $\Psi_0 \approx \zeta = -40$ mV and in pH2 buffer, $\kappa a = 45$ and $\Psi_0 \approx \zeta = -5$ mV; The SDS chain length is ca. 1.2 nm¹⁸ and the surface coverage is ca. 1 SDS per nm². Given that, the total interparticle potential (U_{tot}) for PS nanoparticles in water and in pH2 buffer was plotted separately, as shown in **Figure 6.3A** and **3B**, respectively. The energy barrier for the coagulation of PS nanoparticles in water is ca. 40 kT , which agrees with its very good stability and no aggregation, indicated in **Figure 6.2B**. The conventional DLVO

Superstructure control for monodisperse nanoparticles with a low Peclet number in ultracentrifugation

theory can result in a potential curve with a maximum and a secondary minimum. However, calculating the DLVO curve for PS nanoparticles in pH2 buffer resulted in a curve showing no maximum and hence no barrier to agglomeration is present, as shown in the red curve in **Figure 6.3B**. Adding SDS resulted in steric stabilization and thus the energy barrier of ca. 6 kT appeared, as indicated by the black curve in **Figure 6.3B**. Thus, the dispersion remains monodisperse without any external field (**Figure S1-4**). However, in a strong centrifugal field, a small amount of oligomers was formed, as shown in **Figure 6.2A**. The contributing force to overcome the barrier of 6 kT might arise from two sources. Firstly, the centrifugal force (F) exerted on a single nanoparticle can be calculated using **Equation 6.6**.

$$F = \frac{4}{3} \pi a^3 (\rho_p - \rho_s) g^* \quad (6.6)$$

where a is the particle radius, ρ_p and ρ_s is the density of particles and solvent, respectively, and g^* is the force due to the centrifugal field.

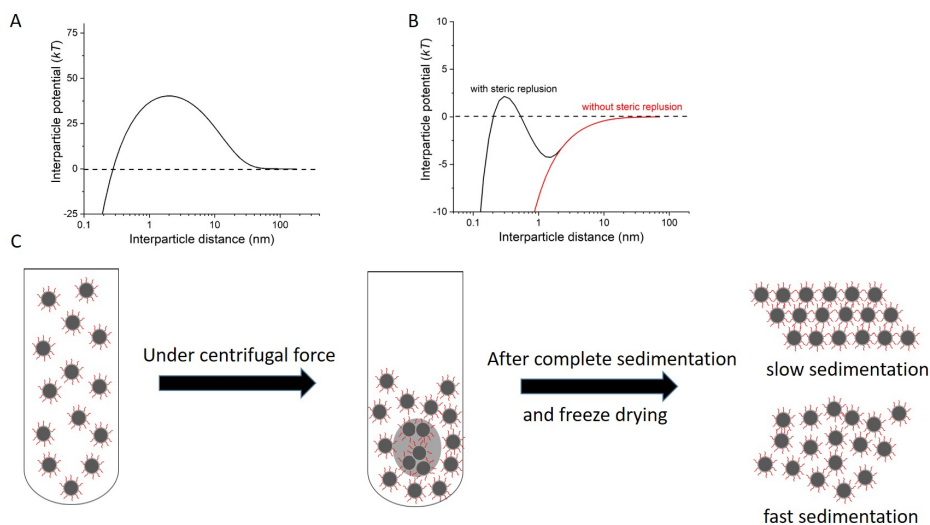


Figure 6.3: Total interparticle potential of PS nanoparticles in water (A) and in pH2 buffer (B). C. The proposed mechanism behind colloidal assembly order tuning in preparative ultracentrifugation. The red hairs on the surface of particles indicate the surfactant SDS. Under a sufficiently high centrifugal force, a small number of oligomers is formed (highlighted by a grey shade inside the tube). These oligomers disturb the crystallization process and make the assembly superstructure tunable with the angular velocity: for slow sedimentation, a crystalline structure is formed, while for fast sedimentation a glassy structure is formed.

For a PS nanoparticle with radius 50 nm and density 1.06 $\text{g}\cdot\text{cm}^{-3}$ in water (1.00 $\text{g}\cdot\text{cm}^{-3}$) under a centrifugal field at 17,100 g , the centrifugal force is approximately 5×10^{-15} N. As discussed in the work by van der Linden et al²⁷, this force may be strong enough to push some

particles through the steric stabilizing layer, especially when the settling nanoparticles are concentrated and move close together in the confinement of a centrifuge tube. The other force may come from hydrodynamic interaction. As Folkersma et al.²⁸ and Xu et al.²⁹ discussed, hydrodynamic attraction may appear when the particle concentration increases and interparticle distance becomes small. This hydrodynamic effect can also lead to the formation of oligomers. Overall, with these two effects the thus proposed mechanism is plotted schematically in **Figure 6.3C**.

6.3. Conclusion

In summary, colloidal assembly ordering for monodisperse nanoparticles of a low Peclet number can be controlled in ultracentrifugation by simply adjusting the angular velocity. This implies that both ordered and disordered superstructures can be easily obtained by a fast sedimentation method³⁰. The mechanism behind this is the introduction of a tiny amount of oligomers (as low as 3%) during the sedimentation. The presence of this small amount of oligomers slows down the crystallization rate to a level with which the sedimentation rate can compete. In this way the assembly structure can be simply tuned by changing the angular velocity of the ultracentrifugation experiment. Overall, this work provides an easy and versatile approach to construct both crystalline and glassy superstructures from monodisperse colloids of a low Peclet number, which have a wide application in areas, such as quantum electronics, battery and photonic materials.

6.4. References

1. Lu, Z.; Yin, Y., Colloidal nanoparticle clusters: Functional materials by design. *Chemical Society Reviews* **2012**, *41* (21), 6874-6887.
2. Ciesla, U.; Schüth, F., Ordered mesoporous materials. *Microporous and Mesoporous Materials* **1999**, *27* (2), 131-149.
3. Yang, H.; Xu, Z.; Fan, M.; Gupta, R.; Slimane, R. B.; Bland, A. E.; Wright, I., Progress in carbon dioxide separation and capture: A review. *Journal of Environmental Sciences* **2008**, *20* (1), 14-27.
4. Huh, S.; Chen, H.-T.; Wiench, J. W.; Pruski, M.; Lin, V. S. Y., Cooperative catalysis by general acid and base bifunctionalized mesoporous silica nanospheres. *Angewandte Chemie International Edition* **2005**, *44* (12), 1826-1830.
5. Lu, S.; Wang, D.; Jiang, S. P.; Xiang, Y.; Lu, J.; Zeng, J., Hpw/mcm-41 phosphotungstic acid/mesoporous silica composites as novel proton-exchange membranes for elevated-temperature fuel cells. *Advanced Materials* **2010**, *22* (9), 971-976.
6. Murray, C. B.; Kagan, A. C.; Bawendi, M., Synthesis and characterization of monodisperse nanocrystals and close-packed nanocrystal assemblies. *Annual Review of Materials Science* **2000**, *30* (1), 545-610.
7. Boles, M. A.; Engel, M.; Talapin, D. V., Self-assembly of colloidal nanocrystals: From intricate structures to functional materials. *Chemical Reviews* **2016**, *116* (18), 11220-89.
8. Vogel, N.; Retsch, M.; Fustin, C.-A.; del Campo, A.; Jonas, U., Advances in colloidal assembly: The design of structure and hierarchy in two and three dimensions. *Chemical Reviews* **2015**, *115* (13), 6265-6311.

Superstructure control for monodisperse nanoparticles with a low Peclet number in ultracentrifugation

9. Chen, M.; Cölfen, H.; Polarz, S., Centrifugal field-induced colloidal assembly: From chaos to order. *ACS Nano* **2015**, *9* (7), 6944-50.
10. Davis, K. E.; Russel, W. B.; Glantschnig, W. J., Disorder-to-order transition in settling suspensions of colloidal silica: X-ray measurements. *Science* **1989**, *245* (4917), 507-510.
11. Whitmer, J. K.; Luijten, E., Sedimentation of aggregating colloids. *The Journal of Chemical Physics* **2011**, *134* (3), 034510.
12. Van Blaaderen, A.; Wiltzius, P., Real-space structure of colloidal hard-sphere glasses. *Science* **1995**, *270* (5239), 1177-1179.
13. García, P. D.; Sapienza, R.; Blanco, Á.; López, C., Photonic glass: A novel random material for light. *Advanced Materials* **2007**, *19* (18), 2597-2602.
14. García, P. D.; Sapienza, R.; López, C., Photonic glasses: A step beyond white paint. *Advanced Materials* **2010**, *22* (1), 12-19.
15. Auer, S.; Frenkel, D., Suppression of crystal nucleation in polydisperse colloids due to increase of the surface free energy. *Nature* **2001**, *413* (6857), 711.
16. Royall, C. P.; Vermolen, E. C.; van Blaaderen, A.; Tanaka, H., Controlling competition between crystallization and glass formation in binary colloids with an external field. *Journal of Physics: Condensed Matter* **2008**, *20* (40), 404225.
17. Schöpe, H. J.; Bryant, G.; Megen, W. v., Effect of polydispersity on the crystallization kinetics of suspensions of colloidal hard spheres when approaching the glass transition. *The Journal of Chemical Physics* **2007**, *127* (8), 084505.
18. Turner, S. F.; Clarke, S. M.; Rennie, A. R.; Thirtle, P. N.; Cooke, D. J.; Li, Z. X.; Thomas, R. K., Adsorption of sodium dodecyl sulfate to a polystyrene/water interface studied by neutron reflection and attenuated total reflection infrared spectroscopy. *Langmuir* **1999**, *15* (4), 1017-1023.
19. Schuck, P., Size-distribution analysis of macromolecules by sedimentation velocity ultracentrifugation and lamm equation modeling. *Biophysical Journal* **2000**, *78* (3), 1606-19.
20. Nieduszynski, I., Dynamic properties of biomolecular assemblies: Edited by se harding and aj rowe, royal society of chemistry, cambridge, 1989, pp. 374. Elsevier: 1990.
21. Chen, M.; Fischli, D.; Schertel, L.; Aubry, G. J.; Häusele, B.; Polarz, S.; Maret, G.; Cölfen, H., Free-standing photonic glasses fabricated in a centrifugal field. *Small* **2017**, *13* (34), 1701392.
22. I. Hogg, R.; W. Healy, T.; W. Fuerstenau, D., *Mutual coagulation of colloid dispersions*. 1966; Vol. 62.
23. Physical - chemical aspects. *Polymer coatings*, With, G. d., Ed. Wiley - VCH Verlag GmbH & Co. KGaA: 2018.
24. Alexander, S., Polymer adsorption on small spheres. A scaling approach. *Journal de physique* **1977**, *38* (8), 977-981.
25. De Gennes, P.-G., Stabilité de films polymère/solvant. *Comptes rendus de l'Académie des sciences. Série 2, Mécanique, Physique, Chimie, Sciences de l'univers, Sciences de la Terre* **1985**, *300* (17), 839-843.
26. Kleshchanok, D.; Tuinier, R.; Lang, P. R., Direct measurements of polymer-induced forces. *Journal of Physics: Condensed Matter* **2008**, *20* (7), 073101.

CHAPTER 6

27. Van der Linden, M. N.; El Masri, D.; Dijkstra, M.; van Blaaderen, A., Expansion of charged colloids after centrifugation: Formation and crystallisation of long-range repulsive glasses. *Soft Matter* **2013**, *9* (48), 11618-11633.
28. Folkersma, R.; Stein, H.; Van de Vosse, F., Hydrodynamic interactions between two identical spheres held fixed side by side against a uniform stream directed perpendicular to the line connecting the spheres' centres. *International Journal of Multiphase Flow* **2000**, *26* (5), 877-887.
29. Xu, W.; Nikolov, A.; Wasan, D. T., The effect of many-body interactions on the sedimentation of monodisperse particle dispersions. *Journal of Colloid and Interface Science* **1998**, *197* (1), 160-169.
30. Pusey, P. N.; van Megen, W., Observation of a glass transition in suspensions of spherical colloidal particles. *Physical Review Letters* **1987**, *59* (18), 2083-2086.

6.5. Appendix

SI 1: Preparation of sterically stabilized polystyrene nanoparticles

10 vol% stock polystyrene (PS) bead suspension (radius 49.8 nm, polydispersity 0.07 as obtained by measuring 100 nanoparticles from a scanning electron microscopy (SEM) image) was bought from Sigma-Aldrich. The suspension was purified by dialysis against MilliQ water for several days until the conductivity of the dialysis water did not change. An appropriate amount of sodium dodecyl sulfate (SDS) was dissolved in the PS suspension to obtain the final concentration of 0.8 mM. The suspension was then diluted 10 times by pH2 buffer (0.08 M KCl and 0.02 M HCl mixture) to make the 1 vol% PS suspension for the further use. The suspension was diluted sufficiently to an appropriate concentration. The zeta potential measurements were then conducted using the Malvern Zetasizer Nano ZSP: the conversion from electrophoretic mobility to zeta potential was achieved by using Henry Equation. The smoluchowski approximation was implemented because it is suitable for samples suspended in aqueous solutions.

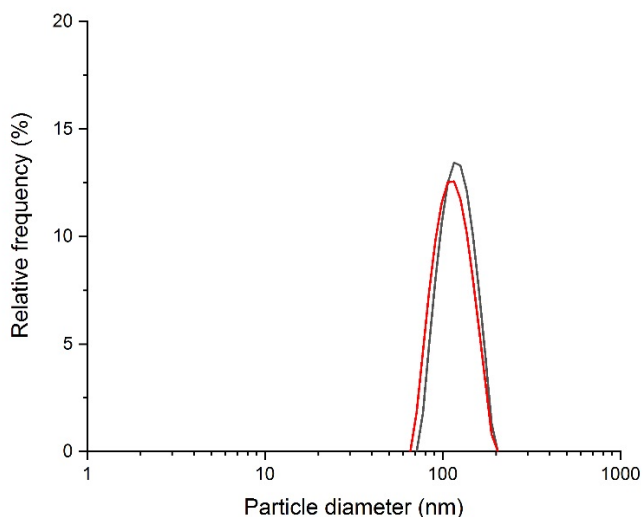


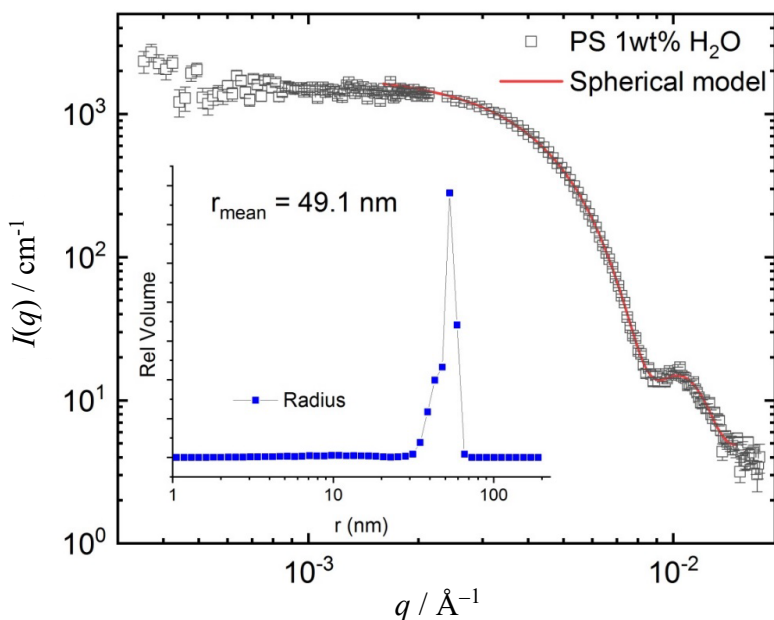
Figure S1: The size distribution of the SDS-stabilized PS nanoparticles in water (black) and in pH2 buffer (red) by LitesizerTM 500. The analytical model used is Contin and the cumulate model used is ISO 22412. The hydrodynamic radius for SDS-stabilized PS nanoparticles in water is 117 nm (PI: 2.2%) while that in pH2 buffer is 112 nm (PI: 1.6%). The size distributions largely overlap and the low PI values (< 10%) in the both cases indicate the high monodispersity of SDS-stabilized PS nanoparticles both in water and in a pH2 buffer.

SI 2: Very small angle neutron scattering (VSANS) experiments

Very small angle neutron scattering experiments were carried out at the KWS-3 diffractometer (Garching, Munich) using a parabolic mirror as an optical element. Using a neutron wavelength of 12.8 Å with $\Delta\lambda/\lambda = 17\%$ and a sample to detector distance of 9.5 m and 1.3, a q -range from about 0.0001 to 0.02 Å⁻¹ was covered. The scattered intensity was collected using a ⁶Li-scintillation detector with pixel size of 0.116 × 0.116 mm², size 3 × 3 cm². The data correction and calibration were performed using the software QtiKWS. VSANS results (**Figure S2** and **S3**) were analyzed by using a Monte Carlo method in order to get information on the size distribution of the particles. Monte-Carlo data fitting was performed using the McSAS analysis packages as described by Bressler et al.¹. The method starts from a set of non-interacting spherical particles but with random values chosen for the fitting parameter(s) of each contribution in the set. The total model scattering pattern is given by the (weighted) sum of the scattering patterns of each scatterer in the set and is compared to the experimental curve. Quantitatively speaking, the VSANS pattern is simulated by a sphere form factor $P(q)$, shown in **Equation S1** and compared to the experimental curve.

$$P(q) = \frac{S}{V} \left(\frac{3V\Delta\rho(\sin(qr) - qr \cos(qr))}{qr^3} \right)^2 + B \quad (S1)$$

where r is the radius of the sphere, S is the scale factor, V is the volume of the sphere. Scattering contrast ($\Delta\rho$) = SLD (sphere) – SLD (solvent) (SLD is Scattering Length Density). The B is the incoherent background and the returned value is scaled to units of [cm⁻¹].



Superstructure control for monodisperse nanoparticles with a low Peclet number in ultracentrifugation

Figure S2: VSANS scattering intensity $I(q)$ versus q plots of SDS-stabilized PS nanoparticles in H_2O . The red dashed line is a Monte Carlo simulation result by using a spherical model. The inset shows the corresponding particle size distribution.

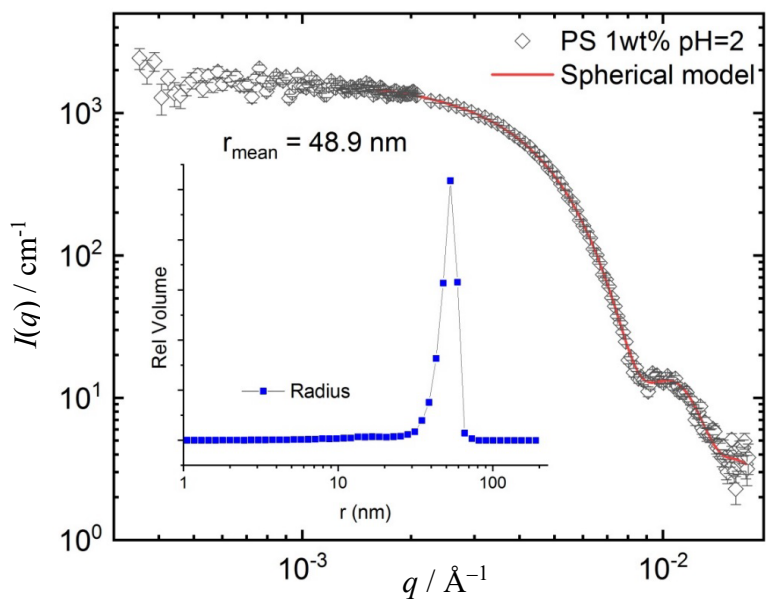


Figure S3: VSANS scattering intensity $I(q)$ versus q plots of SDS-stabilized PS nanoparticles in pH2 buffer. The red dashed line is a Monte Carlo simulation result by using a spherical model. The inset shows the corresponding particle size distribution.

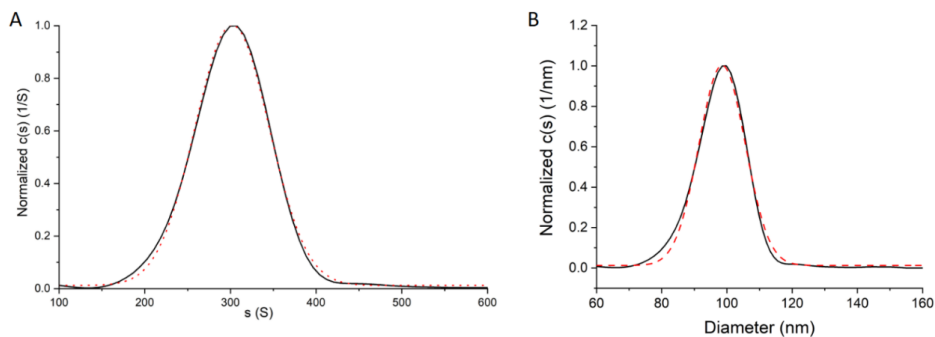


Figure S4: A) The sedimentation coefficient distribution using the $c(s)$ model (black curve) with the software Sedfit for SDS-stabilized PS nanoparticles in pH2 buffer (1 wt%) at a very low angular velocity (5000 rpm, 1900 g) by the AUC. The red curve is the Gaussian function fitting curve and the agreement shows the particle size monodispersity in the dispersion; B) The particle size distribution (black curve) calculated from the sedimentation coefficient distribution. By using the Gaussian function fitting (red curve), the size polydispersity can be calculated: 0.07, while by using the raw data (without any fitting) the polydispersity is 0.08.

SI 3: Discussion on the polydispersity obtained from the different techniques

The size distribution was firstly evaluated by SEM. By using SEM to observe and measure the diameters of 100 PS nanoparticles, a number weighted size distribution with an average diameter of 99.5 nm was obtained. By applying the classic definition of polydispersity² $\delta = \sqrt{\langle \Delta R^2 \rangle} / \langle R \rangle$, a value of $\delta = 0.07$ resulted. The second method that we relied on is AUC. As **Figure S4** shows, a Gaussian function fitted the size distribution well and resulted in an average particle diameter of 99.8 nm and the polydispersity was estimated from the full width at half maximum of the peak, resulting in 0.07. More strictly, the polydispersity was also estimated using the raw data in **Figure S4** without any fitting, resulting in a value of 0.08 which is only slightly larger than the value from the Gaussian function fitting. The last technique that we used is DLS, where the polydispersity is normally characterized by PI (polydispersity index) values. These PI values are specific for DLS measurements³ and the definition is not the same as the classic definition of polydispersity, but obtained by the cumulant analysis (and fitting the autocorrelation function). The PI values that we obtained (ca. 2%) are below 10%, a typical threshold value for small polydispersity in a DLS measurement. From typical DLS measurement data, the number weighted particle size distribution can be calculated from the experimentally obtained intensity weighted distribution, based on the assumption that the intensity (I) is proportional to the diameter (d) to the 6th power⁴. Thus, we can compare the number weighted particle size distributions from SEM and DLS, as shown in **Figure S5**. We find an overall agreement but the location of the peak is at a slightly smaller value and the width of the peak is somewhat larger for the size distribution from DLS than from SEM. Frequently, size measured by DLS shows a somewhat larger value than as measured by the microscopy and this typically attributed to agglomeration and/or aggregation or the presence of surfactants⁵. In a few cases, like here, the reverse is observed for which the reason is not quite clear, but sometimes attributed to the presence of permeable gel layer around particle⁶. Generally, a comparison of the results of these methods is not straightforward at all⁷⁻⁹. When discussing the packing of particles in a sediment, a number weighted particle size distribution should be used. These distributions are obtained directly and reliably from SEM and AUC, while DLS requires additional data, such as refractive index and density, and involves more instrumental and converting issues. Overall, for the present results, the size and polydispersity obtained from SEM and AUC (as well as neutron scattering in **SI 2**) agree well, while the PI values and the number distribution from DLS measurements also show small polydispersity.

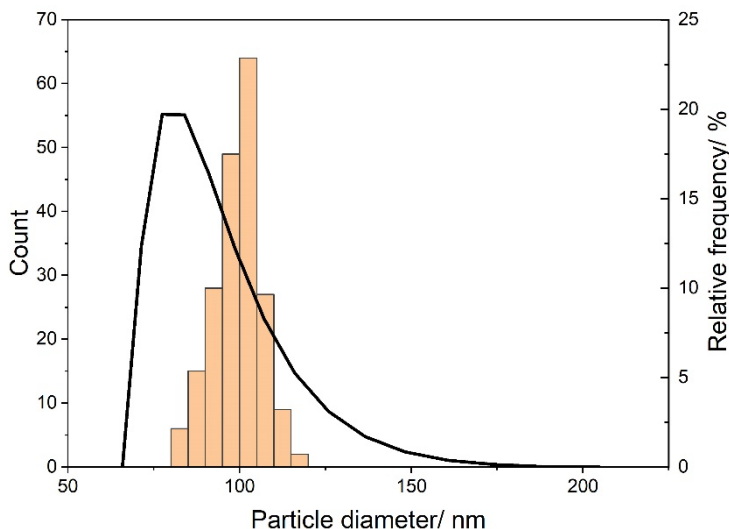


Figure S5: The number weighted particle size distribution from SEM, shown as a histogram, and from DLS, shown as a curve.

SI 4: Detailed sample preparation for SEM characterization

After the ultracentrifugation experiment, the sediment was firstly freeze-dried (typically 1-2 days). After that, the dried sample was chopped into pieces by a razor blade before loading on a SEM stub for the SEM characterization. By this means, the nanoparticle packing inside the sediment can be observed well.

References

1. Breßler, I.; Pauw, B. R.; Thünemann, A. F., Mcsas: Software for the retrieval of model parameter distributions from scattering patterns. *Journal of Applied Crystallography* **2015**, 48 (3), 962-969.
2. Desmond, K. W.; Weeks, E. R., Influence of particle size distribution on random close packing of spheres. *Physical Review E* **2014**, 90 (2), 022204.
3. Gaumet, M.; Vargas, A.; Gurny, R.; Delie, F., Nanoparticles for drug delivery: The need for precision in reporting particle size parameters. *European Journal of Pharmaceutics and Biopharmaceutics* **2008**, 69 (1), 1-9.
4. Wishard, A.; Gibb, B. C., Dynamic light scattering—an all-purpose guide for the supramolecular chemist. *Supramolecular Chemistry* **2019**, 31 (9), 608-615.
5. Souza, T. G.; Ciminelli, V. S.; Mohallem, N. D. S. In A comparison of tem and dls methods to characterize size distribution of ceramic nanoparticles, *Journal of Physics: Conference Series*, IOP Publishing: **2016**; p 012039.
6. Tuoriniemi, J.; Johnsson, A.-C. J.; Holmberg, J. P.; Gustafsson, S.; Gallego-Urrea, J. A.; Olsson, E.; Pettersson, J. B.; Hassellöv, M., Intermethod comparison of the

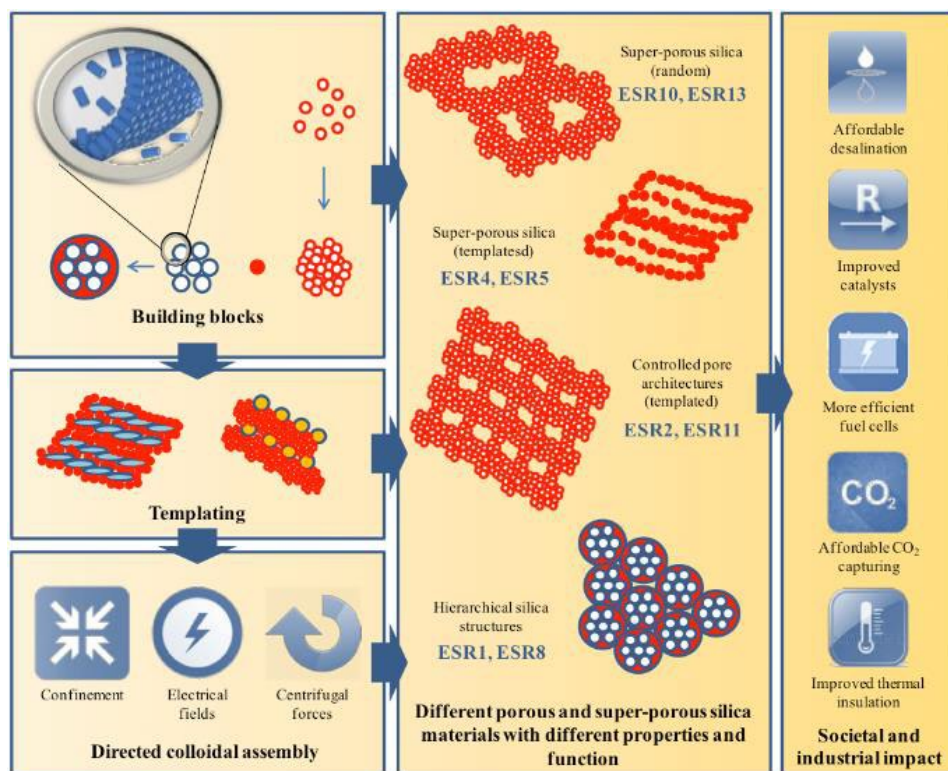
CHAPTER 6

particle size distributions of colloidal silica nanoparticles. *Science and Technology of Advanced Materials* **2014**, 15 (3), 035009.

7. Eaton, P.; Quaresma, P.; Soares, C.; Neves, C.; de Almeida, M. P.; Pereira, E.; West, P., A direct comparison of experimental methods to measure dimensions of synthetic nanoparticles. *Ultramicroscopy* **2017**, 182, 179-190.
8. Amini, R.; Brar, S. K.; Cledon, M.; Surampalli, R. Y., Intertechnique comparisons for nanoparticle size measurements and shape distribution. *Journal of Hazardous, Toxic, and Radioactive Waste* **2016**, 20 (1), B4015004.
9. Bootz, A.; Vogel, V.; Schubert, D.; Kreuter, J., Comparison of scanning electron microscopy, dynamic light scattering and analytical ultracentrifugation for the sizing of poly (butyl cyanoacrylate) nanoparticles. *European Journal of Pharmaceutics and Biopharmaceutics* **2004**, 57 (2), 369-375

CHAPTER 7

Conclusion and Outlook



This chapter is based on:

Xufeng Xu, Helmut Cölfen*. Ordering of nanoparticles in a centrifugal field.
Nanomaterials 2020, to be submitted (invited review)

7. Conclusion and outlook

7.1. Conclusion

The sedimentation of colloidal microbeads¹⁻² in gravity already saw many theoretical and experimental advances in the last century. Besides to the establishment of fundamental theories of sedimentation³⁻⁵, experimental research also saw major progress⁶⁻¹⁰, especially a series of classic experiments conducted by Pusey and Meegen. They made it possible to synthesize hard sphere like latex particles, which represents the simplest interparticle interaction¹¹ case. The phase transition process of these microbeads under gravity was *in-situ* observed and analysed. With the emergence of nanotechnology¹²⁻¹³, colloidal nanoparticles in sedimentation also attract a great deal of attention, which, however, requires the employment of a centrifugal field due to their intrinsically small size¹⁴. Especially when colloidal particles become concentrated in a centrifugal field, the understanding of their physicochemical behaviour is rather important since it is not only relevant for the industry, as processes using such dispersions are abundant, but also vital in academia, since interparticle interaction at such high concentration is largely unexplored. Therefore, my thesis focused on concentrated colloids in a centrifugal field.

The story begins with the simplest case: colloids only working with hard sphere like interaction. The concentration gradients of both monodisperse and bidisperse colloidal particles can be simulated and in practical tailor-made in a centrifugal field with the pre-knowledge of sedimentation and diffusion properties of these particles. A continuous particle concentration ratio gradient can be thus accessed in one single preparative ultracentrifugation experiment to obtain an extended phase diagram of binary superstructures in one centrifuge tube. Unexpectedly, we also found that when the size ratio of a binary hard sphere mixture becomes large, the smaller particles can be even levitated in a centrifugal field. This phenomenon can be quantitatively explained by the theory of effective buoyancy, which provides a good model to study the layering of sedimenting polydisperse colloidal particles in natural and industrial cases.

The story becomes even more exciting when colloidal particles carry charge. With the presence of a sea of ‘extremely light’ counter ions, the classic Donnan potential is formed in a centrifugal field. The sedimentation-diffusion equilibrium for colloids can be experimentally reached with a concentration up to 60 vol%. Rather surprisingly, it was observed that like-charged repulsive colloidal particles started to attract each other at very high concentration regime. This interparticle attraction can be uncovered at 1) the molecular scale (particle-surface deprotonated hydroxide groups), 2) the colloidal scale (particle concentration gradient) and 3) the macroscopic scale (gel formation). In Chapter 5, the ordering of bidisperse charged particles in a centrifugal field was carefully studied both experimentally and theoretically. A binary mixture of charged colloids becomes layered in sedimentation-diffusion equilibrium as a result of minimization of the system Gibbs free energy. We investigated different parameters that might affect the layering, supported by the theoretical calculations of the full sedimentation profiles. Counterintuitively, we found that lighter particles can even sink below heavier ones when the particle surface charge is

carefully tuned. In the future, this study might give some hints to the purification of polydisperse particles based on the pure thermodynamic driving force.

The final part of the story discusses the superstructure control for colloidal particles of a low Peclet number in the centrifugation. Especially for nanoparticles, their intrinsic high diffusion rate induces the instant formation of colloidal crystals, even at a centrifugal field of an extremely high angular velocity. In our study, we discovered that a tiny amount of oligomers can be detected in sedimentation and proven to significantly affect the final assembly structure, making colloidal glass possible and superstructure ordering tuneable.

Overall, we use fluorescent labeled silica nanoparticles at high initial concentration in a refractive index matching solvent (the turbidity caused by light scattering, irrespective of the size can be significantly minimized) as a model system. With the help of a most powerful available quantitative technique, namely analytical ultracentrifugation, mounted with a multiwavelength detector, the mysteries of colloids at high concentration can be carefully studied in a centrifugal field.

7.2. Outlook

As far as we realize, the research on concentrated colloids in a centrifugal field is still in its infancy. The field will develop significantly if the two main issues are tackled: 1) software development to make tailor-made concentration gradients more convenient to design, with the combinational use of analytical and preparative (ultra)centrifugation; 2) methodology development to allow the measurement of concentration gradients in centrifugation without the pre-requirement of a refractive index matching solvent and fluorescent labeling, especially at high concentration. This will certainly improve the application extensiveness to all kinds of colloidal particles and even to polymers¹⁵ and metal-organic framework¹⁶, besides to well-studied silica and latex particles. Therefore, we expect to see more research output in this interdisciplinary field between colloidal science and centrifugation technique in the future, especially for the applications in photonic materials¹⁷⁻¹⁸, porous materials¹⁹ and functional gradient materials²⁰.

7.3. References

1. Russel, W. B.; Russel, W.; Saville, D. A.; Schowalter, W. R., *Colloidal dispersions*. Cambridge university press: 1991.
2. Ghosh, P., *Colloid and Interface Science*. PHI Learning Pvt. Ltd.: 2009.
3. Kynch, G. J., A theory of sedimentation. *Transactions of the Faraday society* **1952**, *48*, 166-176.
4. Batchelor, G. K., Sedimentation in a dilute dispersion of spheres. *Journal of Fluid Mechanics* **1972**, *52* (2), 245-268.
5. Vrij, A., Sedimentation equilibrium in concentrated, multicomponent particle dispersions. Hard spheres in the percus–yevick approximation. *The Journal of Chemical Physics* **1980**, *72* (6), 3735-3739.
6. Pusey, P. N.; Van Megen, W., Phase behaviour of concentrated suspensions of nearly hard colloidal spheres. *Nature* **1986**, *320* (6060), 340-342.
7. Pusey, P. N.; van Megen, W., Observation of a glass transition in suspensions of spherical colloidal particles. *Physical Review Letters* **1987**, *59* (18), 2083.

CHAPTER 7

8. Pusey, P. N.; van Megen, W.; Bartlett, P.; Ackerson, B. J.; Rarity, J. G.; Underwood, S. M., Structure of crystals of hard colloidal spheres. *Physical Review Letters* **1989**, *63* (25), 2753-2756.
9. Hachisu, S.; Takano, K., Pressure of disorder to order transition in monodisperse latex. *Advances in Colloid and Interface Science* **1982**, *16* (1), 233-252.
10. Kose, A.; Ozaki, M.; Takano, K.; Kobayashi, Y.; Hachisu, S., Direct observation of ordered latex suspension by metallurgical microscope. *Journal of Colloid and Interface Science* **1973**, *44* (2), 330-338.
11. Israelachvili, J. N., *Intermolecular and surface forces*. Academic press: 2015.
12. Murty, B.; Shankar, P.; Raj, B.; Rath, B.; Murday, J., *Textbook of nanoscience and nanotechnology*. Springer Science & Business Media: 2013.
13. Kuno, M., Introductory nanoscience: Physical and chemical concepts. *MRS Bulletin* **2012**, *37* (2), 169-170.
14. Regel, L. L.; Wilcox, W. R., Centrifugal materials processing. In *Centrifugal materials processing*, Springer: 1997; pp 1-15.
15. Spinnrock, A.; Cölfen, H., Control of molar mass distribution by polymerization in the analytical ultracentrifuge. *Angewandte Chemie International Edition* **2018**, *57* (27), 8284-8287.
16. Park, J. H.; Paczesny, J.; Kim, N.; Grzybowski, B., Shaping microcrystals of metal-organic frameworks by reaction-diffusion. *Angewandte Chemie International Edition n/a* (n/a).
17. García, P. D.; Sapienza, R.; Blanco, Á.; López, C., Photonic glass: A novel random material for light. *Advanced Materials* **2007**, *19* (18), 2597-2602.
18. Joannopoulos, J. D.; Villeneuve, P. R.; Fan, S., Photonic crystals: Putting a new twist on light. *Nature* **1997**, *386*, 143.
19. Cecilia, J. A.; Moreno Tost, R.; Retuerto Millán, M., Mesoporous materials: From synthesis to applications. *International Journal of Molecular Sciences* **2019**, *20* (13), 3213.
20. Kieback, B.; Neubrand, A.; Riedel, H., Processing techniques for functionally graded materials. *Materials Science and Engineering: A* **2003**, *362* (1-2), 81-106.

List of important symbols and abbreviations

a	particle radius (m)
d	particle diameter (m)
D	diffusion coefficient ($\text{m}^2 \cdot \text{s}^{-1}$)
k_s, k_D	nonideality coefficient
k (k_B)	Boltzmann's constant ($\text{J} \cdot \text{K}^{-1}$)
L_ω	centrifugal length (m)
M	molecular mass ($\text{kg} \cdot \text{mol}^{-1}$)
n	refractive index
r	radial position (m)
s	sedimentation coefficient (S)
Z	charge number
ω	angular velocity (rpm)
v_{bar}	partial specific volume ($\text{m}^3 \cdot \text{kg}^{-1}$)
AUC	analytical ultracentrifuge
AUC-SE	sedimentation equilibrium experiment
AUC-SV	sedimentation velocity experiment
APTES	3-aminopropyltriethoxy-silane
CLSM	confocal laser scanning microscopy
DLVO	Derjaguin-Landau-Verwey-Overbeek
FITC	fluorescein isothiocyanate
MWL	multi-wavelength
PDI	polydispersity
PEG	polyethylene glycol
PUC	preparative ultracentrifuge
PS	polystyrene
RMSD	root-mean-square deviation
RITC	rhodamine isothiocyanate
SD	sedimentation-diffusion
SEM	scanning electron microscopy
SNPs	silica nanoparticles
TEOS	tetraethyl orthosilicate

Acknowledgements

As every story has an ending word and every book has a final page, my PhD approaches its finishing line. I would like to throw back to my life in Sweden in the summertime in 2016. At that time, I was finishing my master study in Uppsala University in Sweden. I read through the PhD employment ads frequently on the Internet at my home in Flogsta. After sending out tens of emails around the world, I got around 5 interviews chances. Finally, two offers were on my desk. One from Leibniz Institute in Aachen, Germany and the other one from Separex, France (with the coordination with TU/e). Well, I did not remember the details. I think I listed all the advantages and disadvantages for these two options for making a rational choice. However, emotionally, I supported Italy in national level as I witnessed their best performance back to 2006 and always love their strong defense. In addition, I have several French friends in Sweden (still in good connection till now) while I could not get along with most German classmates in school at that time. I therefore had the feeling that I have some magic connection with France which should go further in my lifetime. After the confirmation of the French offer, I started to learn French every day, practice orally with my French pals and even listen to and learn to sing 'La Marseillaise'. After going back to China from Sweden, I started to apply for French Visa. Everything seemed settled, with only some formality issues left. I would say it was a quite relaxed and good summer vacation at that time in China. I traveled a lot and had many good memories across China. However, my contact person in Separex were reluctant to reply, which normally took more than one week for the reply email. Well, maybe French people are relaxed, especially in the summer vacation. Therefore, I did not pay so much attention. In July 2016, things turned wired. As the starting date approaching, the visa application was still on the way, far behind my expectation. Ok, I would admit that it is the most attractive part of life that you never know what to come next. I received a phone call from the coordinator in this EU project. She told me: Well, this French company might have some financial problems. That is first time that I really witnessed the bankruptcy of a company. My French dream seemed broken. The coordinator named Beulah (who is also called Elizabeth) told me that they will take care of everything and do not worry too much. After going through some pressure and worries, I ended up in Eindhoven, The Netherlands in some day in November. The final punchline of this story is that I was going to Germany, Nanolytics GmbH in Potsdam. It seemed like that an Italian football fan would end up in Germany. There are so many stories between these two countries, politically and also in the football history so that I do not like Germany so much.

A temporary stay in Eindhoven seemed prolonged due to formality issues. I think I was not a big fan of administrative issues from that time. I stayed in Eindhoven till September 2017. I spent around 10 months in former SMG. I really like to thank Elizabeth for organizing everything and take care of my special issue throughout. Also, I thank prof. Sommerdijk for his help and accepting me in his group for a temporary stay. I enjoyed my time in SMG although the first year of PhD was just trials and errors without any idea doing what. Sitting at home now, I would say I wasted the time in a meaningful way back then. Without any centrifugation specialist in SMG, I mostly learnt and did research myself, with my own

supervising out of my own curiosity. Besides to it, I thank Dr. Patterson for teaching me how to do research properly and discussing with me patiently although my project does not fall into his research interest exactly. From that time, I also communicated with Prof. Cölfen frequently when I met some AUC problems unsolved. I am always saying that he is the best professor I met in my lifetime so far, who shows me a really good example of doing top research and doing top supervision. From our frequent communication, I felt he is a warm, helpful and considerate person. I also would like to thank Mengdi Chen for her help in AUC although she was in China back then. At this time period, I did not have so much progress in research, but I met many nice people in my life, especially my MULTIMAT friends, my SMG pals. Yifei and Hao gave me some nice suggestions in research. I met Yizhou and Fei, who we had so much fun in free time as we drank and chatted on every Friday night. I continued my gym life in the Netherlands too. SSC has the best ever equipment as I have been to around 10 gyms around the world. I met Jnlin in gym, with who we spotted each other. Lastly, in almost every weekend, I played football with a local Chinese team. We played tournament games together, had some barbeque and had a lot of fun. Especial regards to Chengxi, who is the captain in our team and organized everything. That is Chapter one in my PhD path.

In 17 September 2017, I set off for Potsdam Germany where my two-year German Chapter started. I firstly thanked Prof. Sommerdijk for his help so that I could have the great opportunity to work in the group of prof. Peter Fratzl and had the access to a variety of equipment, especially SEM, DLS and PUC there. Without the access to MPIKG, I could not do my research properly in Nanolytics, a small start-up company mainly focusing on AUC. I did not have a good time with Dr. Schilling to be honest as he did not pay much attention on my research and pushed all his responsibility to Helmut instead. However, due to the opportunity of working as a guest scientist in MPIKG, I could still do research well and had some important progress. In addition, I met many excellent research friends in MPIKG, especially a group of Chinese students, who I can talk with, have food with and drink with for many good memories. I met Jianke Sun, Jianrui Zhang, Yang Yu, Qinqin, Zhaoyong Zou and so on. I still keep contact with them and we will meet in China maybe several years later as we work in similar research subjects. My happiest time in Potsdam is surely weekend time where I went to Berlin every Saturday morning by train at 1200h. I found a really good bunch of Chinese to play football with. We normally had dinner together after football. I really would say it is the best memory I had in Berlin. They have different backgrounds and from different ages. We get together just for the fun of football. Here I really thank Jin Zhang for his organization. He is really friendly and a good captain although his shooting is so so, Haha. Football helped me through this tough time. Also, I met several nice guys in Potsdam, especially Ziheng Zhou from my hometown, Zhengge Zhou and Yang Liu. We had fun together. However, Nanolytics is not a good place to do research for me since the poor supervision and facilities. I made to move to AG Cölfen, the southern part of Germany for a better research atmosphere in June 2018 although I really like those people in Berlin and MPIKG, and the atmosphere in Berlin where you can feel the freedom and happiness without money. Berlin is surely a best place to live where cultures here are really diverse.

From June 2018, I moved again, to Konstanz, for my secondment stay in AG Cölfen. I always say the atmosphere in the group and the attitudes of the group members largely

depend on the boss. Thus, I will say AG Cölfen is a really friendly and united group although group members have different characters. This is mainly due to the personality of Helmut. As I also tell every friend, he is the best scientist, both outside and inside the research. He is super friendly, and he shows his care for every group member very well. I would say that he shows me how one can deal with people and do good research. I believe he really has a large effect on my research life. When I may have my own research group later in the future, I will be nice to my students and always think for them. In Konstanz, with the access to all kinds of equipment, I had really smooth progress in research. I did most of vital experiments in Konstanz. Here I would like to mention Zongkun Chen, Yujie Wang, Song Chen, Gulli, Maire, Andi, Eddie and all group members who all help me a lot in my research. Also, the two excellent engineers in the group Dirk and Rose helped me a lot in my AUC experiments. The only bad memory I had in Konstanz that I feel very sorry for is that I broke DLS by accident which lead to a permanent ban on the usage of the DLS machine. I still think it was an overreaction which I however cannot change it. Without this, I would say I have a really happy time in Helmut's group. I did many experiments and finished most parts of my thesis work there.

As planned, in November 2019, I went back to TU/e for my final year. After two year stay in Germany, everything changed here in TU/e. No SMG anymore and all former SMG people moved to the neighbouring SPC group. My supervisor and promotor also changed. I would say I was lucky as I was in Germany when SMG was in a dramatic chaos, which lead to research delay of my several colleagues. The last year was quite peaceful for me since most of my work was done before I was back. I really thank Dr. Evan Spruijt and Dr. Maarten. Biesheuvel for a nice collaborative project. I did the experimental experiments while they both provided the theoretical support, which finally lead to a publication in *Soft Matter*. It was a quite happy collaboration experience where I was also granted the correspondence author for the first time. I would say I really enjoyed working with them and started to enjoy the collaborative atmosphere in academia. I was also very happy that I had the opportunity to work with Maarten Bransen in the group of prof. Alfons van Blaaderen. I even had the chance to go to their group in Utrecht University to do experiments weekly. It is also a good collaboration and I enjoy it. I really appreciate Alfons for giving me the chance. He does really top research in condensed matter and I feel really honored to have collaboration with him. Several months later, a well-known public disaster happened, which is still going on. It is a disaster for everyone in the world, which should have made human beings all over the world realize that vital problems are global, which requires the collaboration of all humans instead of distrust and isolation from others. We cannot predict when it will end but I hope human beings learn something from this tragedy for the next global issue: climate change. Personally, I also learnt to stop a while and rethink what I am doing. In this strange time, I really thank Bert for the conversation and mental advice in weekly meetings. I also thank prof. Qihuo Wei for his career advice. I really do not know by how the pandemic will end but I learned to be generous to myself and enjoy the lab time if I can. Currently, it seems to be settled that I will go to Switzerland for my post doc at the end of 2020. I think it will be a new start that I can do more nice research. At this point of age, I also tend to stabilize a bit, maybe after this post-doc time. Doing research is the way to get along with the truth while

having a close relationship with another people is the way to get along with humans. These two experiences are equally important in one's life.

Finally, I would like to thank my parents and grandparents for supporting me going abroad although I am their only child and they miss me so much sometimes. Life is like a trade-off. You get something while you will lose something. Getting older, we will lose bit by bit, and finally lose everything. I think at some point we need to get used to losing and still cherish everything we have now.

Curriculum vitae



Xufeng Xu was born on 01-08-1992 in Dafeng District, Yancheng City, Jinagsu Province, China. After completing his high school study in 2010 at Dafeng High School, he started his BSc study in Applied Chemistry in Soochow University, China. He studied in the Intensive Training Class, where all the lessons were taught in English by professors who have overseas research experiences. He also obtained the opportunity to go to NUS and NTU in Singapore for exchange studies for about one month.

During this time period, many international communications with foreigner students and professors were organized. He graduated in 2014 under the supervision of Prof. Hua Li and Prof. Jianmei Lu with the BSc thesis named “The effect of different solvents on electrical properties of PVK-based electric memory devices”.

Straight from September 2014, he accepted Global Merit Scholarship from Uppsala University in Sweden to conduct his MSc study in Chemistry while he declined the well-known Orange Tulip Scholarship from Nuffic Neso China for the study in the Netherlands. In 2016, he obtained his MSc degree under the supervision of Assoc. Prof. Dimitr Ossipov in the department of Chemistry-Ångström Laboratory with the thesis titled “Development of defined synthesis of hyaluronic acid modified with bisphosphonate and photoreactive groups for 3D printable hydrogel formation”. In November 2016, he moved to the Netherlands under European Union's Horizon 2020 research and innovation programme under grant agreement No. 676045 with the project “Ultracentrifugation techniques for the fractionation and controlled assembly of nanoparticle” under the supervision by Prof. de With (TU/e) and Prof. Cölfen (UoK) (also by Prof. Sommerdijk (RU) in the first year). In this time period, he stayed in several places, including Nanolytics GmbH (with an association stay in MPI-KG) in Germany, University of Konstanz in Germany, and TU/e in the Netherlands.

Publication list

- I. X. Xu, T. Franke, K. Schilling, N.A.J.M. Sommerdijk, and H. Cölfen*. **Binary Colloidal Nanoparticle Concentration Gradients in a Centrifugal Field at High Concentration.** *Nano Letters* 2019 19 (2), 1136-1142.
- II. Xufeng Xu, Helmut Cölfen*. **Binary Colloidal Nanoparticles with a Large Size Ratio in Analytical Ultracentrifugation.** *ChemPhysChem* 2019, 20 (14), 1799-1803.
- III. Xufeng Xu, Gijsbertus de With* and Helmut Cölfen*. **Self-association and gelation of like-charged colloids at very high concentration.** *Science Advances* 2020, in revision.
- IV. Xufeng Xu*, P.M. Biesheuvel, Helmut Cölfen and Evan Spruijt*. **Layering of bidisperse charged nanoparticles in sedimentation.** *Soft Matter* 2020, 16, 4718-4722 (first and corresponding author).
- V. Xufeng Xu, Baohu Wu, Helmut Cölfen* and Gijsbertus del With*. **Superstructure control for monodisperse nanoparticles with a low Peclet number in ultracentrifugation.** *Journal of Colloid and Interface Science* 2020, in revision.
- VI. Xufeng Xu, Helmut Cölfen*. **Ordering of nanoparticles in a centrifugal field.** *Nanomaterials* 2020, to be submitted (invited review).
- VII. **Book chapter: Analytical ultracentrifugation** with prof. Cölfen in the Handbook: **Particle Separation: Techniques Fundamentals, Instrumentation, and Selected Applications** by *Elsevier Science* (in preparation).
- VIII. **Laves phase formation from binary hard spheres by CLSM/STED** (in collaboration with prof. van Blaaderen, Utrecht University), in preparation.
- IX. **A universal approach for nanoparticle fractionation**, *Nature Nanotechnology*, in preparation.
- X. **BCC/FCC phase tuning for the assembly of monodisperse nanoparticles in a centrifugal field**, (in collaboration with E. Deniz Eren, TU/e), in preparation.

